Few Hole Quantum Dots in a Gated GaAs/AlGaAs Heterostructure

by

Alexander Bogan

A thesis
presented to the University of Waterloo
in fulfillment of the
thesis requirement for the degree of
Doctor of Philosophy
in
Physics

Waterloo, Ontario, Canada, 2019

© Alexander Bogan 2019

Examining Committee Membership

The following served on the Examining Committee for this thesis. The decision of the Examining Committee is by majority vote.

External Examiner: William A. Coish
Associate Professor,
Dept. of Physics, McGill University

Supervisors: Jan Kycia
Professor,
Dept. of Physics and Astronomy, University of Waterloo

Sergei Studenikin,
Adjunct Professor,
Dept. of Physics and Astronomy, University of Waterloo

Internal Member: Robert Hill
Associate Professor,
Dept. of Physics, University of Waterloo

Internal-External Members: Jonathan Baugh
Professor,
Dept. of Chemistry, University of Waterloo

Zbigniew Wasilewski
Professor,
Dept. of Electrical and Computer Engineering,
University of Waterloo

This thesis consists of material all of which I authored or co-authored: see Statement of Contributions included in the thesis. This is a true copy of the thesis, including any required final revisions, as accepted by my examiners. I understand that my thesis may be made electronically available to the public.

Statement of Contributions

The contents of this thesis are the author's own work, but the studies presented herein were the result of a collaboration with others and this work at times describes their work in the author's own words. Particular attention has been paid to the author's own contributions to these studies, but for clarity credit will be given here to the efforts of these collaborators.

In particular, Marek Korkusinski contributed the numerical simulations of the experiments presented here. Where numerical simulations are described in this thesis, these simulations were his work. As a result, the simulations themselves are not discussed in detail (except in appendix A) and the author refers the reader to the cited publications when they are relevant.

The experiments themselves were designed and conducted by the author, with guidance from Sergei Studenikin.

The author did not substantially contribute to the installation and wiring of the cryostats described in chapter 3 or to the construction of the sample holder used, beyond effecting minor repairs and both operating and doing regular maintenance of the cryogenic systems. The author credits Piotr Zawadzki and Sergei Studenikin with the initial installation and setup of the dilution refrigerator and he3 cryostat respectively.

Abstract

This thesis presents a set of experiments that explore gate defined hole quantum dots in the GaAs/AlGaAs heterostructure. These experiments explore the evolution of the quantum states of holes in a double quantum dot. The focus is placed on the charge distribution and spin degrees of freedom, with a view toward developing quantum information technologies.

Chapter 1 briefly introduces the concept of quantum information and gives a perspective on the role of quantum dots and spin qubits in implementations of quantum information technology. The particular potential of hole spins will be summarized.

Chapter 2 outlines the design and fabrication of the device, as well as simple characterization measurements.

Chapter 3 describes the experimental setup used to perform measurements and describes the methods and circuits used to perform different types of electrical measurements of the device.

Chapter 4 reviews basic theory of transport through quantum dots and develops the notation and conventions used in the rest of the thesis to describe both transport and charge detection measurements. The technique of resonant transport spectroscopy is applied to a double quantum dot to show that, in contrast with electronic quantum dots in the same material system, the full spectrum of states are visible in transport spectroscopy due to strong spin orbit interactions for holes. The effective gyromagnetic ratio of a single hole is measured via transport magnetospectroscopy. The dramatic anisotropy of the g-factor in a plane perpendicular the heterostructure growth axis is studied by tilting the magnetic field. The degree of anisotropy in this double quantum dot suggest the confined holes are heavy holes, and some preliminary estimates of spin coherence are made.

Chapter 5 presents a novel method for the projection and measurement of a single hole spin in a double quantum dot, which allows for fast spin to charge projection of a hole spin in 100 ns or less using a charge detector. This is accomplished by encoding the projected spin information into a long-lived metastable charge state. An experimental study using this method to measure the spin relaxation of a single hole over a range of magnetic fields is presented, and the dominant microscopic mechanism of single spin relaxation is deduced.

In chapter 6, the coherence of the charge and spin degrees of freedom is studied more carefully through the technique of Landau Zener Stueckelberg Majorana interferometry. The technique is briefly reviewed and an experiment is presented in which LZSM interferometry was explored in the transport spectra of a single hole, revealing the mean coherence times of the charge and hybrid spin/charge qubits.

Acknowledgements

I have been fortunate to have the opportunity to work with a diverse group of resourceful, determined, talented, and good-hearted people who are deserving of thanks and shared credit for much of what is to be described later in this document and much more that will not. I have the privilege of sincerely thanking my co-workers, collaborators, and supervisors.

Jan Kycia is certainly to blame for my pursuit of a career in experimental physics. His passion for experiment and his brand of instruction was inspiring during my undergraduate degree, and Jan has continued to be a font of esoteric history and useful technical knowledge. His practical resourcefulness conveyed to me the useful lesson that one can always benefit from a bit more knowledge about one's tools.

Sergei Studenikin introduced me to experimental physics as a profession and for that I will be eternally grateful. His instruction, trust, and understanding made it possible to flourish in this environment.

Guy Austing, Louis Gaudreau and Jason Phoenix should be thanked for their positive contributions to the social and professional atmosphere of the lab, and for stimulating discussions of other research. I would like to thank Jason and Louis in particular for sharing software developed for their projects.

I would also like to thank Piotr Zawadzki for his unequaled dedication.

Further thanks to Marek Korkusinki for his theoretical work and for enduring my exhaustive questions.

Special thanks to Andrew Sachrajda in equal part for dedicating time to the administrative aspect of scientific enterprise and for setting a great example as an unpretentious leader.

I would like to thank Lisa Tracy, John Reno, and Terry Hargett of Sandia National Labs, who contributed the sample studied in this work.

Finally, I would like to acknowledge the financial support of NSERC and NRC, which contributed to the maintenance of my well being during this work.

Dedication

This thesis is dedicated to Kira Sfiligoi and to Sandra and Michael Bogan.

Table of Contents

List of Tables

List of Figures

Please excuse the crudity of this model. I didn't have time to build it to scale... or to paint it.

Doc Brown

Chapter 1

Introduction

1.1 Quantum Information

The large scale manual collection and processing of information, as well as computation and modeling of systems, vastly predates the automated processing of information with the aid of mechanical or electronic devices. Examples of manual mechanical aids for numerical calculation date back as far as the ancient Sumerian abacus or the Antikytheria mechanism, and the practice of manually, yet accurately collecting and disseminating information through large-scale organizations dates back at least as far as the concepts of taxation and military strategy.

Automated mechanical computation has been an academic interest for at least two centuries. However, the maturation of computation and information as an academic, industrial, and cultural phenomenon arguably began between the mid 1930s and 1940s. In 1937 Alan Turing presented his Turing machine, a foundational model of computational theory [1]. Meanwhile, the founding of information theory as an academic discipline is commonly attributed to Claude Shannon [2], who published his seminal work in 1948: a year after the point contact transistor was demonstrated in 1947. The field of computer science has grown and flourished well into the present day, as technology has allowed automated computation and collection and processing of information has become more economical.

Large quantities of human labour have historically been organized and applied to computation and information processing problems such as tax collection, scheduling, and logistics; and yet the impetus to discuss information and computation mathematically apparently did not emerge until it became possible to surpass the computational and information processing limits of organized human bureaucracies, individuals, and teams.

The revolution brought on by automated information processing devices has transformed the language we use to describe information. Concepts like "data" feature prominently in our daily vocabulary, and we instinctively think of information in quantifiable terms. It has become comparatively trivial to distribute and copy large works and databases. The changes to our culture and lifestyle in the developed and developing worlds are so great that the development of automated information processing arguably defines our current age. The theory and practice of classical information processing and communication has been revolutionary.

The origin of the *quantum* information field is often attributed to Richard P. Feynmann, who spoke in 1981 [3] about the attractive possibility of simulating quantum phenomena with a quantum computer. Be that as it may, works in quantum information do pre-date his talk, including Holevo's theorem [4] bounding the transmission of classical information by quantum channels in 1973 and an attempt to generalize Shannon's information theory to a quantum theory of information [5].

As was the case with classical computation and information theory, quantum information has developed dramatically in recent decades. As computational technology has begun to butt the physical limits of classical systems for classical computation, the impetus to explore beyond those limits to understand the challenges and opportunities of systems with quantum phenomena has grown.

Theoretically, some potential applications of quantum computing have emerged. These include assisting our understanding of many body quantum phenomena through quantum simulation [6, 7], solving difficult logistics problems in the classical world using quantum searching [8], challenging existing cryptographic security previously thought sufficient in a classical world [9], and simultaneously assisting in the exchange of private communications [10, 11] to name just a few.

In response to the growing possibilities, many physical implementations of quantum information have been developed, including photonic qubits [12], superconducting qubits [13], and spin qubits [14].

1.2 Quantum Dot Spin Qubits in Gated Semiconductor Heterostructures

Some physical implementations have clear advantages and disadvantages for certain applications. For example, photonic qubits are seemingly ideal for long-range communication of information, but photons may be a comparatively poor choice for in place, long term information storage and retrieval because they always travel at the speed of light, necessitating some sort of light-matter interaction. Spin qubits in semiconductors can be long lived [15], but spin qubits do not directly interact over long distances (meters to kilometers). These competing properties can be complementary, and there is great interest in inter-conversion of quantum information between qubit implementations [16].

Toward the realization of quantum information networks, spin qubits have been pursued in optically active defect centers [17–21] and quantum dots in optically accessible semiconductors [22–29]. In particular, spin qubits in gated quantum dots [30] are attractive because of the large degree of in-situ electrical tunability of quantum dot properties offered by these platforms, as well as the capacity for electrical control of spin qubits and electrically mediated interactions between them. Moreover, gated quantum dot technology supports the precise placement of multiple dots to create double [31], triple [32, 33], quadruple [34], and even larger [35] arrays with relative ease. Whereas in nitrogen vacancy centers and other defects the charge of the quantum dot is fixed by the defect type, in quantum dots in gated heterostructures the charge occupation and total charge of even large arrays of quantum dots can be varied by tunneling to and from a lead [34].

1.3 Hole Spin in Quantum Dots

To date, efforts to explore spin qubits in gate defined quantum dots in III-V semiconductors have mostly focused on the electron spin, but owing to advances in device fabrication [36] and predictions of increased coherence [37, 38], hole spins have received some attention in recent years. Investigations of hole quantum dots have been made in InAs [39], InSb [40], and SiGe [41] nanowires, Silicon CMOS devices [42, 43]; Silicon [42], GaAs [44], and SiGe [45] heterostructures; and self-assembled InGaAs quantum dots [46].

Some of the interest has been driven by a desire for longer qubit coherence times, which are frequently limited by hyperfine interactions between the spin qubit and the angular momentum bath of the host material's nuclear spins. In [40] the hole spins were estimated to experience hyperfine couplings an order of magnitude weaker than electrons in the same system. In [41], the qubit decoherence times for holes were estimated to be 20 times longer than for electrons, and this difference was attributed to a weaker hyperfine interaction. Reducing the hyperfine interaction strength is a key motivation for the study of spin qubits in (isotopically purified) Silicon rather than group III-V semiconductors. However, Silicon is not a direct band-gap semiconductor and the development of optical photon to spin or spin to photon interfaces is challenging in this material.

Other studies focused on observations of the anisotropic hole spin g-factor [47, 48], which was demonstrated to vary in magnitude by up to 50% depending on the orientation of the magnetic field. A tunable g-factor, ideally approaching zero, is relevant for photon to spin conversion [16, 49] as it would enable the quantum media conversion between photon polarization and hole spin [16] or help increase the fidelity of photon time bin and hole spin conversion [50].

In addition to the anisotropic g-factor and potentially extended coherence times, effects of strong spin-orbit interactions have been observed in hole transport experiments through quantum dots [39] including specifically in GaAs [44]. As the spin orbit interaction couples the electric dipole to the spin of the carrier, these interactions offer an avenue to fast and efficient qubit control and may enable other novel techniques. GaAs is an attractive material because the technology to create gate-defined quantum dots is well developed and GaAs permits coherent electron hole pair photo-generation because of its direct band gap, which is important for quantum media conversion between photons and spins.

This work presents several experimental studies of some of these properties of hole spin qubits in gate defined lateral quantum dots in GaAs, focusing on the coherence of single hole spins and inter-dot charge tunneling, as well as some of the implications and consequences of the strong spin orbit interaction for holes.

Chapter 2

Sample Fabrication and Characterization

2.1 Design and Fabrication

The experiments described in the following chapters were performed on a double quantum dot device fabricated by Sandia National Labs [36, 51]. This chapter will briefly introduce quantum dots and describe the fabrication of this specific device, as well as highlight several noteworthy differences between this device and typical double quantum dot devices used to confine electron spins in GaAs heterostructures.

In the language of artificial semiconductor quantum dots, the term "gate-defined" as applied to quantum dots implies that electrostatic gates provide confinement in at least one dimension. This provides an element of in-situ electrical tunability that is attractive for experiment and for applications. Moreover, the gates can be modulated electrically at microwave frequencies to manipulate the quantum dot and confined spins, including hole spins [52].

A common variety of gate-defined quantum dot is the "lateral" semiconductor quantum dot, where confinement is provided in two dimensions by electrostatic gates. For example, in a III-V semiconductor material system such as GaAs, a heterostructure is fabricated with either a two-dimensional conductive heterointerface or quantum well. If the quantum well is populated with carriers, the resultant conductive layer is called a Two-Dimensional Electron Gas (2DEG) or Two-Dimensional Hole Gas (2DHG) depending on the carrier type. Two-dimensional systems can exhibit the Quantum Hall Effect [53, 54], Microwave-Inducted

Resistivity Oscillations [55, 56], and associated Zero-Resistance States [57, 58] to name just a few. These effects are well studied and can be used to measure certain characteristics of 2D systems, including the concentration and mobility of carriers (as in section 2.2).

While modulation doping [59] is frequently used to introduce a built-in electric field that attracts carriers to populate the two dimensional gas, for the device under study a global accumulation gate was employed to provide a tunable hole concentration in the 2DHG. In addition to the global gate operating in accumulation mode, local depletion mode gates were deposited to locally shape and tune the confining potential of the quantum dots. Finally, electrical contact was made to the 2D system using an ohmic metal-semiconductor interface so that currents could be supplied from the ohmic contacts to initialize the device in a conductive state.

Figure 2.1 shows the vertical layout of the heterostructure used to host the quantum dot used in these particular experiments. With the sample kept at a temperature of 630 C, GaAs and $Al_{0.5}Ga_{0.5}As$ were deposited on the surface via Molecular Beam Epitaxy. In chronological order, the following layers were deposited on a GaAs substrate:

1. A 300nm “buffer” layer of GaAs.
2. A superlatice layer: 300 repetitions each of 3nm of GaAs and 10nm of $Al_{0.5}Ga_{0.5}As$, alternating
3. 1000nm of GaAs
4. 100nm of $Al_{0.5}Ga_{0.5}As$
5. A 10nm GaAs “cap” layer.

The purpose of the “buffer” layer is to suppress structural defects at the substrate/buffer interface that propagate layer by layer through epitaxial growth. If the buffer layer is too thin compared to the mean propagation length of these defects, these defects will be present in the surface.

Ohmic electrical contacts were made to the 2DHG by evaporation of AuBe alloy and annealing. Ti/Au local gates and an Aluminium global gate were isolated from one another and from the ohmic contacts by 130nm of Al_2O_3 deposited by Atomic Layer Deposition (ALD). Figure 2.2 shows an SEM image of the horizontal layout of local gates in a similar sample, indicating the intended positions of the two quantum dots (circles) and a Quantum Point Contact (QPC). The current through the QPC was used as a charge sensor [60].

The next section will focus on the characterization of the sample, including the tunability of the carrier concentration.

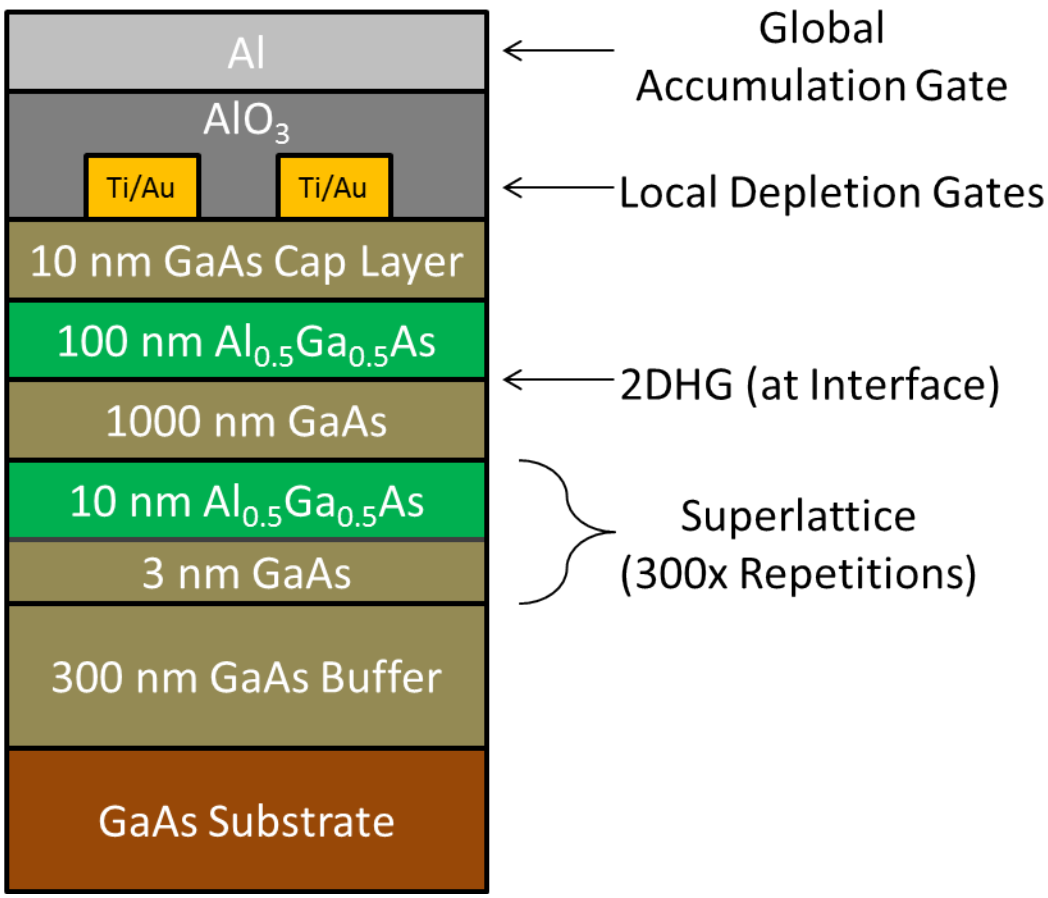

Figure 2.1: A schematic vertical cross section of the device showing layers of material including 2DHG, local Ti/Au depletion gates and Al global gate separated by Al_2O_3 *insulator, as well as the 2DHG at the AlGaAs/GaAs heterointerface between depletion-mode local gates.*

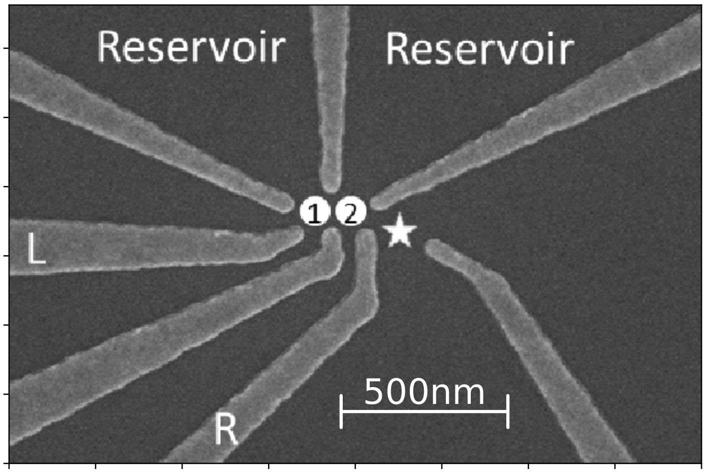

Figure 2.2: Scanning electron microscope image of a similar device with Al global gate and Al oxide omitted. The horizontal local gates (light grey), the ohmic charge reservoirs, the quantum dots (labeled 1 and 2), and the QPC charge sensor (identified by a star) are visible.

2.2 Sample Characterization

As described in the previous section, the 2DHG in this device was populated with carriers using a global accumulation gate to provide electrically tunable carrier concentration. A model AVS-47 cryogenic resistance bridge was used to measure the two-point resisistance (R_2) of the sample, including ohmic contacts and 2DHG, with the sample held at a temperature of 60 mK. Shubnikov de Haas magnetoresistance oscillations were observed by measuring R_2 as a function of an applied magnetic field normal to the plane of the 2DHG (B_Z) between 2.0 T and 4.0 T. Shubnikov de-Haas Resistivity Oscillations (SdHO) were used as an experimental probe of the bulk majority carrier concentration as a function of the accumulation gate voltage. The period of the SdHO resistivity oscillations is inversely proportional to the carrier concentration:

$$\Delta\left(\frac{1}{B}\right) = \frac{2e}{hn} \tag{2.1}$$

where n is the carrier density.

The period of each SdHO trace was measured as a function of the uniform magnetic field applied normal to the plane of the sample, and from this data the carrier density was obtained.

Typical resistivity oscillations are plotted in panel A of figure 2.3 for several values of V_{GG}, the voltage on the global accumulation gate, while a set of extracted carrier concentrations are plotted in panel B for V_{GG} between $-8.0\,\mathrm{V}$ and $-6.8\,\mathrm{V}$. Over this range, the carrier concentration varied between $3.36 \times 10^{11}\,\mathrm{cm}^{-1}$ and $1.10 \times 10^{11}\,\mathrm{cm}^{-1}$ at a rate of $\frac{\mathrm{d}\eta}{\mathrm{d}V} = -1.87 \times 10^{11}\,\mathrm{cm}^{-2}\,\mathrm{V}^{-1}$.

The 2DHG and the global accumulation gate were modelled as a parallel plate capacitor with a total separation (as designed) of 240 nm (including the cap layer, Al_2O_3, and 100 nm of GaAs).

From the capacitive charging of the 2DHG, the effective dielectric constant k of the sample can be estimated according to:

$$\frac{\mathrm{d}\eta}{\mathrm{d}V} = -\frac{k\epsilon_0}{d} \tag{2.2}$$

where d = 240 nm. This formula gives k = 8.13, which is comparable to the dielectric constants of GaAs and Al_2O_3 at cryogenic temperatures. This suggests that no large parasitic charge has accumulated near the interface to screen the global accumulation gate.

From a linear fit to figure 2.3 an offset voltage of -6.18 V can be identified which is required to produce the necessary band bending to populate the interface QW. In the following experiments V_{GG}=-7.9 V was used, which corresponds to initial 2DHG concentration of $3.2 \times 10^{11}\,/\mathrm{cm}^2$ or 1 hole per $312\,\mathrm{nm}^2$ before depletion gate voltages were applied. The bulk concentration of holes is roughly indicative of how many holes can be confined in a quantum dot of a certain size.

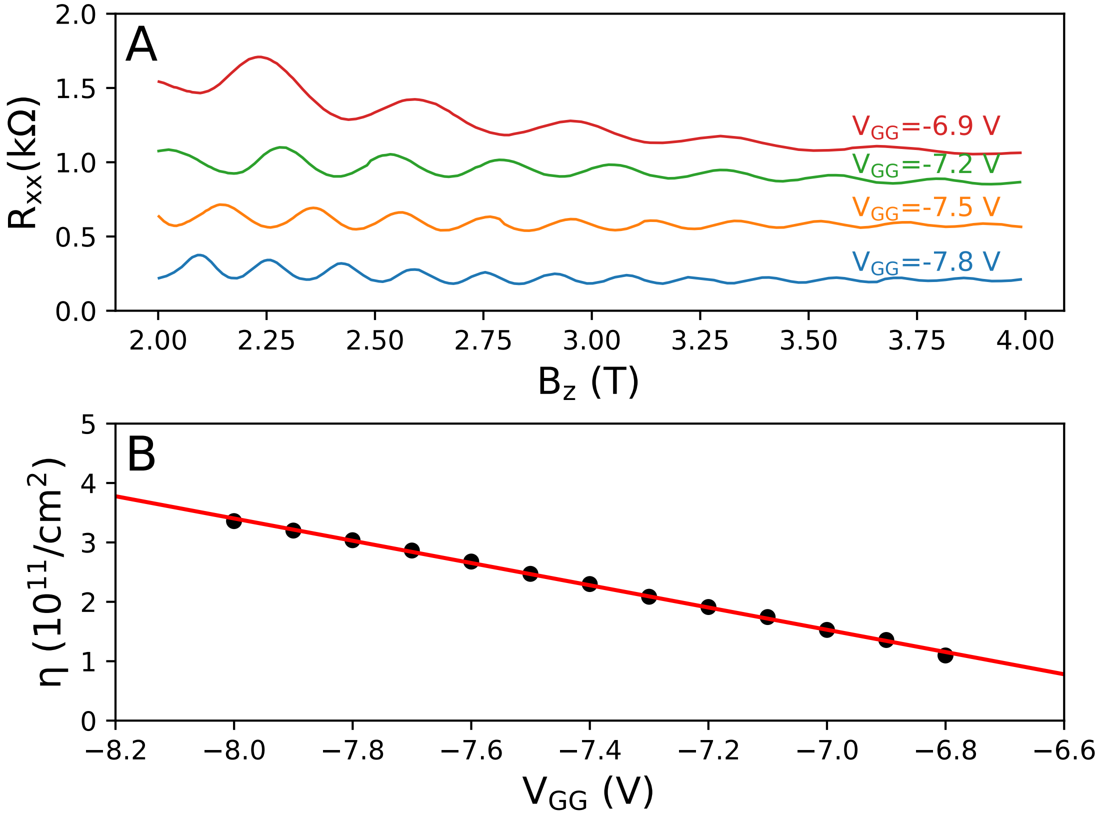

Figure 2.3: ***A****) 2-point measurement of resistance as a function of the magnetic field applied normal to the sample (B_Z) for various voltages applied to the global accumulation gate (V_{GG}).* ***B****) Carrier concentration extracted from the Shubnikov de-Haas Oscillations, varying linearly in V_{GG} at $1.87 \cdot 10^{11}/cm^2/V$*

Chapter 3

Experiment Setup and Methods

3.1 Equipment

DC voltages were generated using three Iotech DAC488HR/4 modules to generate twelve total DC voltages. DC gate voltages were applied through $1\,\mathrm{M\Omega}$ series resistors to limit current supplied to the gates in case of a short. Bias voltage for the quantum dot and Quantum Point Contact (QPC) charge sensor were supplied similarly, with the assistance of custom built voltage divider circuits (see figures 3.11 and 3.12) to provide better resolution. Current through the dot and QPC was measured to a virtual ground supplied by an Ithaco 1211 current preamplifier with configurable gain and bandwidth. The output voltage was digitized using a Hewlett Packard 3458A digital multi-meter. A Tektronix AWG710B arbitrary waveform generator was used to supply the voltage pulse sequence described in chapter 5, while a Tektronix TDS6154C digital storage oscilloscope was used to visualize the pulse delivered to the sample. The oscilloscope's line-trigger signal was used to trigger both the AWG710B and the HP 3458A during the charge sensing experiments of chapter 5, providing additional rejection of 60 Hz noise. Finally, an Anritsu 69377B synthesized high performance signal generator was used to generate the microwave signal for the experiments described in chapter 6.

3.2 He3 Refrigerator

In section 4.5, experiments were performed in an Oxford Instruments cryostat equipped with a split-coil 5 Tesla magnet. A Heliox AST VL sorption pumped cryogenic He3 insert was used to cool the sample to a base temperature of approximately 300 mK inside the bore of the split-coil magnet.

This setup was used because the entire Heliox insert can be rotated freely in the bore of the magnet, even at base temperature, effectively changing the orientation of the magnet relative to the sample about one axis.

The cryostat features a liquid He4 dewar with liquid nitrogen shielding, and is pictured in figure 3.1 fully assembled, with the He3 insert and magnet assembly in the cryostat.

The insert can be rotated in the cryostat. The insert is equipped with a mechanical indicator pointing to a protractor on the magnet assembly, allowing for the rotation angle to be read out visually. The rotation angle was calibrated using the Hall effect in the 2DHG to compare the Hall field (field normal to the 2DHG) with the applied field. The protractor markings are spaced out about every 5 degrees.

The magnet assembly is pictured in figure 3.2, here removed from the cryostat. The coils are directed horizontally, while the insert can be rotated about the vertical axis.

The insert itself, pictured in figure 3.3 without its vacuum shield, contains the refrigeration and electrical components including the microwave transmission lines and sample header. Note that the sample is mounted with the normal axis of the 2DHG horizontal, enabling rotation between a condition where the field is oriented in-plane with the 2DHG and a condition where the field is directed normal to the 2DHG.

Note that the sample was mounted such that the in-plane component of the magnetic field was approximately directed along the major axis of the double quantum dot (the direction of current flow). Figure 3.4 shows the coordinate system that will be referred to in the experiments performed on the He3 system. The x axis is chosen such that the in-plane component of the field is directed along x. The z axis is directed out of the plane of the 2DHG in the growth direction. The y axis is perpendicular to both, and in principle the applied magnetic field in this direction is null. The angle θ corresponds to the displacement of the field orientation from the growth direction (z axis), such that $\theta = 0^\circ$ corresponds to a perpendicular field along z and $\theta = 90^\circ$ corresponds to an in-plane field along x. Unfortunately, the orientations of the crystallographic axes are not known.

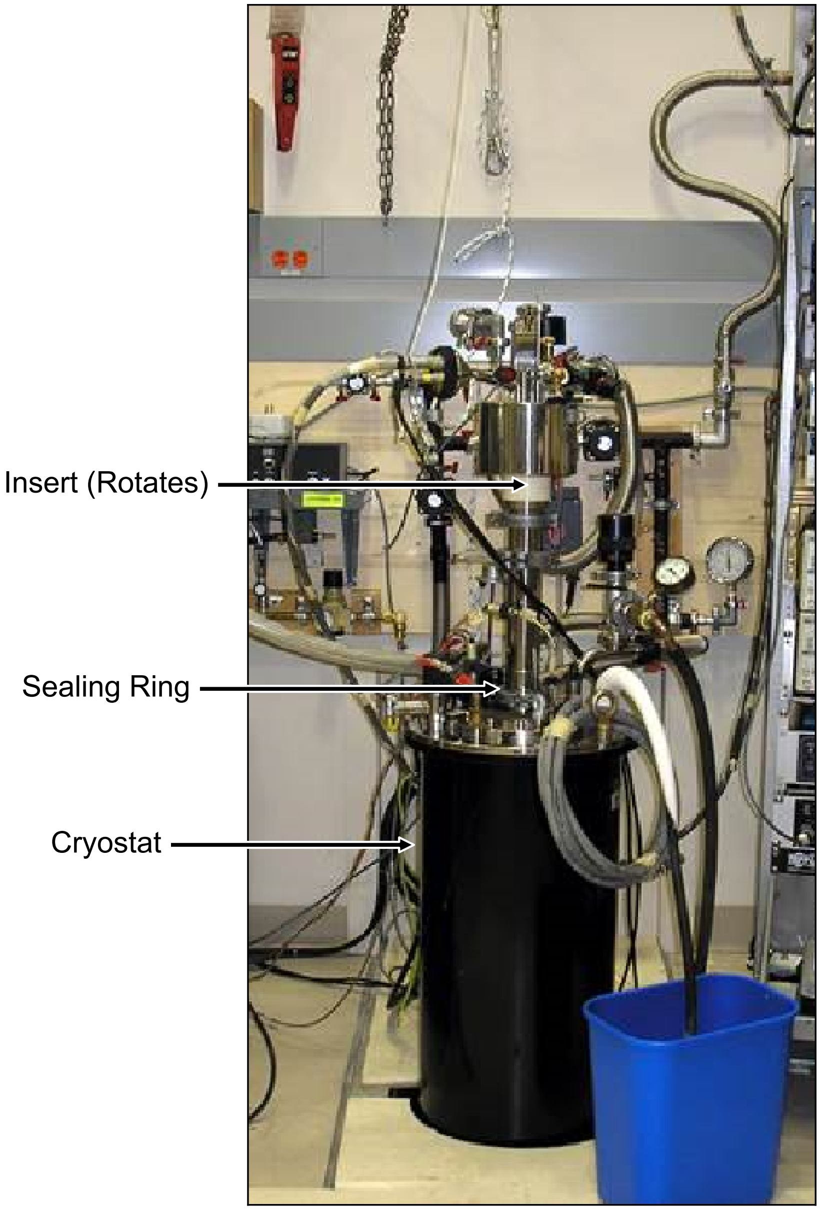

Figure 3.1: He3 cryostat with insert and magnet assembly installed. If cryostat is cold, insert can rotate in-situ. Bath seal is maintained by the sealing ring and clamp (indicated).

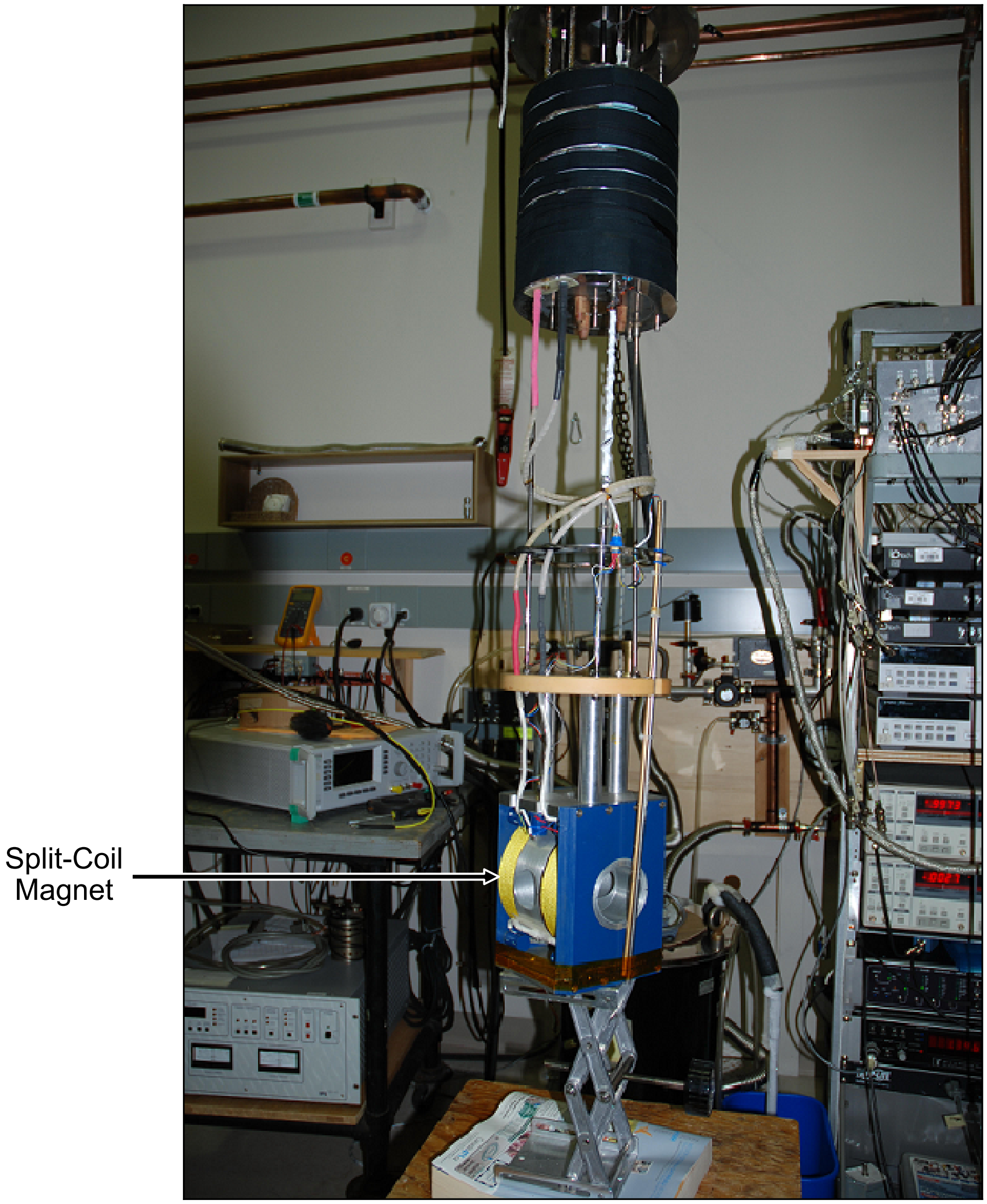

Figure 3.2: He3 cryostat magnet assembly removed from cryostat. Split-coil magnet bore is horizontal (visible) while the insert rotates about the vertical axis when installed. Sample rests in the bore of the magnet when installed.

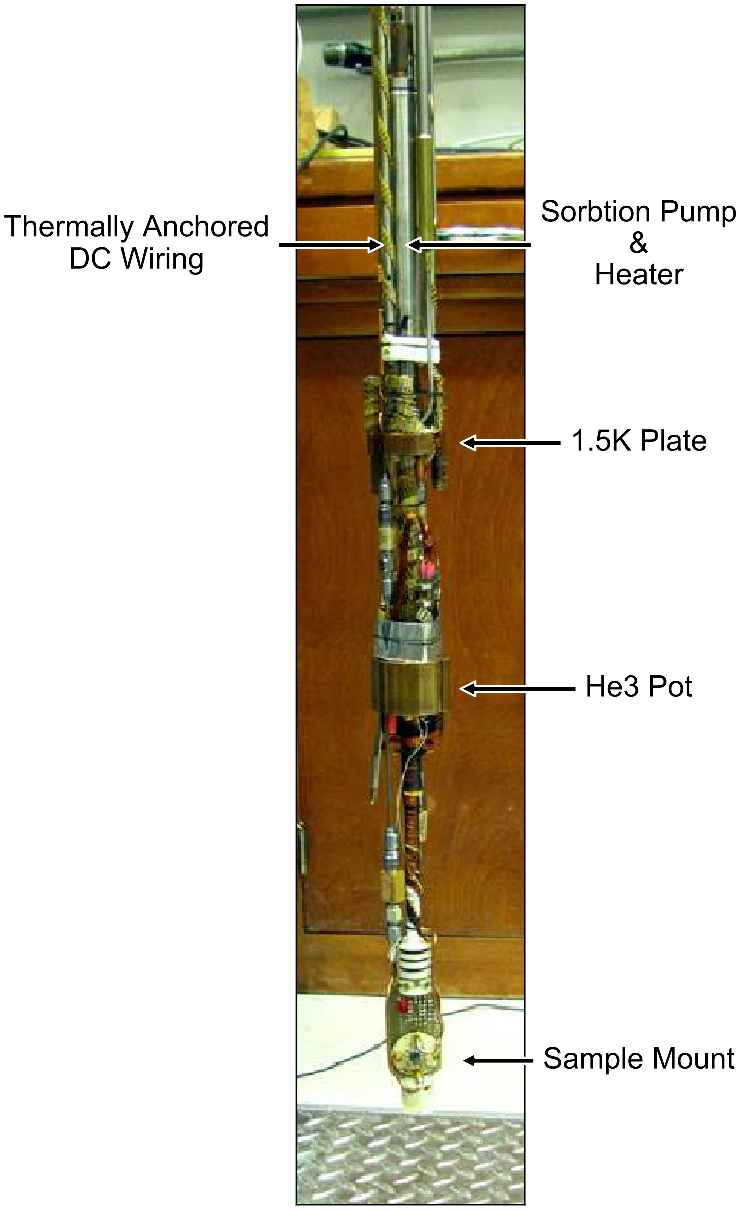

Figure 3.3: He3 sorption pumped insert, shown here with vacuum shield not installed. The entire insert (and sample) rotates when installed in the cryostat.

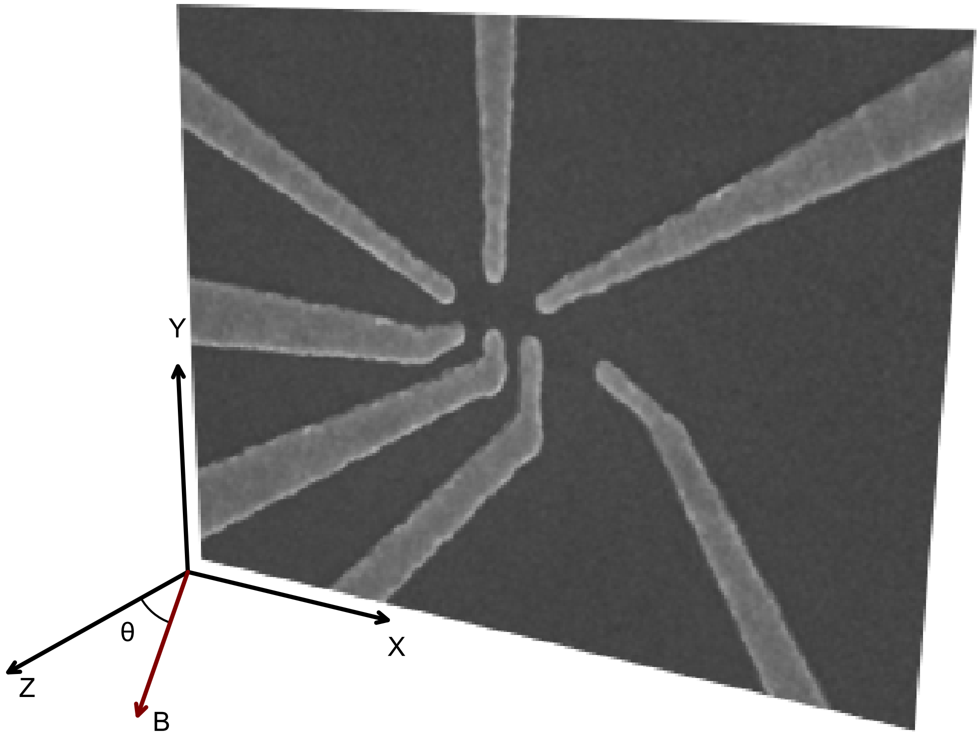

Figure 3.4: Coordinate system used to describe experiments on the He3 system. The Z axis is directed along the growth direction, while the X and Y axes are in the plane of the 2DHG. The angle θ denotes the rotation angle of the applied field from the Z direction into the plane (X direction). The y axis points "up" in the sense of the Earth's gravitational field.

3.3 Dilution Refrigerator

Many experiments described in this thesis were performed in an Oxford Instruments Kelvinox dilution refrigeration unit. The dilution refrigerator cryostat is equipped with a superconducting magnet capable of achieving a 16 T field at 4 K. The sample header included 19 independent voltage pins, each connected to 19 copper lines that delivered DC voltage from room temperature. Two additional semirigid microwave coaxial cables were used to deliver microwave and arbitrary waveform pulses to the lower temperature stages where the signals were added to two of the DC lines. This setup provided a fixed magnetic field normal to the plane of the sample and the capacity to drive two gates on the sample (‘L’ and ‘R’) with microwave signals and/or so-called ‘arbitrary waveform’ voltage pulses.

A schematic showing the wiring of the dilution refrigerator unit is shown in figure 3.5. The exact schematic of the DC biasing circuits used depend on the experiment, and specifically whether the sample is being operated in transport or charge detection mode. Both biasing circuits will be discussed in this section.

The gate electrodes and ohmic contacts on the sample were bonded with Au wires to Au-plated pins on the sample header. The sample header is pictured in figure 3.10, which shows the sample, sample header, Au bonding wires, and the DC and RF lines delivering electrical signals to the header.

Each of the DC lines were part of a lab-made copper wire loom. The loom delivered voltage from room temperature to the sample, but each line was interrupted by one 60 cm of Nickel Chromium thermocoax type coaxial cable for each line between the 1.5 K stage and the Mixing Chamber. The thermocoax cables functioned as high-frequency low-temperature filters [61]. At room temperature, additional filtering on the DC lines was provided by pi filters: 5 µF Oxley pi-capacitor in series with 470 Ω resistor.

The two plunger gate electrodes, ‘L’ and ‘R’ as labeled in figure 2.2, were driven by both DC and RF electric fields. DC biasing of the RF transmission lines was accomplished with customized Anritsu V251 bias tees featuring (nominally) 100 nF replacement capacitors (measured at cryogenic temperatures). The DC input to each bias Tee was driven by a normal DC line. The DC+RF output of each bias tee was semi-rigid Cu coaxiable cable.

The DC lines were thermally anchored to the 4 K plate as well as at the 1.5 K plate and the mixing chamber, at the interfaces between the copper loom and thermo-coaxial cables. The RF coaxial lines were thermally anchored at 1.5 K and the mixing chamber, where the low temperature attenuators and bias tees were located.

The RF lines were thermally anchored to the 4 K plate, the 1.5 K plate, and the mixing chamber using copper wires, plates, and brass screws to provide clamping pressure.

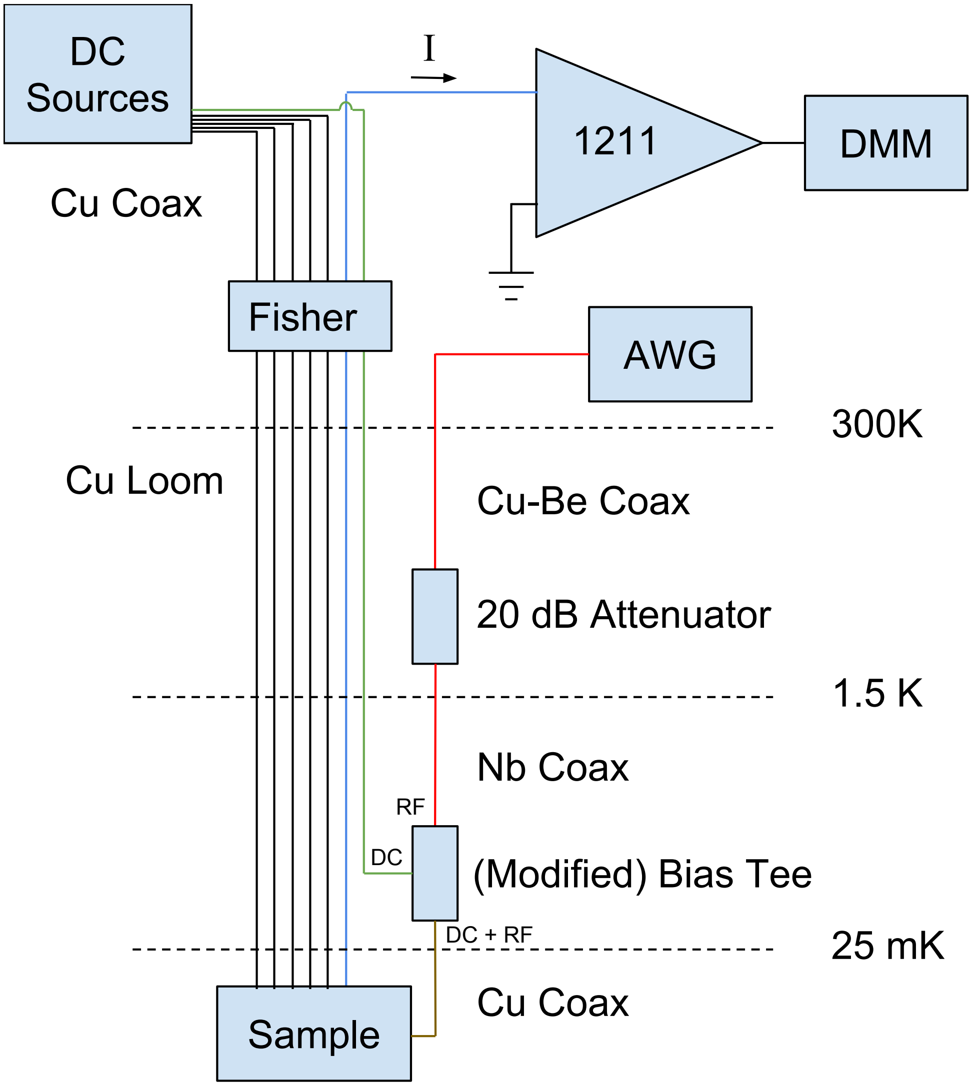

Figure 3.5: Dilution refrigerator setup wiring diagram. Most gate electrodes and ohmic contacts are DC biased through copper wire. Two gates (just one pictured) are driven by a DC and RF signal combined in a bias tee thermally anchored to the mixing chamber. Cu-Be coaxial transmission line is used to deliver the high frequency component of the signal from the Arbitrary Waveform Generator (AWG) or microwave generator to the 1.5 K *stage, where it is attenuated. A superconducting Niobium line is used to thermally isolate the mixing chamber. Below the bias tee, copper coaxial cable is used to deliver the DC+RF signal to the sample mount.*

From room temperature to the 1.5 K stage, the transmission lines were composed of Copper/Beryllium alloy. A 20 dB in-line attenuator serves also as a thermal anchor to the 1.5 K stage. Below the attenuator, superconducting Niobium coaxes were used as low-temperature heat-switches to prevent thermal conduction from the 1.5 K stage to the mixing chamber once it is cooled below the superconducting transition of Niobium at 9.3 K. The Niobium coaxial cables fed into the RF input of the bias tees and the AC+RF signals from the tees were delivered to the sample by copper coaxial transmission lines to the L and R gate electrodes via Au bonding wires.

Due to a mechanical fault in one of the transmission lines that manifested at low temperatures, likely caused by mismatched thermal contraction of the metal and dielectric in the coaxial cable, only the transmission line connected to the L gate was functional during the experiments described in chapter 6. Fortunately, only one transmission line was required. The R gate was DC biased as normal.

Figures 3.6 through 3.10 show the dilution refrigerator insert with the shielding removed. Many of the components described in the above paragraphs are visible and identified in these photographs.

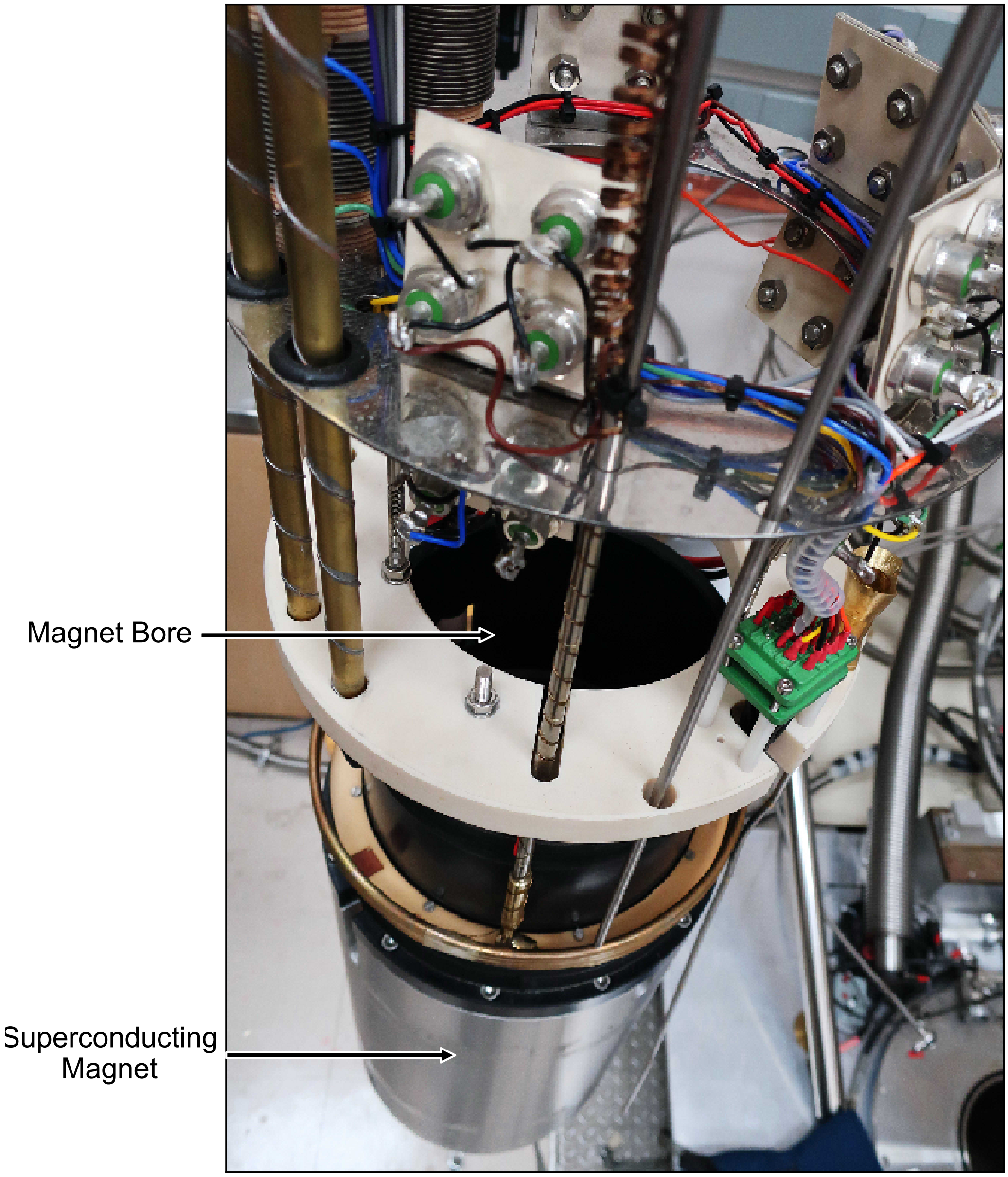

Figure 3.6: 16/18 tesla superconducting magnet assembly for Oxford cryostat, showing the open core where the shielded dilution unit was inserted.

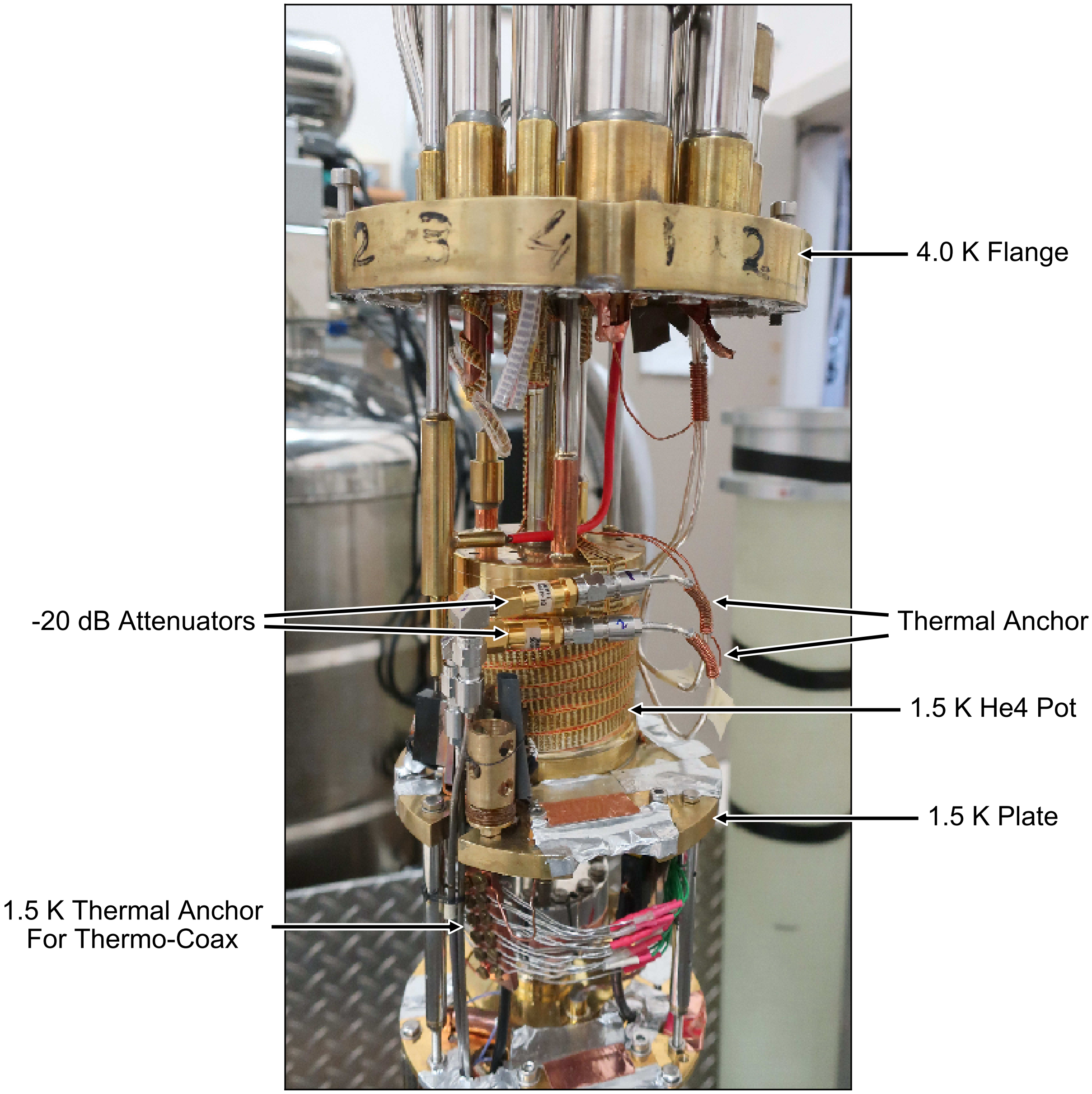

Figure 3.7: Upper body of dilution refrigeration unit. 4 K flange is visible with Indium vacuum seal. Custom wire loom, thermo-coaxial cables, and radio frequency attenuators with copper wire thermal anchoring to the 1.5 K He4 pot are all indicated.

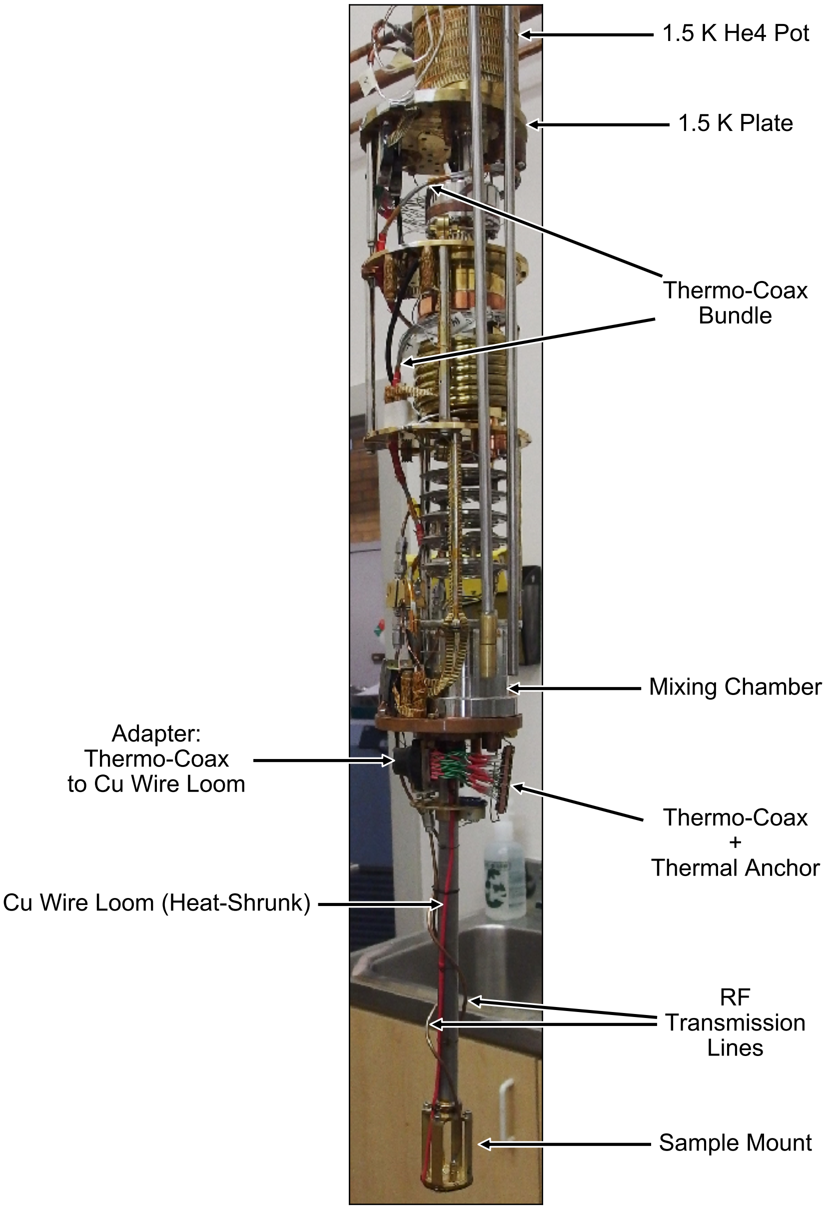

Figure 3.8: Main body of dilution unit with sample mount installed. DC and RF lines are indicated, along with the $1.5\,\mathrm{K}$ *stage and mixing chamber.*

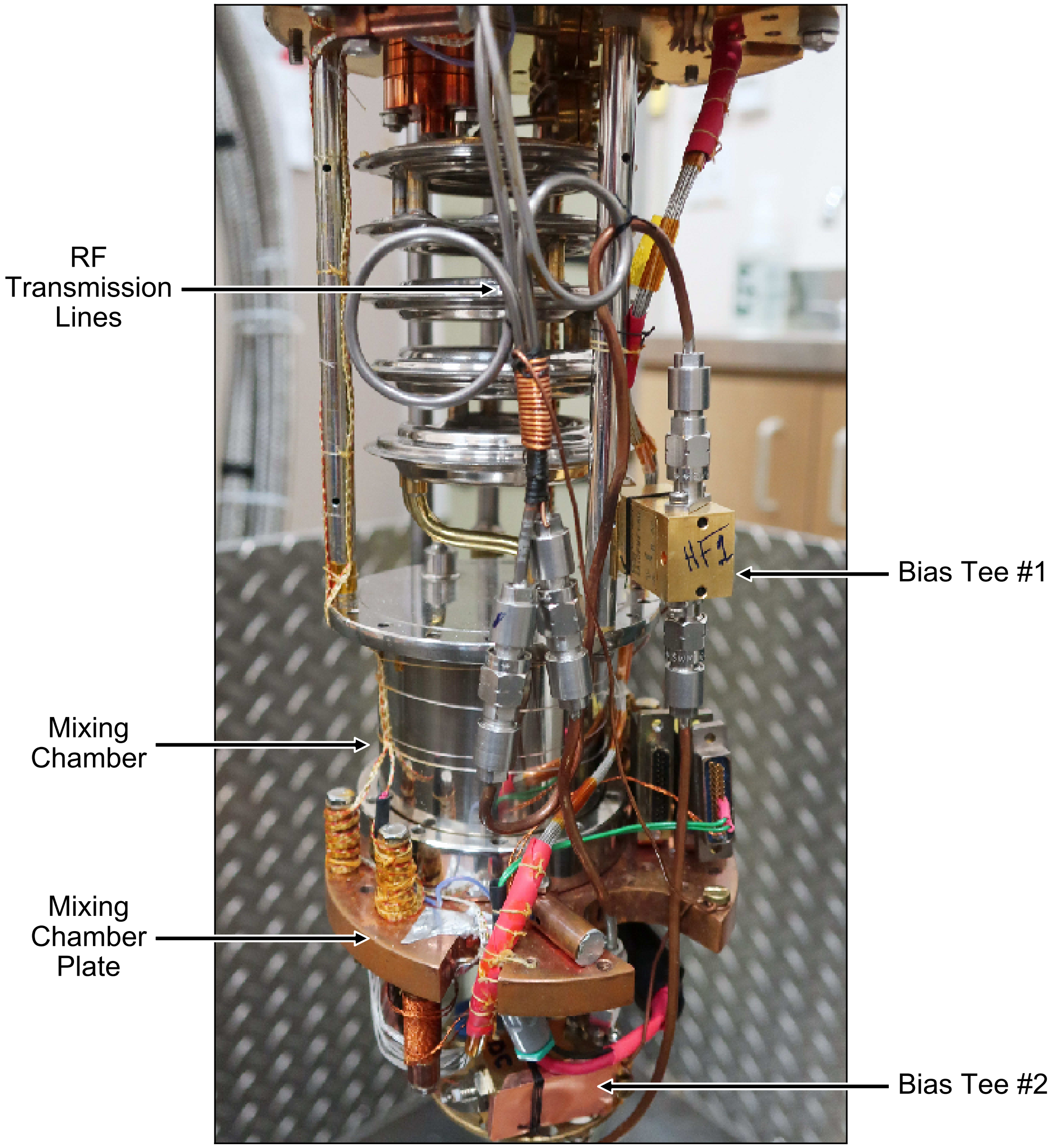

Figure 3.9: Stepped heat exchangers and mixing chamber are visible. The bias tees, indicated in the photograph, are heat-synced to the mixing chamber with copper wire. Below the mixing chamber plate is the sample mount.

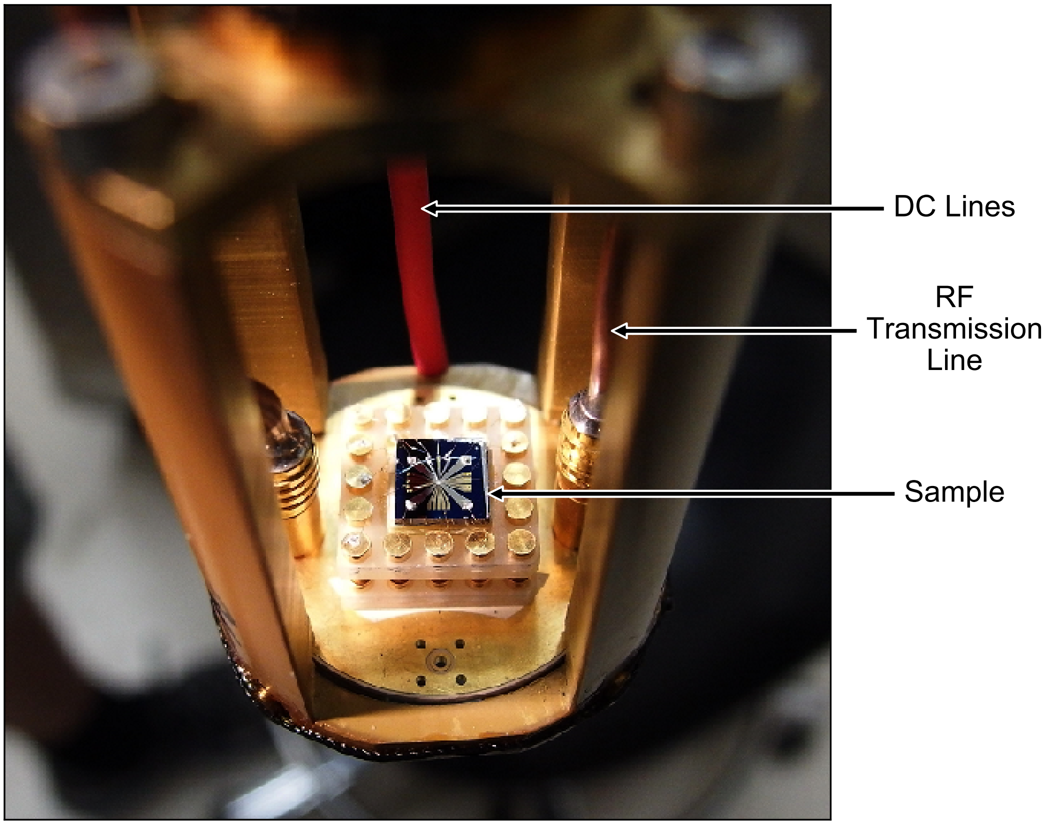

Figure 3.10: Lower part of sample mount and sample header. Sample pictured is the sample used in the experiments. The red wire contains DC lines, which are soldered to the pins from below. Au bolding wires were used to contact the sample.

3.4 Hole Transport Circuit

In the transport configuration, a current was measured through the double quantum dot directly. The measurement circuit show diagramatically in figure 3.11 used for the transport magnetospectroscopy and Landau Zener Stueckelberg Majorana (LZSM) interferometery experiments detailed in chapters 4 and 6.

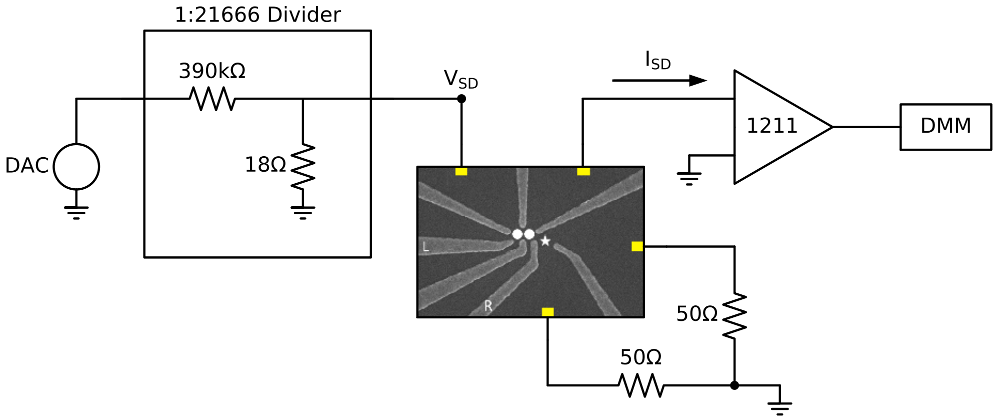

Figure 3.11: Schematic diagram of the bias and measurement circuits used in the transport configuration. Yellow boxes represent contact made with the four reservoirs including the ohmic contacts, DC lines, and filters as discussed in the previous sections. The voltage divider and the virtual ground supplied by the 1211 current amplifier are shown connected to the left and right dot leads respectively. The unused reservoirs were grounded through 50 Ω *terminators.*

A passive 1:10000 voltage divider was used to supply the bias voltage V_{SD} to the left-most dot lead, while the right-most lead was virtually grounded by the current measurement circuit. When measuring transport current, the Ithaco 1211 current pre-amplifier was set to output 10^8 V per A of input current.

3.5 Charge Detection Circuit

In the charge sensing configuration, a current was measured through the quantum point contact and used to infer the charge state of the double quantum dot. The measurement circuit show diagramatically in figure 3.12 was used for the single spin relaxation experiment detailed in chapter 5.

A passive 1:21666 voltage divider was used to supply the bias voltage V_{QPC} to the QPC charge sensor, while the right-most lead was virtually grounded by the current measurement circuit. The bias voltage used in the charge sensing experiments of chapter 5 was $V_{QPC} = 1$ mV. When measuring transport current, the Ithaco 1211 current pre-amplifier was set to output 10^8 V per A of input current. When measuring charge sensor current, the Ithaco 1211 current pre-amplifier was set to output 10^7 V per A of input current.

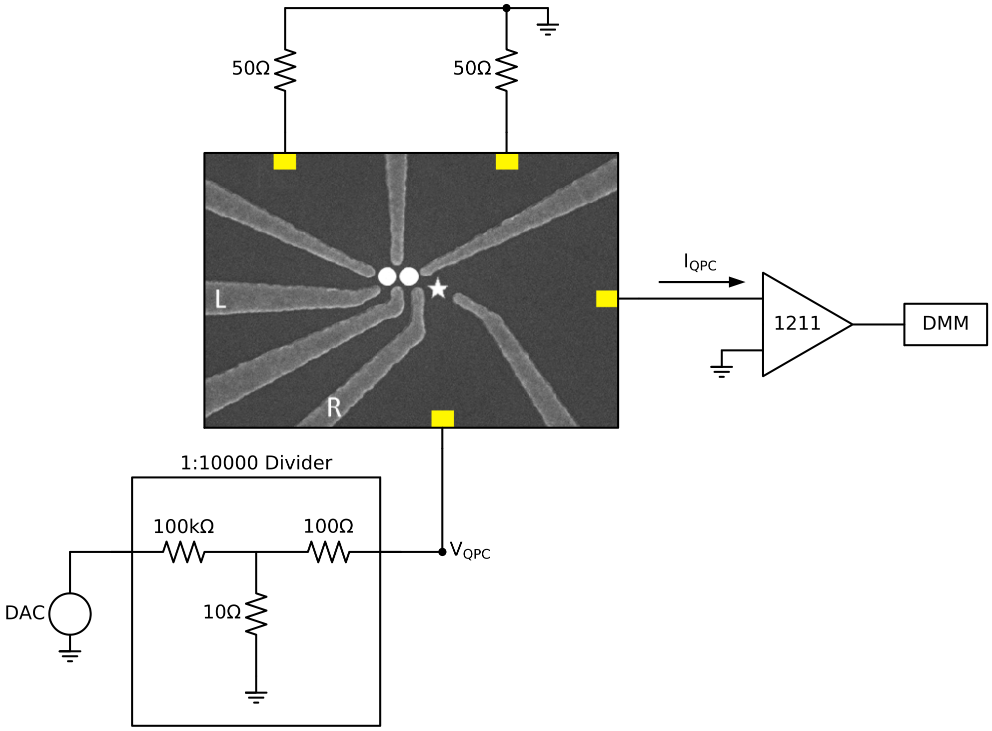

Figure 3.12: Schematic diagram of the bias and measurement circuits used in the charge detection configuration. Yellow boxes represent contact made with the four reservoirs including the ohmic contacts, DC lines, and filters as discussed in the previous sections. The voltage divider and virtual ground supplied by the 1211 current amplifier are shown connected to the two QPC leads. The unused reservoirs were grounded through $50\,\Omega$ *terminators.*

Chapter 4

One and Two Hole Transport Spectroscopy and Spin Blockade

4.1 Charge Transport Through Quantum Dots

A quantum dot is a three dimensional finite potential well in which one or more carriers may be bound. In the case of a GaAs heterostructure such as the one investigated in these studies, confinement is provided in one direction by the vertical band structure of the device, whereas in the remaining two directions it is provided by an electrostatic potential. The electric fields are created by the electrostatic gates, and thus may be tuned by tuning the applied gate voltages.

A source of carriers, holes in this case, is typically provided by a lead. In the case of this structure, the lead is the two-dimensional hole gas outside the quantum dot. The lead is tunnel coupled to the dot by tuning the electrostatic barrier, and depending on the voltage settings on the gates different numbers of charges will occupy the dot at equilibrium [62]. When the energy associated with the addition of a single charge well exceeds the temperature, the charge of the quantum dot is well described by a discrete number of carriers and the eigenstates of the double quantum dot will generally be eigenstates of the charge number operator.

The Coulomb interaction energy of a quantum dot array is that of a capacitor with discrete charge N with an effective applied voltage:

$$E(N) = \frac{(qN)^2}{2C} + \frac{eN}{C}\sum_i C_i(V_i - V_{0i}) \tag{4.1}$$

where C is the total self-capacitance of the quantum dot, V_i is gate voltage setting of gate i, V_{0i} is an offset voltage taking into account the uncontrolled background electric field (chosen such that when $\vec{V_0} = \vec{V}$ the zero charge state has zero energy) and C_i is a capacitance that couples the charges on each gate to the carriers on the dot.

The electrochemical potential, or energy associated with the addition of the $(N+1)$th carrier, is the difference between $E(N+1)$ and $E(N)$:

$$\mu_{N+1} = \frac{e^2}{C}(N + \tfrac{1}{2}) + \frac{e}{C}\sum C_i(V_i - V_{0i}) \tag{4.2}$$

$$\mu_{N+1} = \frac{e^2}{C}(N + \tfrac{1}{2}) + \sum_i \alpha_i(V_i - V_{0i}) \tag{4.3}$$

where a constant charging energy $E_C = \frac{e^2}{C}$ separates successive values of μ_N. Here, α_i calibrates the contribution of gate i to the energy of the excess carrier.

For qualitative interpretations and discussions, it can be helpful to draw energy diagrams such as figure 4.1, which depict the ladder of electrochemical potentials associated with different charge states.

The ground state of a quantum dot connected to a lead will depend on the Fermi level in the lead. At zero temperature, if the Fermi level in the source lead (ϵ_S) exceeds the electrochemical potential of the charge state N, carriers will tunnel from the lead onto the dot until this is no longer true. If the Fermi level is below that charge state, the carriers will tend to tunnel off the dot and into the empty states in the lead. The ground charge state of the quantum dot depends on the Fermi energy and the applied local gate voltages.

If a drain lead is added and is also tunnel coupled to the dot, a second Fermi energy is introduced into the system: ϵ_D. a voltage bias $eV_{SD} = \epsilon_S - \epsilon_D = \epsilon_{SD}$ can be applied and a non-equilibrium condition may be introduced into the system. For finite bias, it is possible for one or more electrochemical potential levels to lie above one Fermi energy but below the other, allowing carriers to tunnel onto the dot from one lead and out of the dot into the other, passing a net current. This current can be measured, and this forms the basis of charge transport measurements. The span of energies between the Fermi energies of the source and drain is called the “bias window”.

For a bias window smaller than the charging energy, current can pass only at certain values of $\vec{V}$. If only one gate is varied, V, the pattern will be periodic in V where the

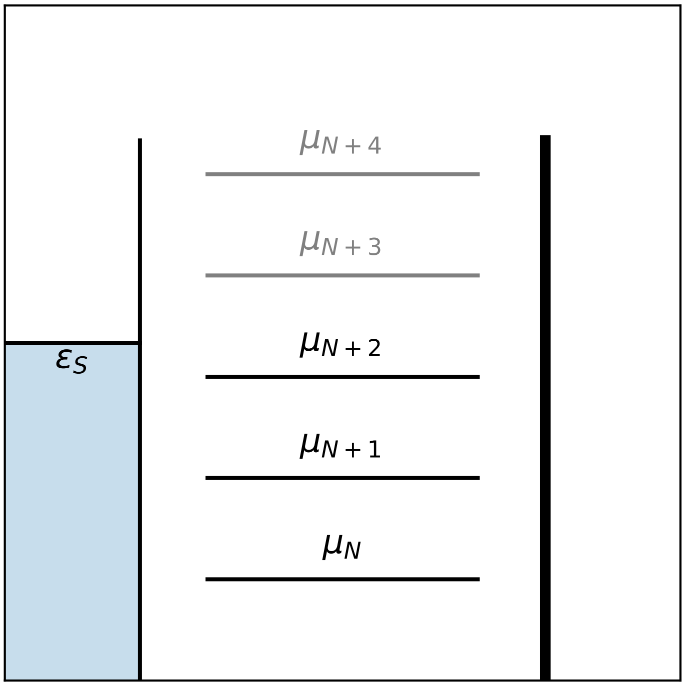

Figure 4.1: Electrochemical potentials of discrete charge states of a single quantum dot, showing the ladder of energies separated by the charging energy $E_C = \frac{e^2}{C}$*. The Fermi level of the source lead (to the left) is also shown.*

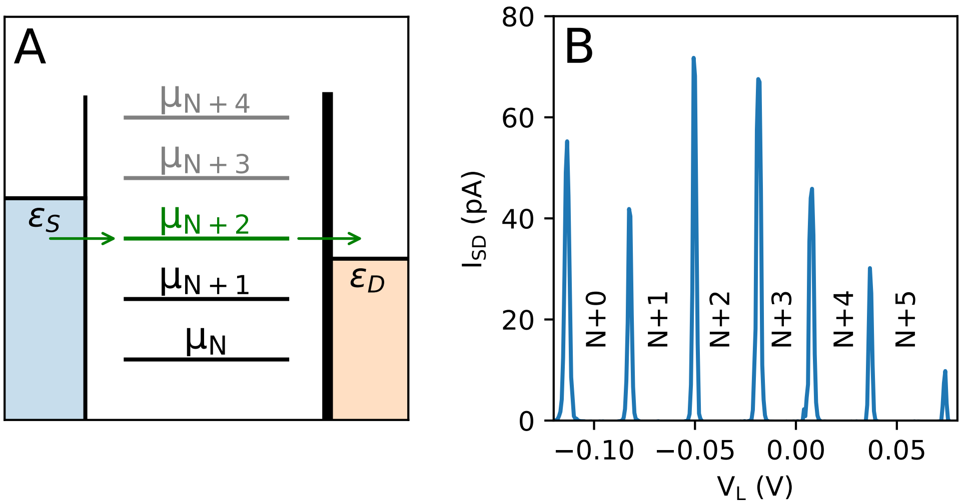

Figure 4.2: ***A****) Energy level diagram showing a condition where current may flow through the quantum dot. The electrochemical potential of the* $N + 2$ *charge state is within the bias window, allowing current to flow.* ***B****) Measured current through the quantum dot. Peaks occur where one of the electrostatic potentials is within the bias window. Between peaks, the charge ground state is constant and each peak marks a change in the average occupancy of the dot.*

period is equal the charging energy $E_C = \alpha^{-1}(V_{i+1} - V_i)$ [1]. Here α^{-1} is the inverted lever arm matrix and V_N is the Nth voltage at which current is observed, corresponding to an instability where the electrochemical potential of the Nth charge state is in the bias window. See figure 4.2, where this phenomenon was observed as a function of the gate voltage L with the device described in chapter 2 tuned in the single dot regime in the He3 dilution refrigerator. The device was tuned in the many-hole regime and N was not known. A bias of $\epsilon_{SD} = 10\,\mu\text{eV}$ was applied.

The width of each peak is a function of both the electron temperature and the lifetimes of the charge states determined by the tunnel barriers to the leads.

A Double Quantum Dot (DQD) is a pair of tunnel coupled quantum dots. Commonly, each quantum dot is connected to a dedicated lead: the left dot is tunnel coupled to the left lead, the right dot is tunnel coupled to the right lead, and each dot is tunnel coupled

---

[1] In the simple quantum capacitor model described by equation 4.1

to the other.

In this configuration, transport is more complex because each dot has its own ladder of energy states, each with its own charging energy, and inter-dot Coulomb interactions become relevant. This complicates equation 4.1:

$$\mu_{(N+1,M)} = E(N+1,M) - E(N,M) = \frac{e^2}{C_L}(N+\tfrac{1}{2}) + \sum \alpha_{Li}(V_i - V_{0i}) + \mathbf{ME_{int}} \tag{4.4}$$

$$\mu_{(N,M+1)} = E(N,M+1) - E(N,M) = \frac{e^2}{C_R}(M+\tfrac{1}{2}) + \sum \alpha_{Ri}(V_i - V_{0i}) + \mathbf{NE_{int}} \tag{4.5}$$

where C_L and C_R are the self-capacitances of the left and right dot respectively, N and M count the existing charges in the left and right dots respectively, and E_{int} is an inter-dot charging energy reflecting the increasing energy cost of adding a carrier to one dot in the presence of a repulsive charge in the coupled dot. α_{Li} $[\alpha_{Ri}]$ is the lever arm representing the contribution of gate i to the energy of the excess carrier in the left [right] dot.

Figure 4.3 panel B shows the current through the double quantum dot as a function of two gate voltages, V_L and V_R applied to gates L and R as identified in figure 2.2. A bias of $\epsilon_{Sd} = 100$ µeV was applied. In the single dot case a single charging energy is visible and Coulomb blockade peaks present as sloped lines in the two-dimensional voltage space where the slope gives the ratio of the $\hat{\alpha}$ matrix elements for gates V_L and V_R: $V_L = -\frac{\alpha_{LR}}{\alpha_{LL}}V_R + V_0$, for example, for some offset V_0. Because the lines separate regions of the voltage space with different ground charge distributions and a charge is added as one of these lines are crossed, in transport spectroscopy these lines are called "addition" lines. In the double dot case two distinct sets of addition lines are visible, corresponding to addition of charges into two different dots. The slopes of these lines give the relative α parameters $\frac{\alpha_{RR}}{\alpha_{RL}}$ and $\frac{\alpha_{LR}}{\alpha_{LL}}$. Also visible is a jump where the addition lines intersect. These jumps reflect the inter-dot charging energy, which displaces the addition lines of one dot when a hole is added to the other. Short lines with positive slope appear when two different charge configurations with the same total charge (for example, (1,0) and (0,1) in figure 4.3 B are equal in energy).

In the single dot case, the dot is coupled to a continuum of states in the source and drain leads and thus elastic tunneling is always possible. In the double quantum dot case, transport involves both elastic and inelastic inter-dot tunneling processes. By definition, elastic or resonant tunneling can occur only if the energy required to transfer a charge from one dot to another is zero, and may be coherent. Conversely, inelastic tunneling requires a source or sink of energy, which is very often provided by the phonon bath in crystaline bulk

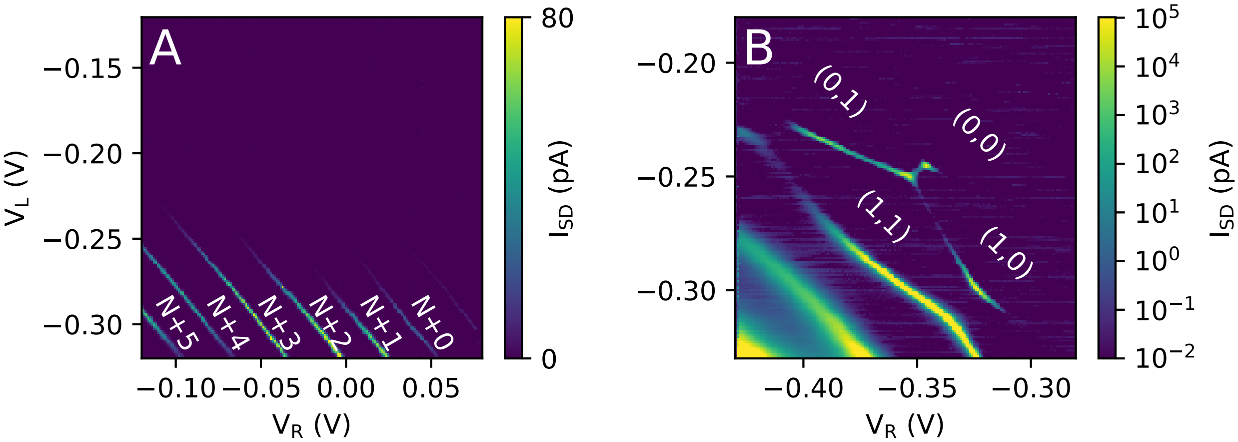

Figure 4.3: ***A****) Coulomb blockade observed in transport as a function of L and R with the device tuned in the single-dot many-hole regime. Current is suppressed as* V_L *becomes more positive because the tunneling barrier to the lead becomes opaque. B) Transport through the same device in the double dot few-hole regime. Transport is enhanced at the two triple degeneracy points at the center of the figure, as well as along some of the addition lines where the tunnel barriers to the leads are more open (toward the bottom left of the image). The total current is sensitive to both* V_L *and* V_R *because the tunnel barriers to the leads change with both voltages.*

GaAs. Because of the involvement of the phonon bath, inelastic tunneling may be slower than resonant tunneling and is incoherent.

Resonant tunneling is visible in figure 4.3 B at the interface between the (1,0) and (0,1) regions, where a short line of positive slope is visible. This “charge transfer line” corresponds to where holes can resonantly tunnel between the (1,0) and (0,1) charge states, leading to a current enhancement. Current is further enhanced at the extremes of the charge transfer line, at the intersection of the (1,0) and (0,1) regions and either the (0,0) or (1,1) regions. At these triple degeneracy points (or “triple points”) three charge states are equal in energy and the DQD can cycle from, for example, (0,0) to (1,0) to (0,1) and back to (0,0) without emitting a phonon. Similarly, a triple point is visible where the (1,1) to (1,0) to (0,1) to (1,1) cycle is resonant. If the bias is reversed, the cycles can simply occur in reverse and the triple points remain visible in DQD current.

Addition lines and transfer lines are more reliably and uniformly visible using charge detection techniques as charge detection is not reliant on the conditions that govern direct

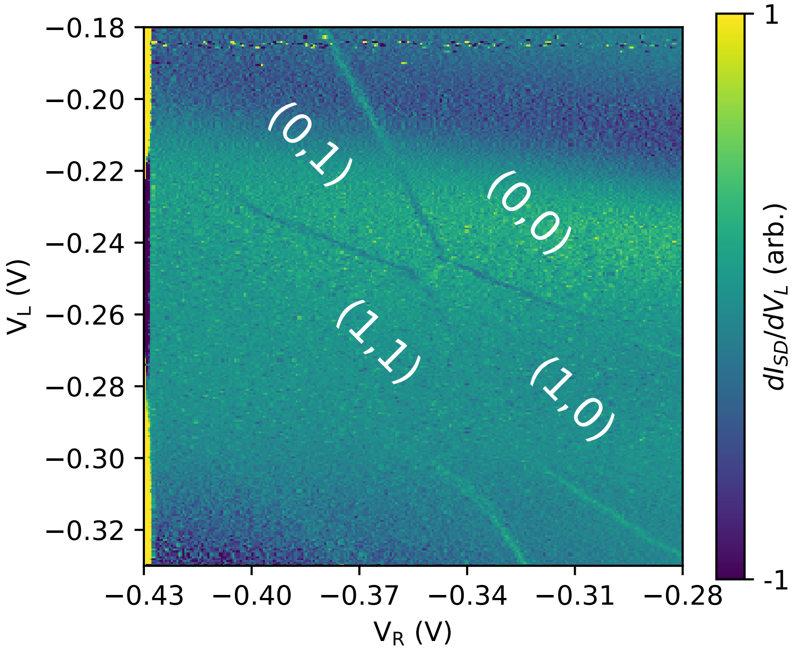

Figure 4.4: Charge sensor current I_{QPC} measured simultaneously with the transport current I_{SD} shown in figure 4.3 B. The current is differentiated to show the discontinuities. Lines with negative slopes are addition lines. The faint line with positive slope at the center of the image is an example of a charge transfer line. Charge ground states are indicated in several regions.

transport, such as relatively open tunnel barriers to the leads. A QPC is a point contact between two leads, the resistance of which is highly sensitive to the electrostatic confinement and therefore to local electrostatic fields such as the ones produced by single holes[60]. As an example, the DQD was configured in the few-hole regime and a 1 mV bias was applied across the QPC near pinch-off $R_{QPC} > 50$ kΩ. In this state, the current through the QPC, I_{QPC}, varied continuously with the local depletion gate voltages but was discontinuous near the addition lines because of the change in DQD charge configuration. Figure 4.4 shows I_{QPC} as a function of V_L and V_R, differentiated along the V_L axis, showing clear addition and transfer lines and serving to confirm that there are no further addition lines in the (0,0) region (because no further carriers could be removed).

4.2 Blockade and High-Bias Transport

Transport through a single quantum dot is suppressed when there are no states in the bias window, as only states in the bias window can be populated from the source *and* empty into the drain to sustain the instability that leads to transport. This current suppression, lifted under specific circumstances, is called Coulomb blockade.

Current blockade may occur in double quantum dots even if one or more states are within the bias window because of the inter-dot charging energy. For example, under positive bias, suppose the (1,0) charge state could be populated by tunneling a hole from the left lead (source) into the left dot. If the (0,1) charge state is above the (1,0) state in energy, however, the (0,1) state cannot necessarily empty into the drain even if there is an empty state of equal energy in the drain lead. Figure 4.5 panel B depicts this situation. The (1,0) state in this case is meta-stable, and will prevent the flow of current. Gate voltages may be adjusted to detune the (0,1) state below the (1,0) state to lift the blockade, provided both states remain in the bias window.

In the space of voltage values for any two gates (V_L, V_R) with all other gates held constant, there exist triangular regions of voltage space where this form of current blockade is lifted. The edges of the transport regions are defined by the three conditions that must be met to enable transport. If the transport cycle is (0,0) → (1,0) → (0,1) → (0,0) for example, then:

1. $\epsilon_S >= E_{(1,0)} - E_{(0,0)}$. There is a filled state in the source to charge the left dot.
2. $E_{(1,0)} >= E_{(0,1)}$. Tunneling from left to right is possible without energy input.
3. $E_{(0,1)} - E_{(0,0)} >= \epsilon_D$. There is an empty state in the drain to receive the right hole.

The range of voltages that satisfy all three criteria for the (0,0), (1,0), (0,1) cycle is not the same as for the (1,1), (1,0), (0,1) cycle:

1. $\epsilon_S >= E_{(1,1)} - E_{(0,1)}$. There is a filled state in the source to charge the left dot.
2. $E_{(1,1)} - E_{(1,0)} >= \epsilon_D$. There is an empty state in the drain to receive the right hole.
3. $E_{(1,0)} >= E_{(0,1)}$. Tunneling from left to right is possible without energy input.

The inter-dot tunneling condition is identical for both cycles, so one of the edges in

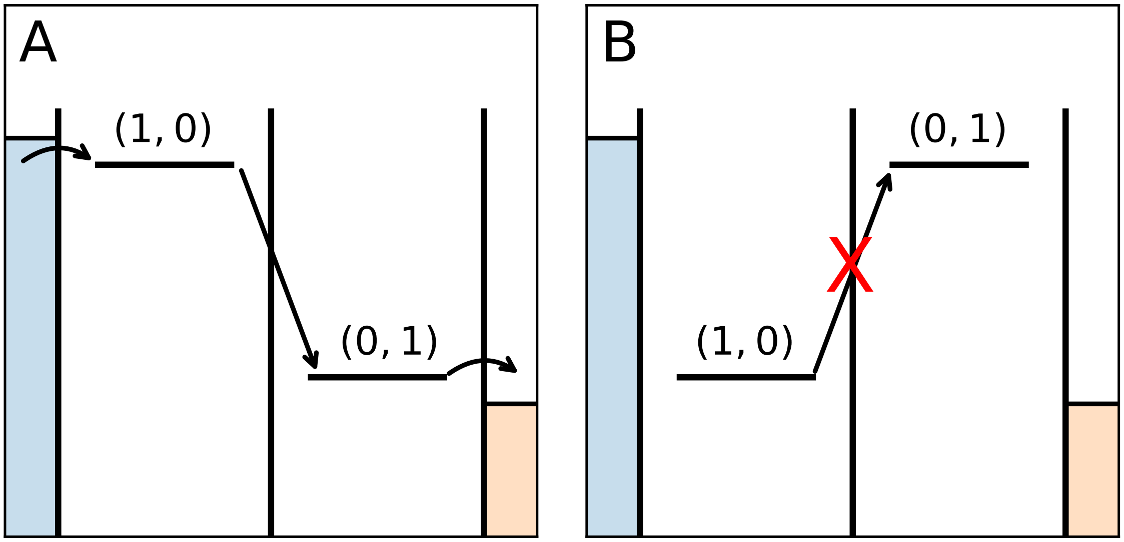

Figure 4.5: ***A****) A configuration of energy levels that supports transport through a double quantum dot. Each dot has one level in the bias window. A single carrier may tunnel into the left dot from the source lead. That carrier may inelastically tunnel (downward arrow) to the right dot and then out to the right lead. This process can repeat to support current.* ***B****) Because of the ordering of the energy levels, the carrier becomes trapped in the meta-stable (1,0) charge state in this configuration and the double quantum dot is blockaded. If the bias were reversed or the detuning were reversed, blockade would be lifted.*

each transport triangle should be colinear with a corresponding edge in the other triangle. The other two inequalities are shifted by a constant ($E_{(1,1)} - E_{(1,0)} = E_{(1,0)} - E_{(0,0)} + \mathbf{E_{int}} + (\mathbf{E_{CL}} - \mathbf{E_{CR}})$). This constant shift is equivalent to a shift in $\vec{V_0}$ in equations 4.4 and 4.5, and so the other two pairs of edges should be parallel.

For a charge state x it is convenient to define the energy quantity $\epsilon_x = E_x - E_{(0,0)}$ in the context of the cycle involving the (0,0) charge state and $\epsilon_x = E_{(1,1)} - E_x$ for the triangle involving (1,1). If we do so, the transport conditions can be re-written the same way for both triangles:

1. $\epsilon_S > \epsilon_{(1,0)}$.
2. $\epsilon_{(1,0)} > \epsilon_{(0,1)}$.
3. $\epsilon_{(0,1)} > \epsilon_D$.

Taking the limit where $\epsilon_D = \epsilon_S = \epsilon_f$ it's clear that each triangle must include one triple point: $\epsilon_{(1,0)} = \epsilon_{(0,1)} = \epsilon_f$ where ϵ_f is by definition the energy of either the (0,0) or the (1,1) state with one excess or missing hole in a lead (respectively) to compensate.

This approach applies with no loss of generality to transport through states that involve many holes.

For example, a bias of $\epsilon_{SD} = -2\,\text{meV}$ was applied across the device and transport was observed near the triple points at the intersections of (1,0), (2,0), (1,1), and (2,1) regions. The results are presented in figure 4.6. Panel A shows a charge stability diagram for reference, showing that indeed the device is being operated in the few-hole regime. Panel B shows two overlapping triangular regions of current, which share a base as predicted, and includes an overlay to show that the triangles extend from what would be the triple points for small bias. In both triangles, the base features a resonant current enhancement, which can be explained by the precise alignment of (2,0) and (1,1). We can define the detuning $\Delta\epsilon = \epsilon_{(1,0)} - \epsilon_{(0,1)}$ and see that the bright line at the base of the triangle corresponds to zero detuning, $\Delta\epsilon = 0$.

The size of each triangle should be proportional to the source drain bias applied, given the established conditions. Figure 4.7 shows the same experiment repeated for different bias voltages $V_{SD} = \epsilon_{SD}/q$, showing that this is indeed the case.

In later sections, high bias transport will be used to perform magneto-spectroscopy on the states of the double quantum dot. However, the immediately following section will discuss how high bias transport can be used to calibrate the lever arm matrix $\hat{\alpha}$ in the

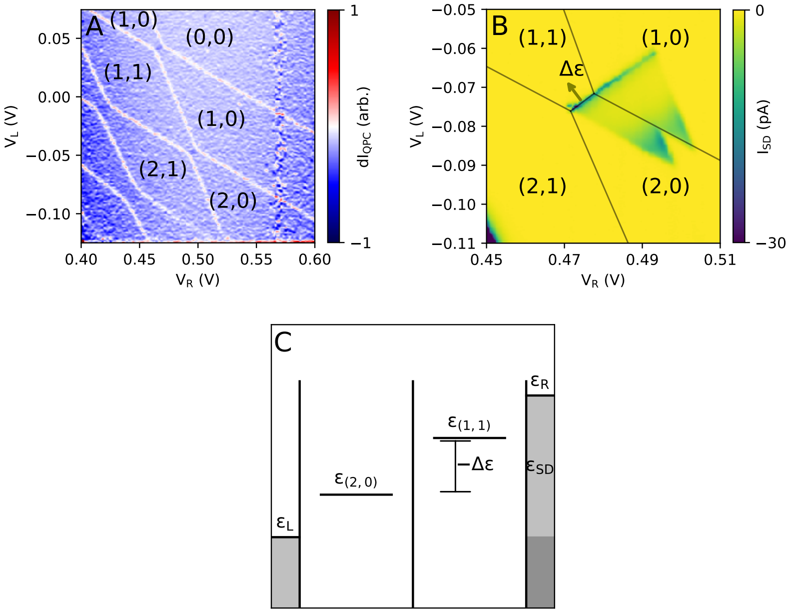

Figure 4.6: ***A****) Example of a charge stability diagram showing regions of gate voltage space defined by different ground states of definite charge. The QPC current is measured and differentiated with respect to* V_L *to highlight the abrupt changes in the charge sensor current at the boundaries between stable charge regions.* ***B****) Example of triangular charge transport features at finite bias,* $V_{DC} = 1.6\ mV$ *or* $\epsilon_{SD} = 1.6\ meV$*. Source drain current is measured directly. A sketch of the charge stability regions at zero bias is overlaid on the raw data. The triangles extend from the triple degeneracy points with this source-drain biasing scheme. Directed arrow indicates increasing* $\Delta\epsilon$*.* ***C****) Level diagram showing the charge states that participate in inter-dot tunneling: (2,0) with energy* $\epsilon_{(2,0)}$ *and (1,1) with energy* $\epsilon_{(1,1)}$*. Also shown are the Fermi levels, with energy* ϵ_L *and* ϵ_R*, and the bias window spanning a range of* ϵ_{LR}*.*

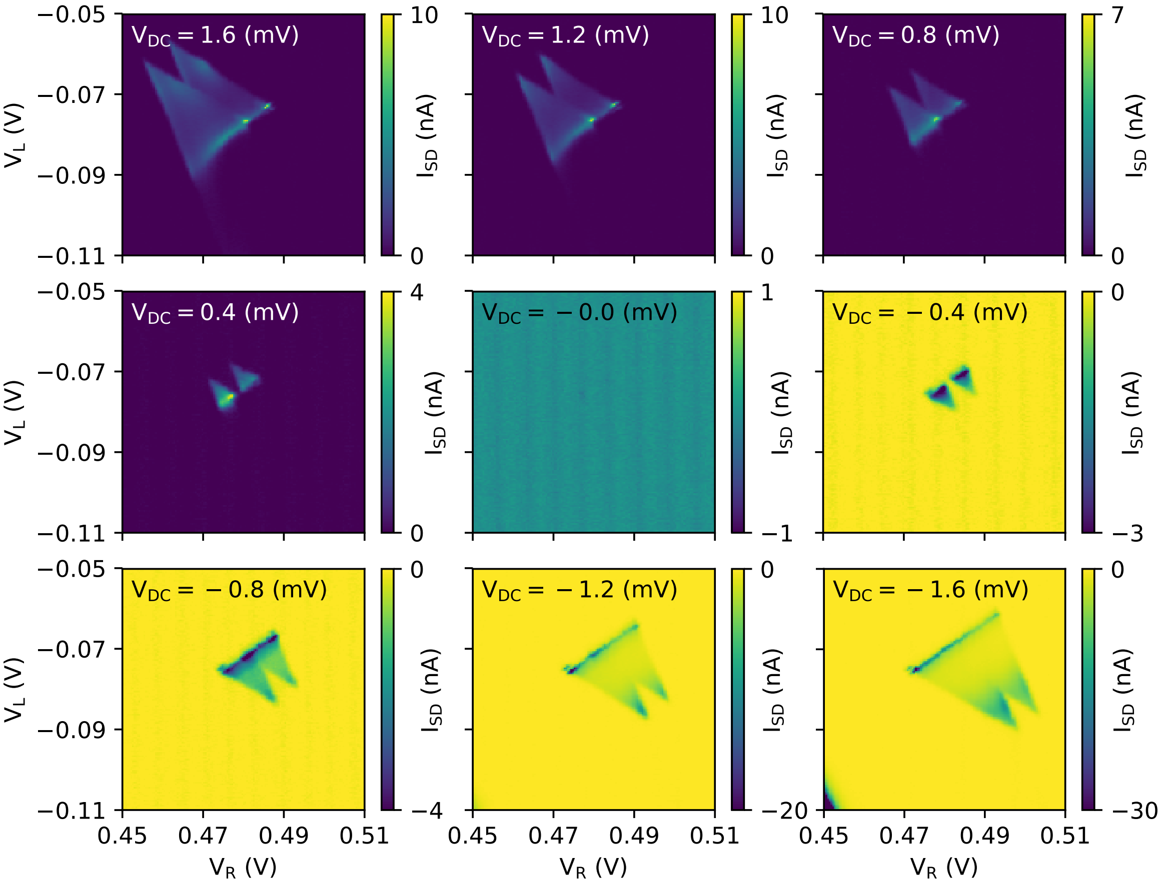

Figure 4.7: Observation of charge transport through the double quantum dot as a function of the left and right gate voltages (V_L, V_R) and applied bias (V_{DC}) showing triangular features in voltage space.

double quantum dot so that transport spectroscopy may be performed in terms of energy instead of voltage.

4.3 Transport Calibration of Lever Arms

To obtain the lever arm matrix from high bias transport measurements, one must first identify a gate set. In principle if there are N gates, two leads, and two dots, then $\hat{\alpha}$ in equations 4.4 and 4.5 is an $N+2$ by 2 matrix. Typically it suffices to find the lever arms for one or two gates at a time. For spectroscopy, the most important gates to calibrate are the one or two that are varied to detune the double quantum dot.

This method produces the lever arm elements for two particularly chosen gates, though in principle it can be applied to any two gates to obtain every lever arm.

The calibration data was obtained by measuring I_{SD} as a function of V_L and V_R using the transport circuit and a source-drain bias of $\epsilon_{SD} = 2$ mV and is shown in figure 4.8 panel A.

Consider the three specific points in voltage space recorded in figure 4.8: $(V_{L\blacktriangle}, V_{R\blacktriangle})$, $(V_{L\blacktriangledown}, V_{R\blacktriangledown})$, and $(V_{L\bullet}, V_{R\bullet})$.

$$\begin{bmatrix} \epsilon_{10} \\ \epsilon_{01} \end{bmatrix} = \begin{bmatrix} \alpha_{LL} & \alpha_{RL} \\ \alpha_{LR} & \alpha_{RR} \end{bmatrix} \begin{bmatrix} V_L \\ V_R \end{bmatrix} \tag{4.6}$$

$$\epsilon_{10}(V_L, V_R) = \alpha_{LL}V_L + \alpha_{LR}V_R \tag{4.7}$$

$$\epsilon_{01}(V_L, V_R) = \alpha_{RL}V_L + \alpha_{RR}V_R \tag{4.8}$$

$$\Delta\epsilon = \alpha_{LL}V_L + \alpha_{LR}V_R - \alpha_{RL}V_L + \alpha_{RR}V_R \tag{4.9}$$

At each of the three points, the alignment of both energy levels with the Fermi levels in the leads are known. We can therefore obtain four equations with four unknowns:

$$eV_{DC} = \alpha_{LL}V_{L\blacktriangle} + \alpha_{LR}V_{R\blacktriangle} - \alpha_{RL}V_{L\blacktriangle} - \alpha_{RR}V_{R\blacktriangle} \tag{4.10}$$

$$eV_{DC} = \alpha_{LL}V_{L\bullet} + \alpha_{LR}V_{R\bullet} - \alpha_{RL}V_{L\blacktriangledown} - \alpha_{RR}V_{R\blacktriangledown} \tag{4.11}$$

$$eV_{DC} = \alpha_{LL}V_{L\bullet} + \alpha_{LR}V_{R\bullet} - \alpha_{RL}V_{L\blacktriangle} - \alpha_{RR}V_{R\blacktriangle} \tag{4.12}$$

$$0 = \alpha_{LL}V_{L\blacktriangledown} + \alpha_{LR}V_{R\blacktriangledown} - \alpha_{RL}V_{L\blacktriangle} - \alpha_{RR}V_{R\blacktriangle} \tag{4.13}$$

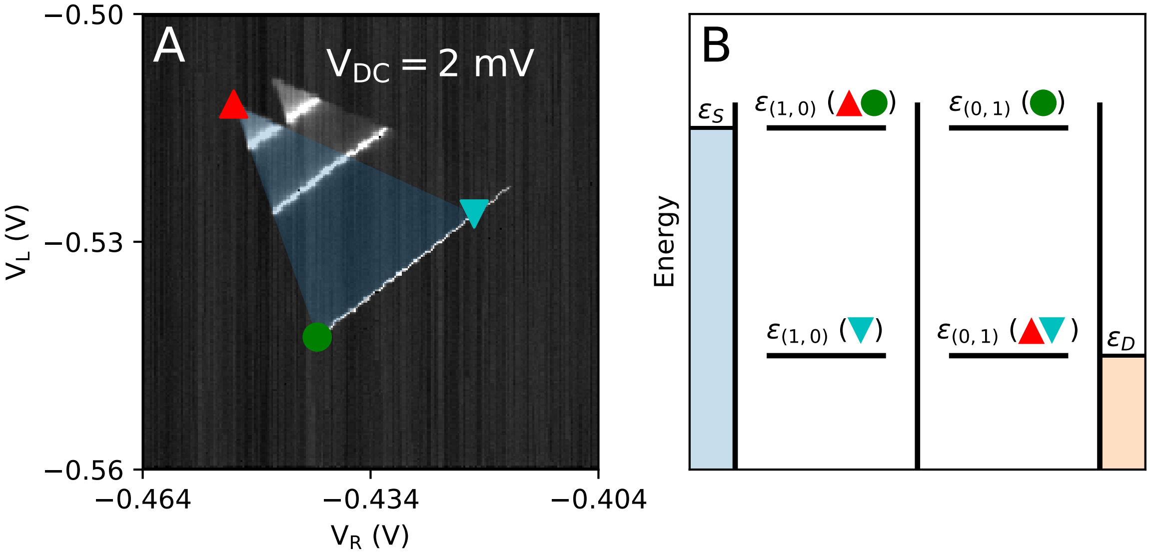

Figure 4.8: ***A****) Triangular transport region in the single hole occupation regime. Two triangles appear, here overlapping, with the lower triangle shaded in blue. The vertices of the triangle are identified by three symbols.* ***B****) Alignments of energy levels at each of the three identified vertices. For example, at the blue downward-facing triangle,* $\epsilon_{(1,0)} = \epsilon_{(0,1)} = \epsilon_D$

Using $V_{DC} = -2$ meV, one obtains for the alpha parameters:

$$\alpha_{LL} = 78 \text{ meV/V} \tag{4.14}$$

$$\alpha_{LR} = 32 \text{ meV/V} \tag{4.15}$$

$$\alpha_{RL} = 29 \text{ meV/V} \tag{4.16}$$

$$\alpha_{RR} = 61 \text{ meV/V} \tag{4.17}$$

This gives the detuning of the two energy levels at any point in voltage space, according to:

$$\Delta\epsilon = \alpha_{LL} V_L + \alpha_{LR} V_R - \alpha_{RL} V_L - \alpha_{RR} V_R \tag{4.18}$$

or:

$$\Delta\epsilon = 49 \text{ meV/V } V_L - 29 \text{ meV/V } V_R \tag{4.19}$$

In the next section, transport magneto-spectroscopy as a function of a calibrated detuning will be applied to measure the effective g-factor of a single hole in a quantum dot.

4.4 Single Hole g-Factor Via Transport Spectroscopy

In previous sections, it was observed that elastic (i.e. resonant) inter-dot tunneling can be more efficient because no energy is absorbed or emitted in tunneling, and a bright zero-detuning line was observed in a high-bias triangle and attributed to this resonant enhancement of tunneling. In fact, the current inside the un-blockaded region in figure 4.8 displays several sharp resonances at finite detuning as well. These resonances correspond to transitions between the (1,0) ground state and several different states of the (0,1) manifold, including orbital excited states. In earlier discussion of quantum dots orbital excited states were ignored, but in general orbital degrees of freedom can create a number of bound excited states with the same charge. These states will not be discussed in detail here. However, the mechanism by which they become visible in transport will be used in most of the following studies.

Transport blockade occurs when the DQD enters a meta-stable state, which will eventually occur if the lowest accessible energy state in the bias window is not directly coupled to the drain. For example, if the orbital ground state of (1,0) is below the orbital ground state of (0,1) for positive bias, the DQD will become blockaded. It should be noted that in high bias transport, higher excited states of (1,0) might become populated instead of the ground state, but eventually either the ground state will receive a hole or an excited state of (1,0) will relax into a ground state before transfering the hole to (0,1) and the DQD will become blockaded.

This blockade will be lifted when the ground state of (1,0) is at least equal in energy to the ground state of the (0,1) manifold for positive bias, and we have seen in the previous two sections that in fact a resonant enhancement to the current occurs when the two ground states are energetically aligned. In fact, this resonant enhancement is not unique to the (1,0) to (0,1) transition or to the transition to the (0,1) ground state. If transport requires a transition from one charge configuration to another, then a resonant enhancement may be expected when the ground state of the initial configuration is resonant with any ground or excited state of the destination configuration. Here the initial charge configuration will be refered to as the "emitter" and the final configuration will be called the "receiver". Figure 4.9 illustrates the concept.

This form of transport spectroscopy is similar to Coulomb blockade spectroscopy [63] at high bias, where multiple states of a quantum dot can be resolved as a function of increasing bias. This technique provides a single reference state, the emitter state, with known energy and spin. The spectroscopy therefore reveals more specific information about the nature of the transition between states in addition to the target state's energy.

To acquire the spectrum of states in the (0,1) charge state, a bias of $\epsilon_{SD} = 2\,\mathrm{mV}$ was applied across the device in the single hole regime near the (0,0),(1,0),(0,1),(1,1) triple points and I_{SD} was measured. The current is plotted in figure 4.10 for two values of the magnetic field B oriented in the z direction and over a range of values of V_L and V_R, showing that the uniform current resonance at the base of the triangle (the zero detuning line) splits into two for a finite applied field.

A spectrum was acquired by fixing V_R at $-0.43\,\mathrm{V}$ and sweeping V_L as a function of B. The result, plotted in figure 4.11, shows two current resonances that diverge linearly with field and are degenerate at zero field.

The resonances were fitted against a numerical model of the single hole tunneling that included spin relaxation, inter-dot inelastic tunneling, and spin decoherence, explained in detail in [64] and in appendix A. In the (0,$\Downarrow$), (0,$\Uparrow$), ($\Downarrow$, 0), ($\Uparrow$, 0) basis, the system was modeled using the following Hamiltonian:

$$H = \begin{bmatrix} \frac{\Delta\epsilon}{2} + \frac{E_Z}{2} & 0 & -t_N & -it_F \\ 0 & \frac{\Delta\epsilon}{2} - \frac{E_Z}{2} & -it_F & -t_N \\ -t_N & it_F & -\frac{\Delta\epsilon}{2} + \frac{E_Z}{2} & 0 \\ it_F & -t_N & 0 & -\frac{\Delta\epsilon}{2} - \frac{E_Z}{2} \end{bmatrix} \tag{4.20}$$

The tunneling matrix elements t_F and t_N couple different charge states of similar (t_N) and dissimilar (t_F) spin, such that the transition associated with t_F includes a spin flip and t_N does not flip the spin. Notably, the phase factors i and $-i$ for the t_F matrix elements are somewhat arbitrary and cosmetic in the above Hamiltonian. In principle t_F may be a complex number, and the transport experiments in this chapter can only reveal the absolute value. The imaginary part of the tunneling matrix element is contributed by the Dresselhaus spin orbit interaction, whereas the real part is contributed by the Rashba interaction. As will be shown, the Dresselhaus interaction is apparently present, and hence the choice of phase.

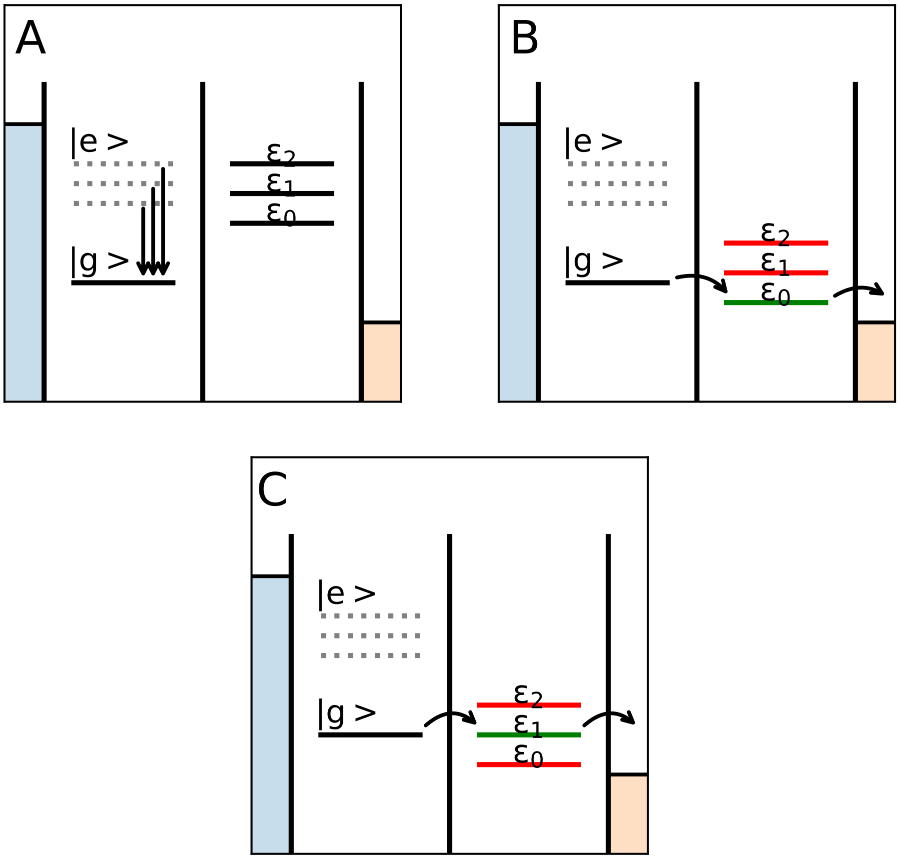

Figure 4.9: Schematic illustrating the mechanism of transport spectroscopy. Carriers from the energetically elevated lead (left) can enter the emitter quantum dot (left) in one of many possible states of a particular charge distribution. Carriers may then directly tunnel into states of the receiver dot that are of equal or lesser energy, and will do so more efficiently on resonance. ***A****) Diagram showing that populated excited states of the emitter can decay into the ground state (downward arrows) to cause blockade if the ground state of the emitter is lower in energy than the ground state of the receiver.* ***B****) If the emitter is not blockaded, the current may increase with each inter-dot transition that becomes energetically allowed.* ***C****) Current through the double quantum dot is further enhanced when the ground state of the emitter dot is resonant with an energy level of the receiver dot. As a function of detuning, the positions of resonant peaks and discontinuities in the current correspond to energy eigenstates localized in the receiver dot.*

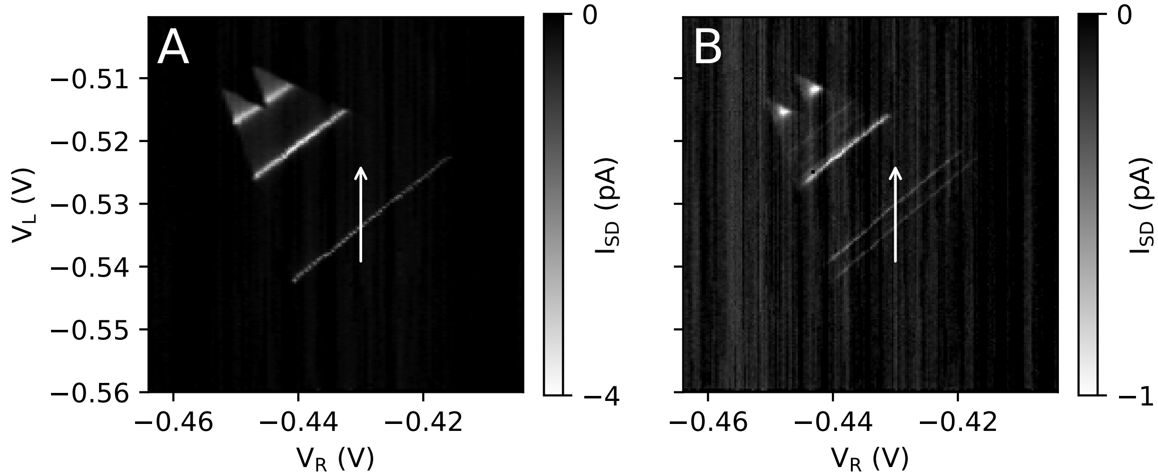

Figure 4.10: Transport spectra of the (0,1) charge state ***A****) for* $B = 0$ *and* ***B****)* $B = 2.0$ T*. White arrows indicate the sweep line for the spectrum shown in figure 4.11.*

Additional fitting parameters to the model included the mean tunneling rates from the source lead into the (1,0) state (Γ_i) and from the (0,1) state into the drain lead (Γ_o). Also included were the single-dot mean spin relaxation lifetime (T_{1S}, corresponding to relaxation within a single dot), an inelastic inter-dot spin flip tunneling lifetime (T_{1F}, corresponding to the inter-dot spin-flipping transition), the spin non-flipping lifetime (T_{1N}, modeling the lifetime of spin conserving inter-dot transitions), the associated phase decoherence lifetimes (T_{2F} and T_{2N}) and finally the coherent tunneling matrix elements t_F and t_N. These mean lifetimes are inverses of the tunneling rates between related states. Table 4.1 summarizes the model parameters used to fit the data for different values of magnetic field. Finally, figure 4.12 plots the two tunneling matrix elements.

Figure 4.12 shows that the two tunneling matrix elements behave somewhat differently. As explained in [65] and [64], t_N is expected to decrease with increasing magnetic field because a tightening of the (1,0) and (0,1) cyclotron orbitals causes a reduced overlap between them as B increases. t_F decrease for the same reason at large enough B, though it initially increases. In the analysis presented in [64], the Dresselhaus spin-orbit contribution to the spin flip matrix element contains a term that is proportional to B^2, to which this initial increase may be attributed. The values of t_N and t_F become comparable at $B = 0.7$ T and remain of a similar order for larger fields.

B (T)	0.5
Γ_i (GHz)	2.0
Γ_o (GHz)	2.0
T_{1S} (µs)	0.75
T_{1N} (µs)	2.7
T_{1F} (µs)	2.4
T_{2F} (ps)	80
T_{2N} (ps)	80

Table 4.1: Parameter values used to reproduce the transport current observed in figure 4.11. A single value T_2 was used for both T_{2F} and T_{2N}.

The spin-flip tunnel couplings can be expected to increase with increasing field as though the vector potential were effectively contributing to the momentum operator. In [64, 65], a microscopic theory modeling the behaviour observed here was developed in more detail.

While coherence (T_1, T_2) parameters can in principle be estimated from these data, there are complications in interpreting them. The T_2 values are decoherence values in the tunneling regime. The decoherence effects of tunneling to and from the leads (at random times) are similar to phase decoherence of the four states within the double quantum dot itself. In chapter 6, a second transport experiment will be presented where the coherence of the inter-dot tunneling was independently measured and the T_2 values in table 4.1 are consistent with the fitting parameters obtained in those experiments. T_{1S} was also measured by an independent experiment explained in chapter 5, which studied spin relaxation in a different regime, where a single hole was isolated in a single quantum dot. In that experiment the value of T_{1S} was found to vary by several orders of magnitude over the field range from $B = 0.5$ to $B = 1.5$ T. The value of T_{1S} found here is relatively field-independent, suggesting a different relaxation mechanism is dominant in the transport regime explored here.

In addition to modeling the line-shapes to extract coherence, relaxation, and tunneling parameters, it is possible to extract information from the positions of the resonances as well.

At finite field, the $(\Downarrow,0)$ to $(0,\Downarrow)$ and $(\Uparrow,0)$ to $(0,\Uparrow)$ transitions are simultaneously resonant at $\Delta\epsilon = 0$. At $\Delta\epsilon = E_Z$, the $(\Downarrow,0)$ to $(0,\Uparrow)$ resonance is active. At $\Delta\epsilon = -E_Z$, the $(\Uparrow,0)$ to $(0,\Downarrow)$ transition is active. These resonance conditions are illustrated in figure 4.13. At zero field, all four resonances are simultaneously active when $\Delta\epsilon = E_Z = 0$. However, for finite E_Z the $(\Uparrow,0)$ to $(0,\Downarrow)$ transition occurs at $\Delta\epsilon = -E_Z$ and the current is expected to be energetically blockaded by occupation of the $(\Downarrow,0)$ state as illustrated in figure 4.13

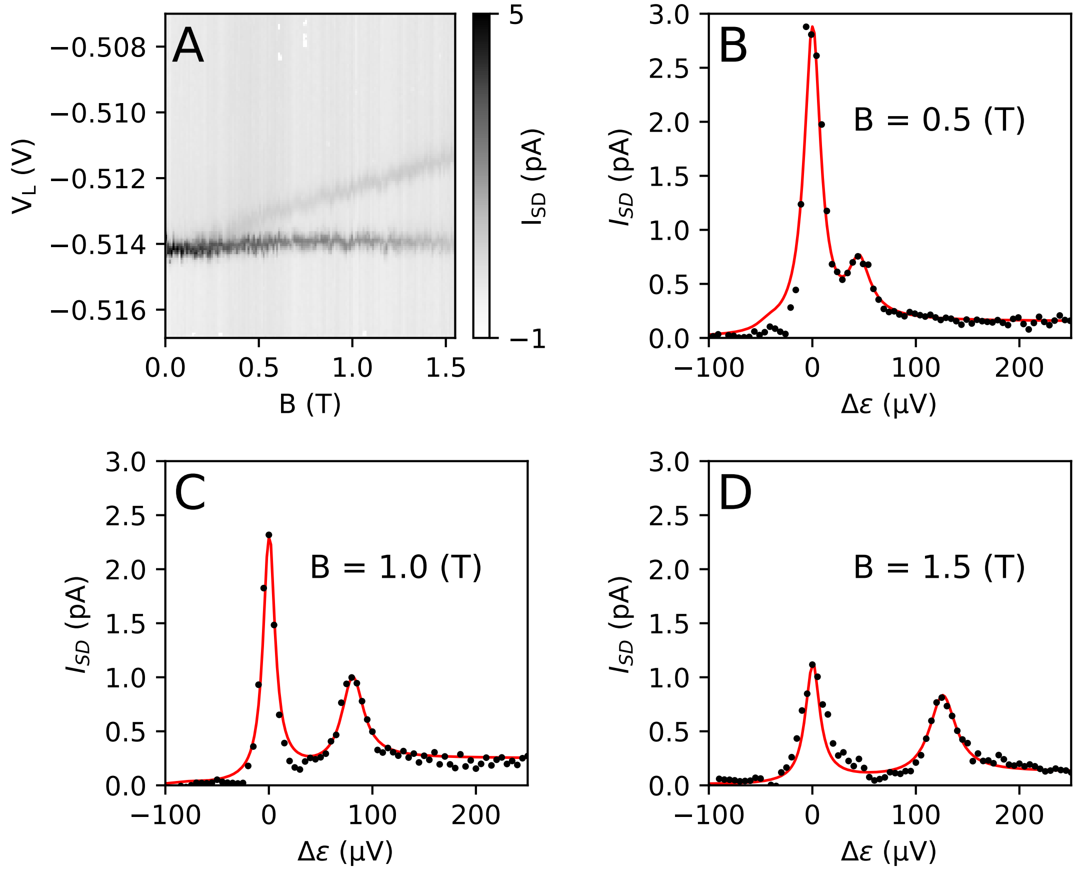

*Figure 4.11: **A**) Transport spectra of the (0,1) state showing the divergence of (0,⇓) and (0,⇑) with increasing B. **B-D**) Transport spectra at the indicated applied fields and fits to a numerical model (solid red curves).*

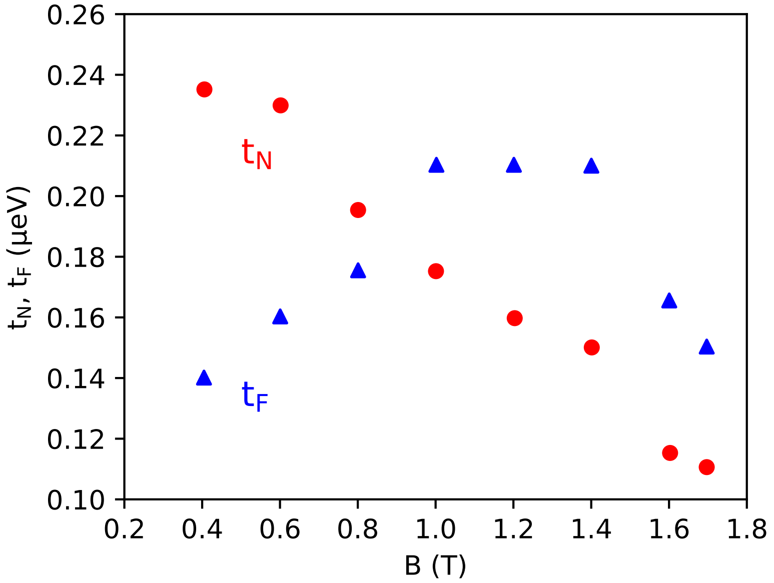

Figure 4.12: Tunneling matrix parameters t_F (blue triangles) and t_N (red circles) extracted by fitting transport spectra as a function of magnetic field.

panel C. Thus, only two resonances can be expected to be visible in transport and they can be expected to diverge linearly with increasing field, as was observed. The energy displacement between the two resonances follows $\Delta\epsilon = E_Z = g^*\mu_B B$, which serves as a measurement of the effective g-factor.

In the spectra plotted in 4.11, the divergence is $\frac{E_Z}{B} = 76.7 \pm 3.8\ \mu\mathrm{V\,T^{-1}}$, giving $g^* = 1.33 \pm 0.07$.

In the following section, a transport magnetospectroscopy experiment will be presented in the two-hole regime with a focus on extracting information about the effective g-factor as a function of magnetic field *orientation*.

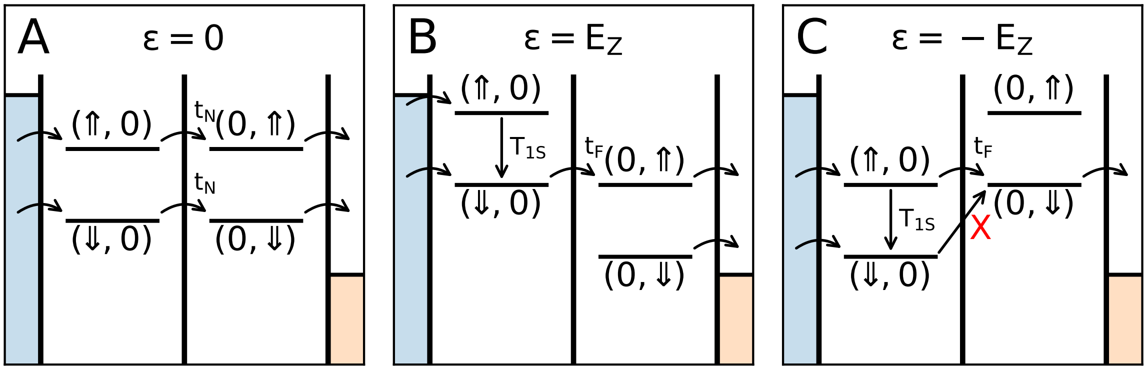

Figure 4.13: ***A****) Schematic of the* $\epsilon = 0$ *resonance, showing the two simultaneously active spin-preserving transitions.* ***B****) Schematic of the* $\epsilon = E_Z$ *resonance, where a single spin-flipping transition (aided by* T_{1S} *spin relaxation)enables a resonance enhancement of the current.* ***C****) Schematic of the* $\epsilon = E_Z$ *resonance, where a single spin-flipping transition (aided by* T_{1S} *spin relaxation)enables a resonance enhancement of the current.*

4.5 Two Hole Magnetospectroscopy

Previously, the transport spectra of a singly occupied quantum dot was examined and a single measurement of the effective g-factor, g^*, was made in that regime. In this section, the transport spectra of a doubly occupied quantum dot (2,0) will be examined as probed by the (1,1) ground state of a double quantum dot. The spectra will be used to extract information on the anisotropy of the effective hole g-factor with respect to the orientation of the applied magnetic field.

The spin physics of a doubly occupied quantum dot are richer than that of a singly occupied quantum dot due to the presence of exchange. For electrons in GaAs, with spin 1/2, the possible eigenvalues of the total spin of two particles are 0 and 1 and the eigenvalues of the spin projection operators are −1,0, and 1. Valence band holes in GaAs can have total angular momentum eigenvalues of $J = 3/2$ or $1/2$. The large spin orbit gap in the valence band ensures the $J = 1/2$ states are far from the band edge, whereas the $J = 3/2$ states are degenerate at the k=0 point in bulk GaAs. Anisotropic confinement, such as in a lateral or nanowire quantum dot, lifts the degeneracy of the $J = 3/2$ states and separates the $J_Z = \pm 1/2$ sub-band ('light' holes) and the $J_Z = \pm 3/2$ sub-band ('heavy' holes). This separation occurs due to different microscopic p-type bloch orbitals of the holes in each

		Exchange Eigenvalues			Spin Eigenvalues	
Symbol	State	Orbital	Spin	Overall	J	J_Z
$\lvert S\rangle$	$\frac{1}{\sqrt{2}}(\lvert\Downarrow\Uparrow\rangle - \lvert\Uparrow\Downarrow\rangle)$	+1	-1	-1	0	0
$\lvert T_-\rangle$	$\lvert\Downarrow\Downarrow\rangle$	-1	+1	-1	1	-1
$\lvert T_0\rangle$	$\frac{1}{\sqrt{2}}(\lvert\Downarrow\Uparrow\rangle + \lvert\Uparrow\Downarrow\rangle)$	-1	+1	-1	1	0
$\lvert T_+\rangle$	$\lvert\Uparrow\Uparrow\rangle$	-1	+1	-1	1	+1

Table 4.2: Simultaneous eigenstates of J, J_Z, and particle exchange operators and their eigenvalues. Because holes are Fermions, the overall symmetry factor of every two-particle state must be -1. However, the spin and orbital exchange eigenvalues may differ individually.

sub-band. The heavy and light hole sub-bands are so named for the differences in the effective mass of each sub-band. If these two sub-bands are well separated, it is frequently useful to describe spin states in either sub-band in terms of a pseudo-spin with $J = 1/2$ and $J_Z = \pm 1/2$, though the properties of this pseudo-spin in each sub-band may depend on whether it is a heavy or light hole pseudo-spin. In this case, it will be verified that lateral confinement (with one dimension more tightly confined than the other two) confined a heavy hole pseudo-spin.

The four simultaneous eigenstates of total spin or pseudo-spin J and projection J_Z of a two-spin system are summarized in table 4.2. These four spin eigenstates are also eigenstates of three kinds of particle exchange. Spin exchange swaps the spins of two particles, whereas orbital exchange swaps the wavefunctions of two particles while preserving the spin. “Overall” exchange (or simply exchange) swaps both simultaneously.

Any eigenvalue λ of an exchange operator must satisfy $\lambda^2 = 1 \implies \lambda = \pm 1$, since exchange is self-inverse. Electrons and holes are also fermions, so by definition their overall exchange eigenvalue must be -1. The spin exchange eigenvalues can be calculated by applying spin exchange to the states in table 4.2 and the orbital exchange eigenvalues can be deduced without any knowledge of the orbital wavefunctions themselves [2].

Orbital exchange is relevant in the calculation of the energy spectra of the (1,1) and (2,0) states. The strength of the exchange interaction depends on the overlap of the single particle wavefunctions, which is much larger for (2,0) configurations, and thus an energy gap is expected between the spin singlet $\lvert S\rangle$ and triplets $\lvert T\rangle$ in the (2,0) configuration. This gap may vanish in the (1,1) configuration provided the wavefunction overlap between the

---

[2] Hole eigenstates are generally not eigenstates of true spin because of the spin-orbit interaction. However, within any of the individual light and heavy hole sub-bands, a pseudo-spin arises that can be discussed similarly. This discussion will apply provided the band intermixing is small

State	Energy
$E_{(1,1)S}$	0
$E_{(1,1)T_-}$	$-g^*\mu_B B$
$E_{(1,1)T_0}$	0
$E_{(1,1)T_+}$	$g^*\mu_B B$
$E_{(2,0)S}$	$\Delta\epsilon$
$E_{(2,0)T_-}$	$\Delta\epsilon + E_{ST}(B) - g^*\mu_B B$
$E_{(2,0)T_0}$	$\Delta\epsilon + E_{ST}(B)$
$E_{(2,0)T_+}$	$\Delta\epsilon + E_{ST}(B) + g^*\mu_B B$

Table 4.3: Expected energies of spin and charge eigenstates in both the (1,1) and (2,0) configurations, defined relative to the separated spin singlet.

dots is sufficiently small. For the purposes of this discussion, $E_{ST}(B)$ is taken to represent the energy gap in the (2,0) configuration between the singlet and triplet states. In principle it may be field (B) dependent, but it is non-zero at zero field.

Table 4.3 gives the energies of each of the four spin states of each of the (1,1) and (2,0) charge states of the double quantum dot in terms of the detuning ($\Delta\epsilon$), the singlet triplet gap (E_{ST}), and the applied magnetic field (B).

Transport measurements in the dilution refrigerator were used to test this theory against measured transport magnetospectra in the two hole regime. Transport triangles were observed near the (2,0)/(1,1) charge transfer line and transport spectroscopy was performed along the sweep lines indicated in figure 4.14.

In the negative bias direction, $V_D C = -2$ mV, the ground state of the (1,1) configuration ($|T_-(1,1)\rangle$) was used to probe the spectrum of the (2,0) configuration. Indeed, all four (2,0) states are visible in transport as shown in figure 4.15.

In the positive bias direction, $V = +2$ mV, the ground state of the (2,0) configuration was used to measure the spectrum of the (1,1) configuration. For $B < 1.5$ T, the ground state of (2,0) is the singlet ($|S(2,0)\rangle$) but for $B > 1.5$ T the Zeeman term overcomes the energy gap E_{ST} and the ground state is ($|T_-(1,1)\rangle$). Again, all four (2,0) states are visible in transport as shown in figure 4.15.

The effective g-factor was measured by obtaining transport spectra of the (2,0) configuration of the double quantum dot in the He3 cryostat. The (2,0) configuration was chosen because the (2,0) spin triplets are composed of two holes in the same quantum dot.

The spectrum plotted in figure 4.16 was obtained as a function of the magnetic field, here directed normal to the plane of the sample (i.e. in the z direction). Care was taken

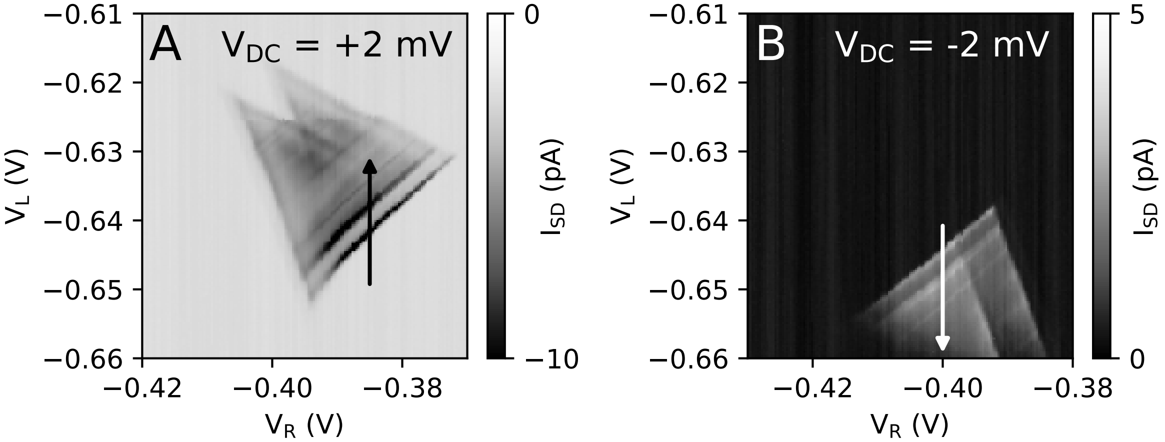

Figure 4.14: High bias transport through the (2,0)/(1,1) charge configurations of the double quantum dot in the ***A****) positive and* ***B****) negative bias directions, with multiple resonances visible in transport. A 1.0* T *magnetic field was applied in the z direction.*

to reduce the background current between resonances by reducing the tunnel coupling between dots. The energy gap between $T_-(2,0)$ and $T_+(2,0)$ yields $g^* = 1.45 \pm 0.05$ for this spectrum.

Similar spectra were obtained for various field orientations rotated by an angle θ between the z and x axes (refer to figure 3.4, which specified the spatial axes) and an effective g-factor was obtained from each one. The smallest g-factor measured with this method was 0.22, limited by the increasing overlap between the transport resonances.

The results are plotted in figure 4.17 alongside similar data reported in the literature for InAs self-assembled dots[47] and Si nanowires[48]. The effective g-factor was also fitted against the following equation:

$$g^*(\theta) = g^*_{\perp}|sin(\theta)| + g^*_{min} \tag{4.21}$$

with fitting parameters $g^*_{\perp} = 1.45$ and $g^*_{min} = -0.04$.

While the absolute anisotropy in the effective g-factor is comparable to that of the holes in InAs dots and Si nanowires, the relative anisotropy is more pronounced. Anisotropy in the effective g-factor is expected for holes under anisotropic confinement and has been

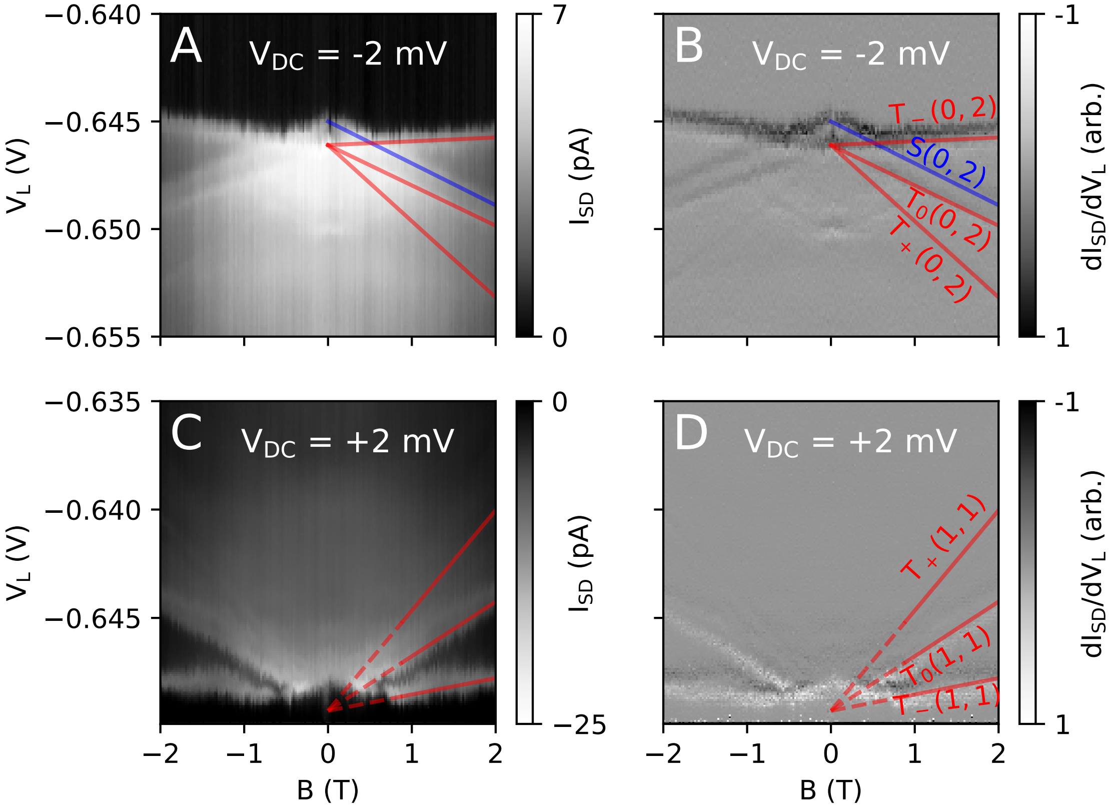

Figure 4.15: ***A****) Transport from the (1,1) to the (2,0) charge configuration showing four resonances corresponding to S(2,0) and the three T(2,0) states.* ***C****) Transport from the (2,0) to the (1,1) charge configuration showing at least three resonances, corresponding to $T-$, $T+$, and the degenerate S and T_0 states of (1,1).* ***B,D****) Numerical derivatives of the source drain currents in* ***A,C*** *with respect to detuning to enhance visibility of the resonances. Solid lines are visual guides.*

observed previously. In this case, however, the small hole g-factors observed and the prediction of the model that the g-factor vanishes when the magnetic field is directed in the plane of the sample suggests that these are heavy holes composed of the spin eigenstates $J = 3/2, J_Z = \pm 3/2$. In quantum electrodynamics, a photon cannot directly couple two states with angular momenta differing by more than one unit of $\hbar$ to first order in the interaction parameter. The heavy hole spin eigenstates differ by three units of $\hbar$. Therefore, an electromagnetic field (including a magnetic field) can only indirectly couple the heavy hole eigenstates through the light hole eigenstates via three (or more) photon processes. Because a z-directed magnetic field does not couple the heavy hole eigenstates, the z-directed component of the Zeeman interaction survives.

In a solid, a Hamiltonian describing heavy holes can contain terms that couple these heavy hole eigenstates [66] because heavy hole eigenstates do not have well defined angular momentum in the presence of a non-zero spin orbit interaction. The Luttinger parameter q describes the strength of the interaction that couples the heavy hole eigenstates directly, even in the absence of heavy hole / light hole mixing.

If the heavy and light hole subbands are decoupled, it implies a suppression of the heavy hole pseudospin effective g-factor in the xy plane of the sample, which is exactly what was observed. This is the origin of $sin(\theta)$ in equation 4.5: the effective g-factor measured was expected to be proportional to the z-directed component of the magnetic field as a fraction of the total field, since only the z-component is ‘felt’ by the hole. The observation of such pronounced g-factor anisotropy therefore suggests the holes under study are indeed heavy holes.

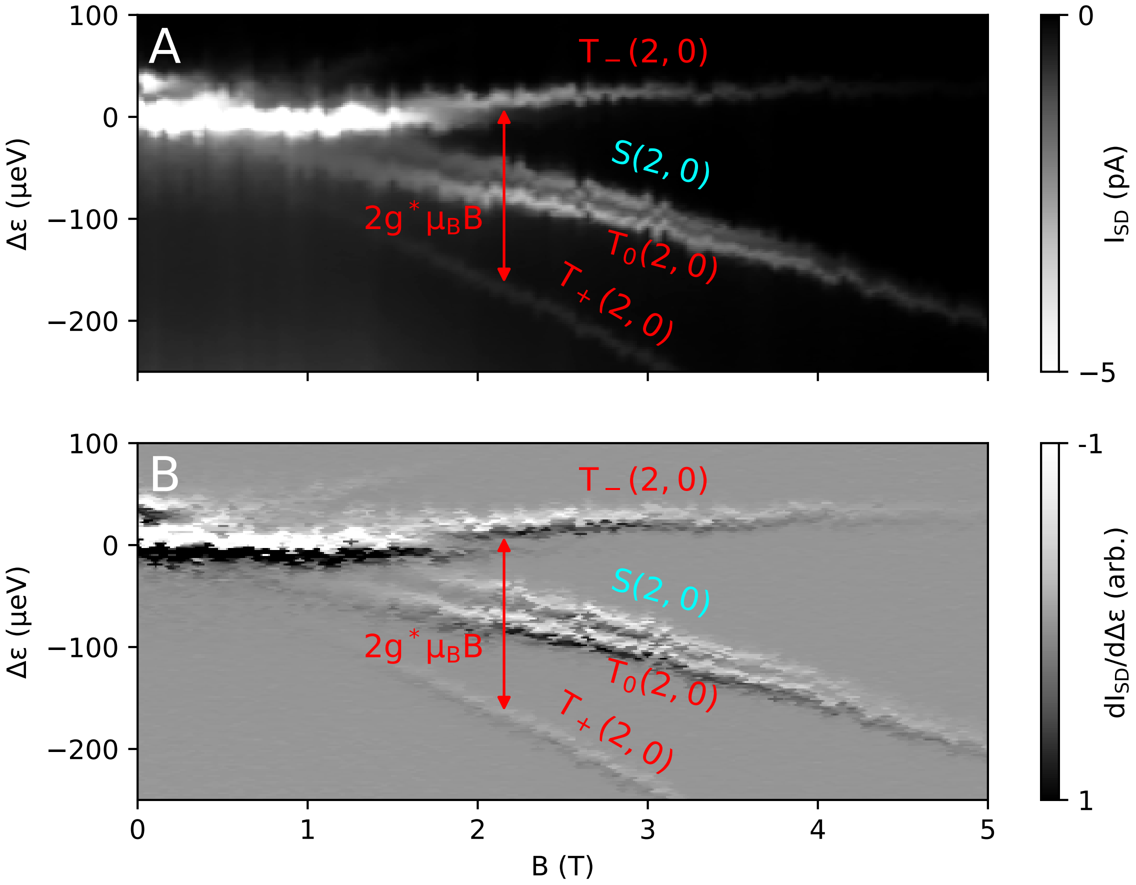

Figure 4.16: Spectrum of the (2,0) charge configuration showing the Zeeman gap between T_+ and T_- growing with field. ***A****) Raw source-drain current and* ***B****) current differentiated with respect to detuning.*

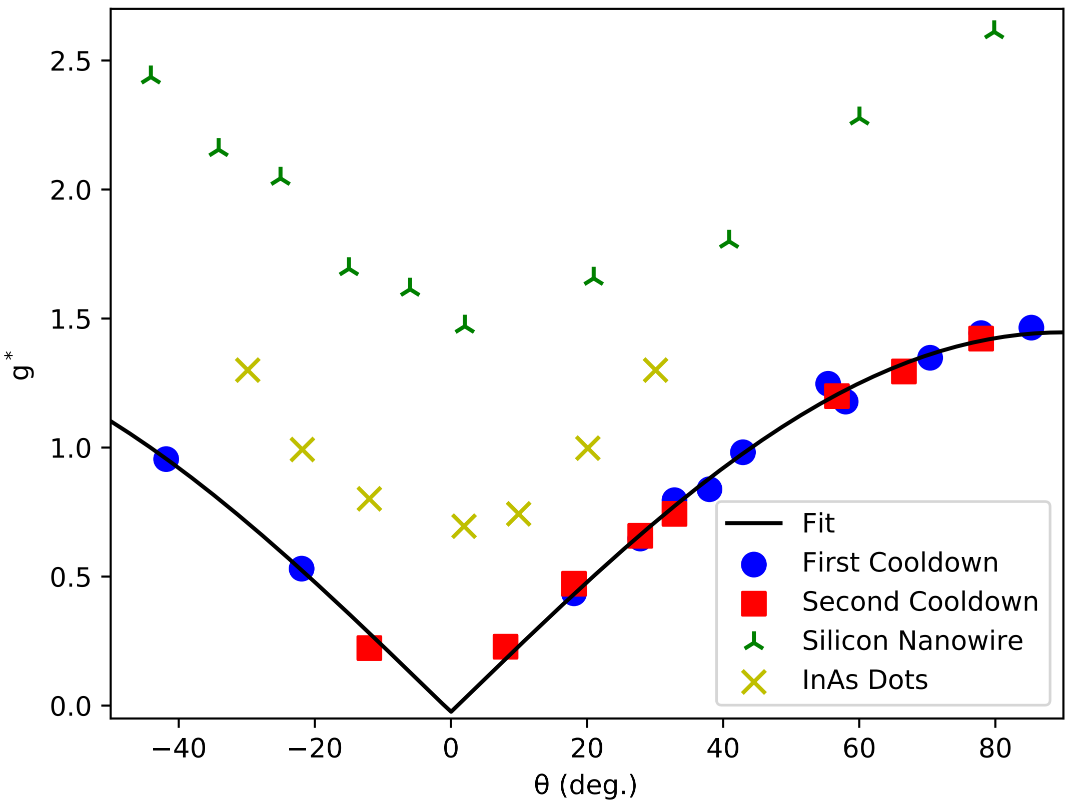

Figure 4.17: Effective g-factor (g^*) in a tilted magnetic field. θ indicates the deflection of the magnetic field from the z axis. Solid points represent experimental data obtained over two different cooldowns of the sample. Crosses indicate data series extracted from the papers referenced in the text. The fitted curve represents a best fit to equation 4.5

4.6 Spin and Spin Orbit Blockade

Previously in this chapter, Coulomb blockade (or energy blockade) was introduced. Another commonly encountered form of blockade is Pauli blockade (or spin blockade) wherein the blocking state is unable to relax due to spin conservation rules rather than energy conservation rules. For example, the two hole pseudo-spin singlet (J=0) and triplets (J=1) differ in angular momentum. Transport from left to right through intermediate states (1,1) and (2,0) in a double quantum dot may be prevented if the (1,1) triplet is populated and no state of compatible spin in (2,0) is available at a lower energy in the bias window. This prevents transport without exchange of angular momentum with the environment. This scenario is illustrated in figure 4.18 panel A in the absence of a magnetic field, where the triplet is degenerate. Panel B illustrates the scenario in the opposite bias direction, where all four populated spin states in (2,0) can tunnel into (1,1) respecting spin conservation. Spin blockade through double quantum dots has been studied in detail for electrons in GaAs.

Spin blockade can be lifted by processes that do not conserve the electron or hole spin, such as interaction with lattice phonons (mediated by spin orbit interactions) and the spins of the Gallium and Arsenic nuclei in the lattice. For electrons in GaAs, the hyperfine contribution lifts the spin blockade in the absence of an applied field [67]. The Hyperfine contribution to the Hamiltonian is:

$$H_{HYP} = \sum_i A_i \vec{I_i} \cdot \vec{S} \tag{4.22}$$

Here, i indexes the individual nuclei, I_i is the spin of that nucleus, S is the spin of the carrier, and A_i quantifies the strength of the interaction between the carrier and the particular nucleus. In cases where many nuclei are relevant, such as in quantum dots that span many thousands of nuclei, the hyperfine interaction can be treated semi-classically by replacing the hyperfine field with its expectation value, sometimes expressed as an effective magnetic field.

The often spatially inhomogeneous and generally time dependent nuclear hyperfine field can couple spin states of different total spin or spin projection and therefore lift spin blockade. When the Zeeman field $E_Z = g^* \mu_B B$ is much larger than the hyperfine field, however, it stabilizes the spin and prevents mixing (in particular) of states of different total spin. In GaAs, externally applied magnetic fields in excess of tens to hundreds of mT can suppress spin flips due to the hyperfine field in this way, enabling spin blockade to occur.

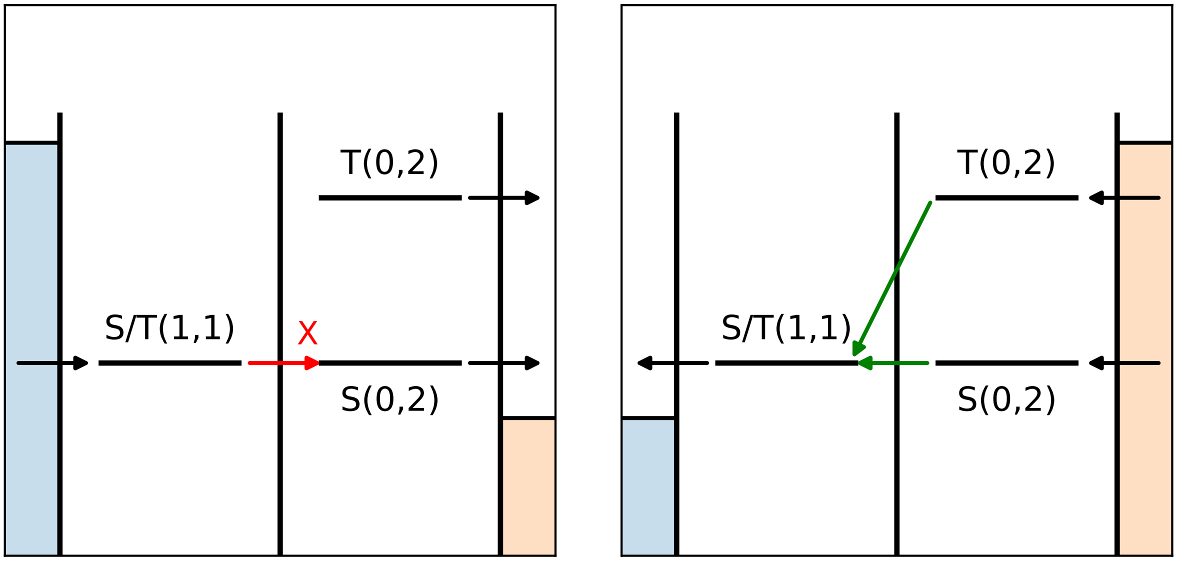

Figure 4.18: Schematic illustrating an example of spin blockade. ***A****) Transport is blockaded in the forward bias direction because the spin triplet states (T(1,1)) can be populated from the source, but cannot relax into S(2,0) or S(1,1) without violating spin conservation rules.* ***B****) Transport is not blockaded in the reverse bias direction because all four spin states of (2,0) can tunnel into (1,1) respecting spin conservation.*

Experiments have shown that holes in GaAs quantum dots can experience weaker hyperfine coupling (A_i) compared to electrons [68].

Spin blockade has been reported for holes in GaAs quantum dots [44]. However, spin orbit interactions for holes in GaAs are stronger by several orders of magnitude than for electrons, which can suppress angular momentum conservation in inter-dot tunneling [69]. The spin orbit interactions have been shown in the previously described experiments to allow inelastic inter-dot spin flip tunneling at similar rates to the spin-conserving tunneling (see table 4.1). Because inelastic inter-dot transport does not necessarily conserve spin as it does for electrons, conventional spin blockade in a magnetic field was *not* observed in this device. However, an unconventional form of blockade *was* observed in small fields.

In the dilution refrigerator unit, using the transport measurement circuit, a transport spectrum was obtained for the small field range $B \in [-125, 125]$ mT using a bias of $V_{DC} = -2$ mV. Dips were observed in the current along the S(2,0) resonance and the nearly degenerate T(2,0) resonances, as shown in figure 4.19. Over this range of fields the source states (the four spin states of the (1,1) charge configuration) are nearly degenerate, since $E_Z < 10$ µeV.

Also shown in figure 4.19 panel B is the single spectral line observed in the opposite bias direction: $V_{DC} = +2$ mV over the range $B \in [-60, 60]$ mT. No corresponding dip was observed in this spectral line over that range of magnetic fields.

To understand these dips, the doubly occupied DQD system was modelled by the following Hamiltonian [64] expressed in the $S(2,0)$, $T_-(2,0)$, $T_0(2,0)$, $T_+(2,0)$, $T_-(1,1)$, $S(1,1)$, $T_0(1,1)$, $T_+(1,1)$ basis:

$$\hat{H} = \begin{bmatrix} E_{S(2,0)} & 0 & 0 & 0 & it_{ST}^{(F)} & -\sqrt{2}t_{ST}^{(N)} & 0 & -it_{ST}^{(F)} \\ 0 & E_{T-(2,0)} & 0 & 0 & -t_{TT}^{(N)} & \frac{i}{\sqrt{2}}t_{TT}^{(F)} & -\frac{i}{\sqrt{2}}t_{TT}^{(F)} & 0 \\ 0 & 0 & E_{T0(2,0)} & 0 & -\frac{i}{\sqrt{2}}t_{TT}^{(F)} & 0 & -t_{TT}^{(N)} & \frac{i}{\sqrt{2}}t_{TT}^{(F)} \\ 0 & 0 & 0 & E_{T+(2,0)} & 0 & -\frac{i}{\sqrt{2}}t_{TT}^{(F)} & -\frac{i}{\sqrt{2}}t_{TT}^{(F)} & t_{TT}^{(N)} \\ -it_{ST}^{(F)} & -t_{TT}^{(N)} & \frac{i}{\sqrt{2}}t_{TT}^{(F)} & 0 & E_{T-(1,1)} & 0 & 0 & 0 \\ -\sqrt{2}t_{ST}^{(N)} & -\frac{i}{\sqrt{2}}t_{TT}^{(F)} & 0 & \frac{i}{\sqrt{2}}t_{TT}^{(F)} & 0 & E_{S(1,1)} & 0 & 0 \\ 0 & \frac{i}{\sqrt{2}}t_{TT}^{(F)} & -t_{TT}^{(N)} & \frac{i}{\sqrt{2}}t_{TT}^{(F)} & 0 & 0 & E_{T0(1,1)} & 0 \\ it_{ST}^{(F)} & 0 & -\frac{i}{\sqrt{2}}t_{TT}^{(F)} & t_{TT}^{(N)} & 0 & 0 & 0 & E_{T+(1,1)} \end{bmatrix} \tag{4.23}$$

The tunneling matrix elements, parameterized by $t_{ST}^{(F)}$, $t_{TT}^{(F)}$, $t_{ST}^{(N)}$, and $t_{TT}^{(N)}$, represent inter-dot tunneling. Here, the value of the tunnel coupling is assumed to vary depending on the total spin of the source and destination states (S vs. T) as well as the change in total spin projection and whether there is a spin flip (F) involved or not (N).

At the $\Delta\epsilon = 0$ resonance, $E_{S(2,0)} = E_{S(1,1)} = E_{T-(1,1)} = E_{T0(1,1)} = E_{T+(1,1)}$. At the $\Delta\epsilon = E_{ST}$ resonance, $E_{T_-(2,0)} = E_{T_0(2,0)} = E_{T_+(2,0)} = E_{S(1,1)} = E_{T-(1,1)} = E_{T0(1,1)} = E_{T+(1,1)}$.

In the negative bias direction, where the inter-dot tunneling is from (1,1) to (2,0), the observed dips in the current at each resonance near $B = 0$ can be understood in terms of meta-stability of the (1,1) charge state. At $\Delta\epsilon = 0$ and $B = 0$, the Hamiltonian in the reduced $S(2,0)$, $T_-(1,1)$, $S(1,1)$, $T_0(1,1)$, $T_+(1,1)$ basis (those states that are involved in transport) is:

$$H_S = \begin{bmatrix} \Delta\epsilon & -\sqrt{2}t_{ST}^{(N)} & it_{ST}^{(F)} & 0 & -it_{ST}^{(F)} \\ -\sqrt{2}t_{ST}^{(N)} & 0 & 0 & 0 & 0 \\ -it_{ST}^{(F)} & 0 & -E_Z & 0 & 0 \\ 0 & 0 & 0 & 0 & 0 \\ it_{ST}^{(F)} & 0 & 0 & 0 & E_Z \end{bmatrix} \tag{4.24}$$

This Hamiltonian has three degenerate eigenstates with zero energy composed exclusively of (1,1) states. There are two non-degenerate eigenstates that are mixtures of $S(2,0)$ and $(1,1)$ states: the ground state and the most excited state.

At zero detuning and zero field, the non-degenerate eigenstates that include a component of $S(2,0)$ are:

$$|-\rangle = -\frac{i}{\sqrt{2}}\,|S(2,0)\rangle + \tilde{t_F}\,|T_-(1,1)\rangle + \tilde{t_F}\,|T_+(1,1)\rangle - \frac{i}{\sqrt{2}}\tilde{t_N}\,|S(1,1)\rangle \tag{4.25}$$

$$|+\rangle = -\frac{i}{\sqrt{2}}\,|S(2,0)\rangle + \tilde{t_F}\,|T_-(1,1)\rangle + \tilde{t_F}\,|T_+(1,1)\rangle + \frac{i}{\sqrt{2}}\tilde{t_N}\,|S(1,1)\rangle \tag{4.26}$$

$$\tilde{t_F} = \frac{t_{ST}^{(F)}}{\sqrt{t_{ST}^{(F)2} + t_{ST}^{(N)2}}} \tag{4.27}$$

$$\tilde{t_N} = \frac{t_{ST}^{(N)}}{\sqrt{t_{ST}^{(F)2} + t_{ST}^{(N)2}}} \tag{4.28}$$

with energies:

Matrix Element	Value (µeV)
$t_{ST}^{(F)}$	0.41
$t_{ST}^{(N)}$	0.51
$t_{TT}^{(F)}$	0.38
$t_{TT}^{(N)}$	0.41

Table 4.4: Tunneling matrix elements used as parameters to model the data in 4.19.

$$E_- = -\sqrt{2(t_{ST}^{(F)2} + t_{ST}^{(N)2})} \tag{4.29}$$

$$E_+ = +\sqrt{2(t_{ST}^{(F)2} + t_{ST}^{(N)2})} \tag{4.30}$$

The energies of the $|+\rangle$ and $|-\rangle$ states can be in terms of an effective magnetic field:

$$B_{SO} = 2\sqrt{2}\frac{\sqrt{(t_{ST}^{(F)2} + t_{ST}^{(N)2})}}{g^*\mu_B} \tag{4.31}$$

$$E_- = -\tfrac{1}{2}g^*\mu_B B_{SO} \tag{4.32}$$

$$E_+ = +\tfrac{1}{2}g^*\mu_B B_{SO} \tag{4.33}$$

When $B << B_{SO}$, there are three degenerate blocking spin states in the (1,1) charge configuration that cannot coherently tunnel into (2,0). As B becomes finite compared to B_{SO}, two of these states become non-blocking and acquire some component of $S(2,0)$. This causes an increase in the current on the $\Delta\epsilon = 0$ resonance.

This is observed as a dip in the current at resonance as a function of the magnetic field applied in the z direction. A more complete analysis of this current dip, including an analysis of the $\Delta\epsilon = E_{ST}$ resonance and inelastic processes, is in preparation [70]. From that analysis, a numerical model of the resonant currents at both resonances vs B in figure 4.19 gives an estimate of the tunneling matrix elements. These estimated tunneling matrix elements are summarized in table 4.4.

No supression is expected or observed in the resonant transport in the reverse bias direction because there are no blocking states of (2,0) at zero field. Specifically, there are no eigenstates of the system that contain only (2,0) charge states at zero detuning.

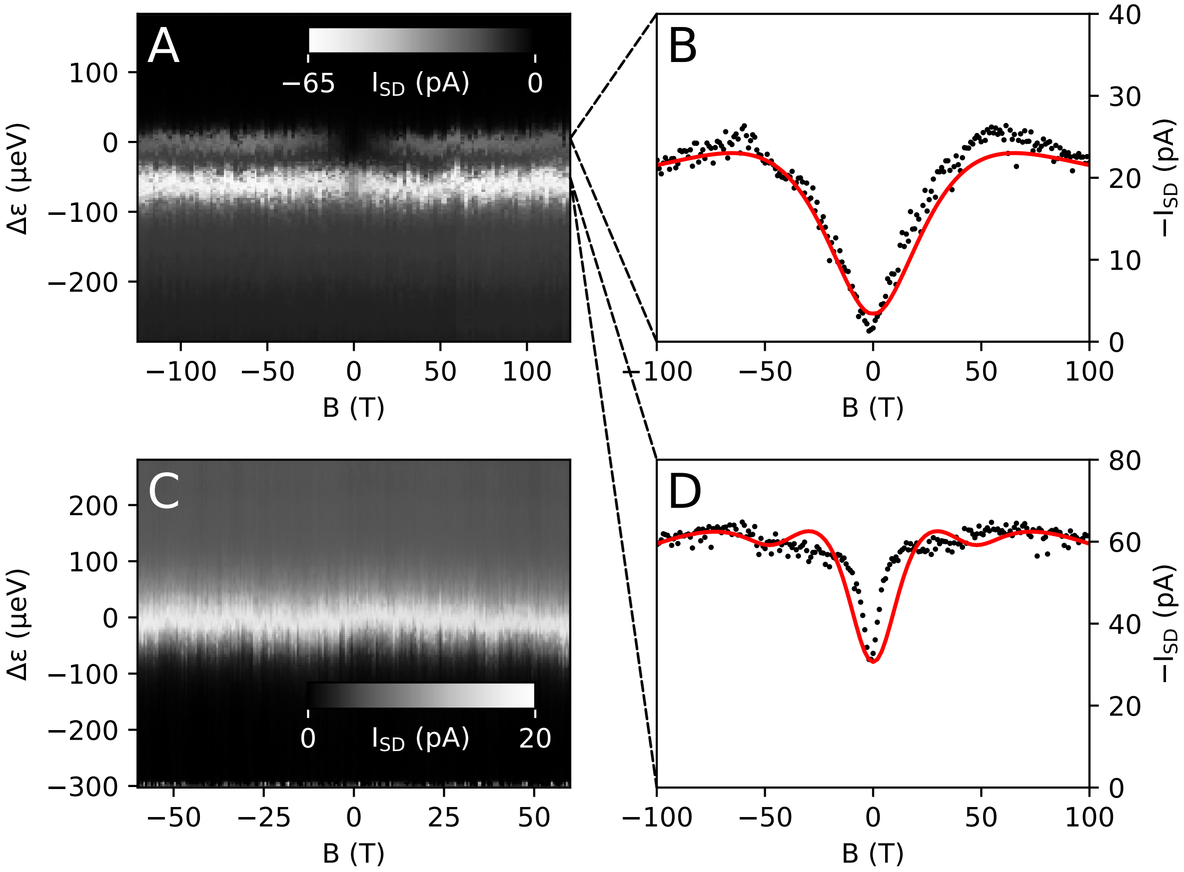

*Figure 4.19: Source drain current as a function of detuning and applied magnetic field in the forward (**A**) and reverse (**C**) directions. Single line traces extracted at constant detuning along the two visible resonances are shown in **B** and **D** showing current suppression at zero field, fitted to the numerical model discussed in the text.*

4.7 Conclusions

The transport spectroscopy experiments in this chapter were used to directly probe the energy spectra of the singly and doubly-occupied double quantum dot, and specifically the (1,0),(0,1),(2,0), and (1,1) charge states [3]. Numerical simulation of the transport current revealed that these measurements encode coherence information about the tunneling, including relaxation times. Most notably, the single-spin dephasing time (at B=0.5 T) was estimated from these measurements to be 0.75 µs in this transport regime. The energy spectrum of the singly occupied dot was used to extract the single hole g-factor, found to be $g^* = 1.35$ along the z direction (parallel to the growth axis). The spectrum of the (2,0) configuration was used to study the anisotropy of the effective hole g-factor, which was found to vary dramatically with the angle of the applied field with a maximum of $g^* = 1.45$. While zero effective g-factor could not be observed due to the finite width of the spectral lines, the smallest directly observed value was $g^* = 0.2$ and a fit to a sinusoidal model was consistent with zero minum g-factor. This suggests that the holes confined in this system were heavy holes with minimal light/heavy hole mixing.

---

[3] Similar results were obtained for the (0,2) state and were not shown

Chapter 5

Single Hole Spin Relaxation

Coherence is of particular interest in the study of spin qubits. The characterization of decoherence is especially important for applications, where longer coherence times are needed. Moreover, since both spin relaxation and intrinsic phase decoherence are fundamentally the product of interactions with the environment of the spin qubit, studying the details of both can give a better understanding of environmental sources of noise and decoherence.

The parameters that quantify the most common decoherence mechanisms for qubits are the spin relaxation time T_1 and the spin decoherence times T_2 and T_2^*. T_1 defines the mean relaxation lifetime of the excited qubit state. T_2 defines the mean dephasing time, including only the intrinsic or "bare" (free induction decay) component of the dephasing due to quantum entanglement between the qubit and the environment. T_2^* is a similar quantity, but also includes dephasing due to (semi-) classical interactions between the qubit and a noisy or uncertain environment.

In this chapter, the focus will be placed on spin relaxation (T_1). Because spin relaxation into an energy eigenstate necessarily erases phase information as well, T_1 establishes an upper bound on the values of T_2 and T_2^*. A measurement of T_1 is therefore an appropriate first step in assessing the coherence of single hole spin qubits.

T_1^{-1} measures the rate at which the excited component of the spin (denoted $|\Uparrow\rangle$ here) relaxes into the ground state ($|\Downarrow\rangle$ here). By the linearity of quantum mechanical processes, a single rate describes relaxation from any linear superposition of $|\Uparrow\rangle$ and $|\Downarrow\rangle$ to the ground state. Under T_1-like spin relaxation for a time T_R, the time-dependence of the spin superposition is captured by:

$$P_{\Uparrow}(t = T_R) = \exp(-T_R/T_1)P_{\Uparrow}(t = 0) \tag{5.1}$$

Measuring T_1 is important to evaluate hole spin qubits as candidate qubits for quantum information processing. It has been claimed that holes interact more weakly with the nuclei of the crystal lattice [71, 72], which is a dominant cause of spin relaxation for electron spin qubits. It is important to study spin relaxation to experimentally establish the effect of hyperfine interactions with the lattice nuclei.

In electron spin qubits, two mechanisms contribute to spin relaxation [30, 73]. Which effect is dominant depends on the strength of the applied magnetic field. For small fields, hyperfine interactions between the lattice nuclear spin bath and the spin qubit dominate spin relaxation. When the external magnetic field is smaller than the effective hyperfine field, the qubit can efficiently exchange angular momentum with the nuclear spins in the lattice. Because the Bloch functions of holes in GaAs have reduced overlap with the nuclei, contact interactions (including contact hyperfine interactions) have been predicted [71, 74–76] and measured [77–79] to be suppressed in hole systems.

When a magnetic field is applied and the Zeeman field exceeds the effective hyperfine field, hyperfine induced spin flips are suppressed. In this regime the dominant contribution to ${T_1}^{-1}$ is phonon mediated spin-orbit interaction with the lattice. Phonons couple lattice charge motion with the motion of the charge distribution and spin orbit interactions couple the charge distribution to the spin. These interactions become more significant at larger magnetic fields, as the Zeeman energy separating the two qubit terms becomes larger and the phonon density of states increases with energy. Theoretically [80, 81] and experimentally [30, 80–86], the electron spin T_1 in GaAs has been found to depend on the magnetic field as $T_1 \propto B^{-5}$ in this regime.

For hole spins, a $T_1 \propto B^{-5}$ term is contributed by the Dresselhaus spin orbit interaction and $T_1 \propto B^{-9}$ originates in Rashba spin-orbit[37, 52].

The focus of this section is an experimental study of the T_1 spin-relaxation time in a single heavy hole spin qubit in a lateral GaAs quantum dot. To measure T_1 as a function of the applied magnetic field, a novel technique will be presented that accomplishes high speed single shot projection of the single spin qubit without the use of a high-speed charge detector such as an RF-QPC.

Charge-latch techniques have been used in the study of spin qubits for some time, in conjunction with Pauli blockade in electron systems [87–90]. However, Pauli blockade techniques do not apply naturally to holes due to the large spin non-conserving tunneling interaction [65, 69] described in section 4.4. Spin-selective tunneling to a lead [82, 84, 85, 91] could in principle be used for single shot spin detection, but these methods require fast, sensitive electronics for high-fidelity measurement. Instead, spin-selecting spin non-conserving tunneling was utilized to enable fast projection of a single spin onto the state of a charge latching. This was accomplished using tunneling effects that couple states of dissimilar spin between dots, discussed in section 4.4. The resulting charge states could be interrogated by the relatively insensitive charge sensor to extract the information encoded in the charge latch, demonstrating that high-speed charge detection is not necessary for high-speed projection of hole spin qubits. This projection and readout technique is the subject of the next section.

5.1 Single Hole Spin Projection and Readout in a Double Quantum Dot

The spin projection procedure described in this section makes use of the unique properties of holes studied in previous sections to rapidly project a single hole spin in a quantum dot onto the charge state of a second quantum dot. The secondary quantum dot, tunnel coupled to the primary dot, is used to perform spin to charge conversion and as a charge-based memory latch to encode and store the result of the spin measurement. The charge latching capability is provided by an asymmetric tuning of the tunnel barriers. The spin to charge conversion capability is provided by the strong resonant spin non-conserving inter-dot tunneling explored in section 4.4.

In the reference experiment developed for this device, the primary dot was the left dot and the secondary dot was the right dot. The reference experiment included state preparation for the spin qubit in the left dot, projection of the prepared spin state using spin to charge conversion, and finally latched charge readout of the right dot.

The relative tuning of the tunnel barriers in the DQD was critical. In order to ensure the right dot could be used as a charge latch, it was isolated from the right lead to prevent direct tunneling between the (0,0) and (0,1) charge configurations. The rightmost tunnel barrier was therefore effectively pinched off, such that the tunneling rate from the right dot to the right lead was ~2 Hz as measured by the mean lifetime of the (0,1) state relaxing in the (0,0) charge stability region. The off-resonant inter-dot inelastic tunneling rate was tuned to approximately 500 kHz, while the on-resonance inter-dot tunneling matrix elements were tuned to approximately 0.2 µeV each (spin-flipping and non-flipping) giving a resonant tunneling rate of approximately 50 MHz. Finally, the tunneling rate from the left dot to the left lead (1,0) to (0,0)) was approximately 100 MHz: two orders of magnitude faster than the inelastic interdot tunneling rate, ensuring that this rate was dominant. This ensured that if the (1,0) state was able to decay into either the (0,0) or (0,1) states, the (0,0) decay pathway was more likely. Each of these quantities were calibrated at B=1 T.

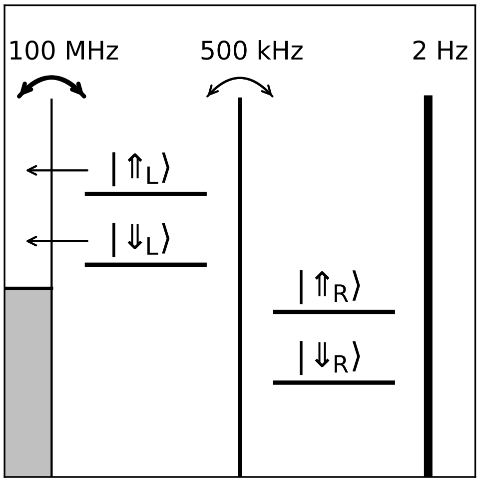

Figure 5.1: Sketch showing asymmetric tunnel barriers and single-hole states in the DQD. The left barrier is effectively more transparent than the inter-dot barrier, such that if the right dot ('R') is empty then the left dot ('L') can be emptied reliably by raising it above the Fermi level in the left lead. In the positive detuning condition shown, the (0,0) and (0,1) or 'R' charge states are meta-stable and the (1,0) or 'L' states tend to decay into (0,0) by ejection of a hole to the lead. This preserves the charge state of the right dot. The inelastic tunneling rates associated with each barrier are indicated above their respective barriers.

Figure 5.1 shows the effects of the asymmetric tunnel barriers.

These asymmetric tunnel barriers provided charge latching capability simply by visiting positive detuning, where the right dot is effectively decoupled from the leads.

The spin information was encoded into the charge state of the right dot prior to latching by attempting to allow the hole to tunnel into the right dot on the spin-flip resonance depicted in figure 5.2 panel A. On this resonance, only the state $|\Uparrow_L\rangle$ can tunnel to the state $|\Downarrow_R\rangle$ to change the charge state of the device. Thus, if this resonance is engaged for a time and the right dot is later latched and found occupied, it implies the initial spin state was $|\Uparrow_L\rangle$. This is the resonant spin to charge conversion enabled by spin non-conserving tunneling.

These two components of the protocol, specifically charge latching and resonant spin to charge conversion, were combined with spin initialization steps to form the 5 step pulse

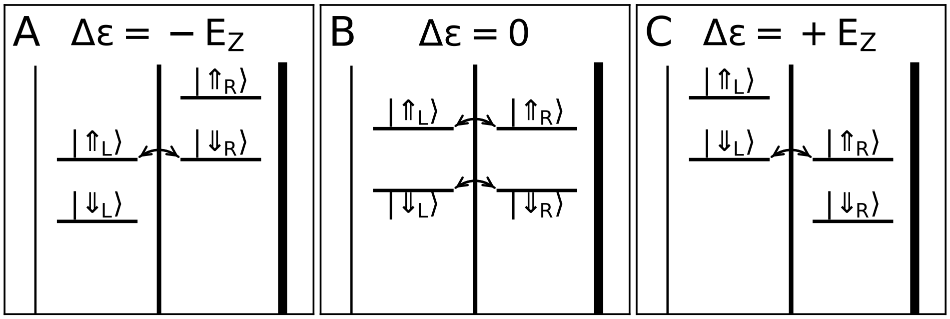

Figure 5.2: Energy diagram showing three important inter-dot resonances. ***A****) When* $\Delta\epsilon = -E_Z$*, tunneling matrix element* t_F *resonantly couples* $\Uparrow_L$ *and* $\Downarrow_R$*.* ***B****) When* $\Delta\epsilon = 0$*, tunneling matrix element* t_N *resonantly couples the L and R charge states without a spin flip.* ***C****) When* $\Delta\epsilon = +E_Z$*, tunneling matrix element* t_F *resonantly couples* $\Downarrow_L$ *and* $\Uparrow_R$*.*

sequence shown in figure 5.3. The first two voltage steps empty the DQD to clear the latch and ensure successive experiments are independently initialized with new spins. The third step admits a hole with random spin from the lead. The fourth step performs spin to charge conversion. The fifth step latches the chage state that now encodes the spin information.

The steps, in greater detail, are as follows. Consult figure 5.3, which identifies the points of interest: ‘M’, ‘R’, and ‘T’ in the charge stability diagram.

1. In the (1,0) region at point ‘R’ in figure 5.3, the right dot was emptied into the left dot to reset the memory latch.
2. In the (0,0) region at point ‘M’, the hole was ejected from the left dot leaving the DQD empty in (0,0).
3. Once more visiting point ‘R’, a hole was admitted from the lead with random spin and it was allowed to relax for a time T_R.
4. At point ‘T’ near the charge transfer line, the excited spin state in the left dot was allowed to resonantly hybridize with the dissimilar spin state of the right dot. An ‘up’ hole was allowed to freely tunnel between the dots while a ‘down’ hole was not.
5. Visiting point ‘M’ for an extended period latched the charge state readout by the nearby charge detector.

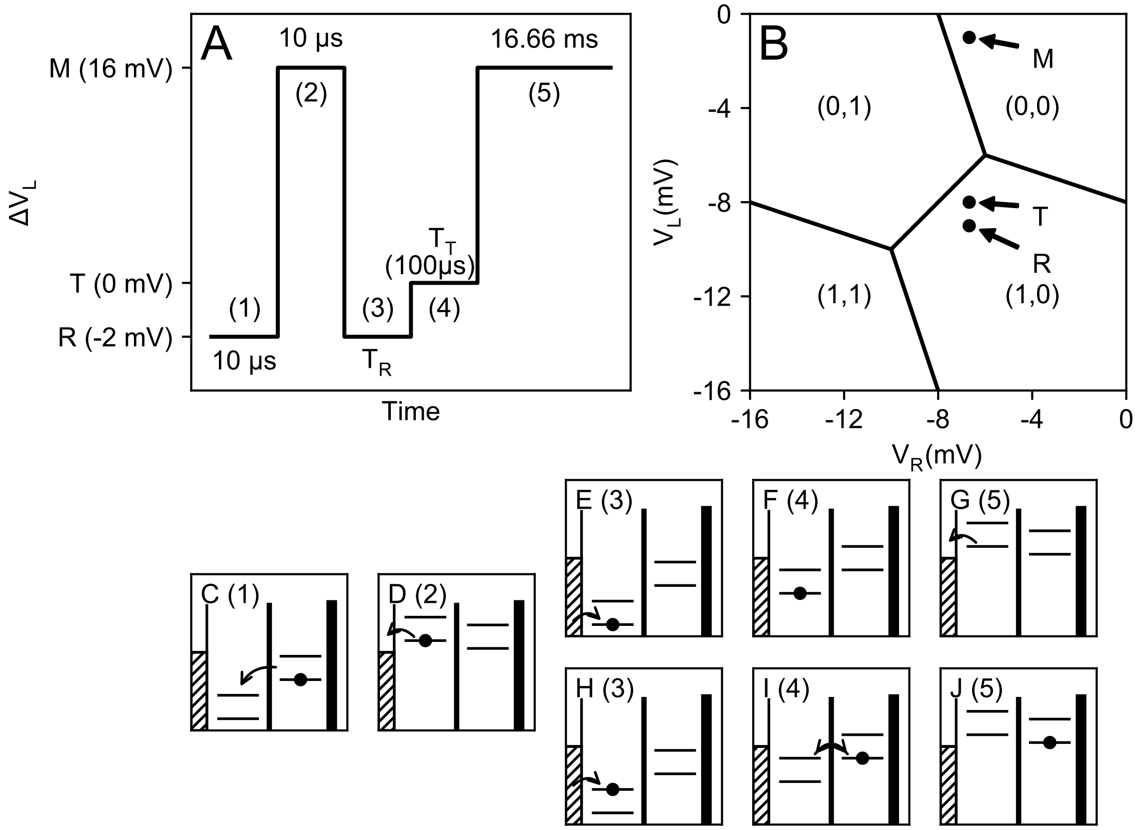

*Figure 5.3: **A**) Five step voltage pulse sequence applied cyclically to gate 'L' on the AC input of the gating circuit. Time axis not to scale. Levels and timing are indicated. The default value of* T_T *is* 100 ns *unless otherwise indicated. **B**) Sketch of the charge stability diagram showing which regions were visited in execution of the protocol. The indicated points 'M', 'T', and 'R' correspond to 'Measurement', 'Transfer', and 'Relaxation' respectively as well as to the levels in panel A. **C**) At point 'R' a hole is collected in the left dot, possibly from the right dot, and ejected. **D**) The (0,0) charge state is prepared by ejecting the hole at point 'M'. **E,H**) At 'R' a hole with random spin is allowed to tunnel into the left dot. Either **E**) a down spin is randomly admitted or **H**) an up spin is admitted. **F,I**) At the* $\Delta\epsilon = -E_Z$ *resonance, point 'T', resonant tunneling permits only an up spin to tunnel to the right. **G,J**) If the hole is in the left dot, it is ejected. In either case, the charge state is then rendered meta-stable by remaining at positive detuning.*

The timings and relative detunings of each step in the reference experiment are summarized in table 5.1.

Step	Point	Detuning (meV)	Duration
1	R	-0.882	10 µs
2	M	0	10 µs
3	R	-0.882	T_R (100 ns to 100 µs)
4	T	-0.784	100 ns
5	M	0	16 ms

Table 5.1: The five steps of the voltage pulse sequence and the duration and detuning at each step used in the experiment.

With a 1 mV bias applied to the QPC[1], the current through the QPC (I_{QPC}) was averaged over a single cycle and recorded. Because of the exceptionally long storage times enabled by the charge latching technique, which further enabled long integration times on the order of several miliseconds, the fidelity of the charge detection was not a limiting factor in evaluating the success of the protocol.

The fidelity of the spin to charge conversion in step 4 will be analyzed in appendix B. However, irrespective of the fidelity of the spin to charge conversion, the charge state of the DQD manifests itself as a distinct level of current in the QPC charge sensor. If the statistical charge outcome after the transfer step is sensitive to the spin input after relaxation, then equation 5.1 predicts exponential decay of the average QPC current with increasing T_R according to:

$$I_{QPC}(t = T_R) = I_{QPC}(t = 0)e^{-T_R/T_1} + I_{QPC}(t \to \infty)(1 - e^{-T_R/T_1}) \tag{5.2}$$

where the initial and final values of I_{QPC} depend on the fidelity and visibility of the spin to charge conversion, as well as the charge sensitivity of the QPC, but the parameter T_1 does not.

The protocol presented above depends sensitively on the position of the point ‘T’, where spin-selective charge transfer projects the spin state onto the charge configuration of the DQD in step 4. The protocol was performed as a function of the average detuning ($\Delta\epsilon$)

---

[1] At this bias the QPC energy dissipation varies between 2 and 20 pW depending on the resistance of the QPC, which could contribute to spin relaxation by (for example) populating the phonon bath. The results presented in this chapter have been replicated under conditions of reduced QPC bias to verify that the QPC itself is not a source of relevant phonons or thermal excitation, but these results have not yet been published.

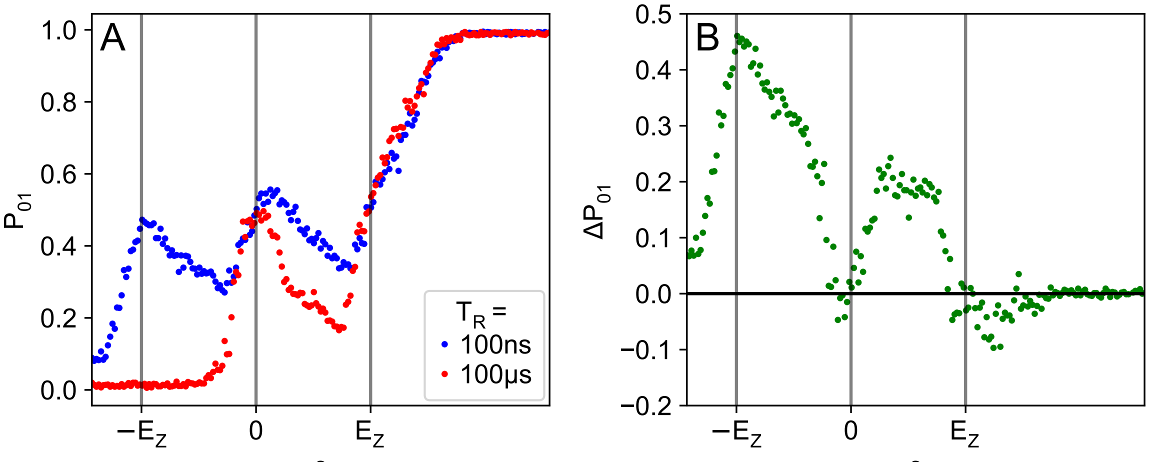

Figure 5.4: ***A****) Probability of finding the DQD in the state (0,1), obtained by sampling 1000 measurements, as function of the detuning* $\Delta\epsilon$ *for two values of relaxation time TR: 100 ns (blue) and 100* μs *(red) at* $B = 1$ *T. B) Difference between the blue and red traces in panel A.*

and the relaxation time (T_R) to determine the optimal setting for spin to charge conversion. For each setting, the probability of a (0,1) charge outcome (P_{01}) was calculated from 1000 measurement outcomes. Panel A of figure 5.4 shows the results for two extreme different values of T_R differing by three orders of magnitude. The probability of tunneling into (0,1) dramatically differed for $T_R = 100\,\text{ns}$ and $T_R = 100\,\mu\text{s}$ when $\epsilon \approx -E_Z$ or $E_Z > \epsilon > 0$. The contrast in the outcome probability depends on $\Delta\epsilon$, and panel B shows that the maximum contrast occurs near $\Delta\epsilon = -E_Z$. Variation of T_R was expected to impact the spin superposition during step 4 according to equation 5.1. The variation in the charge state outcome with decay of the measured spin at $\Delta\epsilon = -E_Z$ is evidence of the spin sensitivity of the protocol.

To confirm that the QPC current depends on the relaxation time in step 3 as expected, the detuning was fixed at the maximum of apparent sensitivity of the charge state outcome to the spin state input: $\Delta\epsilon = -E_Z$.

The duration of the relaxation step was varied logarithmically from $T_R = 100\,\text{ns}$ to $100\,\mu\text{s}$ over 500 steps and at each value the average QPC current was measured. Each of these single-shot QPC measurements implied one of two charge outcomes (0,0) or (0,1) using a simple current threshold technique, whereby the current threshold dividing the (0,0) outcomes and the (0,1) outcomes was simply the average of the 10 largest and 10 smallest recorded current values in the data set. An example of this raw data and the thresholding technique is shown in panel A of figure 5.5. For the purposes of extracting T_1, raw QPC current values were averaged using a Gaussian kernel. This procedure yielded data sets such as panel B of figure 5.5. The averaged QPC current was then fit to equation 5.2, yielding T_1.

This procedure was repeated to extract T_1 over multiple values of B from B =0.5 T to 1.5 T. The results are plotted in panel C of figure 5.5. A good fit is obtained over this range of B to $T_1 = 2.5\,\mu\mathrm{s}B^{-5}$.

As mentioned previously, the observed B^{-5} dependence of T_1 on the applied field is a hallmark of the phonon mediated Dresselhaus spin-orbit relaxation in the case of heavy holes. Dresselhaus spin-orbit interactions are notably much weaker for electrons in GaAs, and indeed the values of T_1 obtained in this sample are four orders of magnitude shorter than typical values obtained for electron spin qubits in similar GaAs quantum dots [92–95]. Over this range of magnetic fields, the spin relaxation is an order of magnitude faster than hole spin relaxation observed in Silicon quantum dots [41, 43, 96]. This is expected owing to the suppressed Dresselhaus spin-orbit interaction in the centro-symmetric Silicon lattice. However, the measured relaxation time compares favourably to other reports of spin relaxation in hole systems in GaAs, for example $T_1 = 53.7$ µs at $B = 0.5$ T compared to $T_1 = 312$ ns under the same conditions in [44]. In that paper, the qubit under study was not confirmed to be a pure heavy hole and indeed the degree of g-factor anisotropy observed in section 4.4 was not observed in that case, suggesting that the more pronounced heavy hole character of this qubit may be protective.

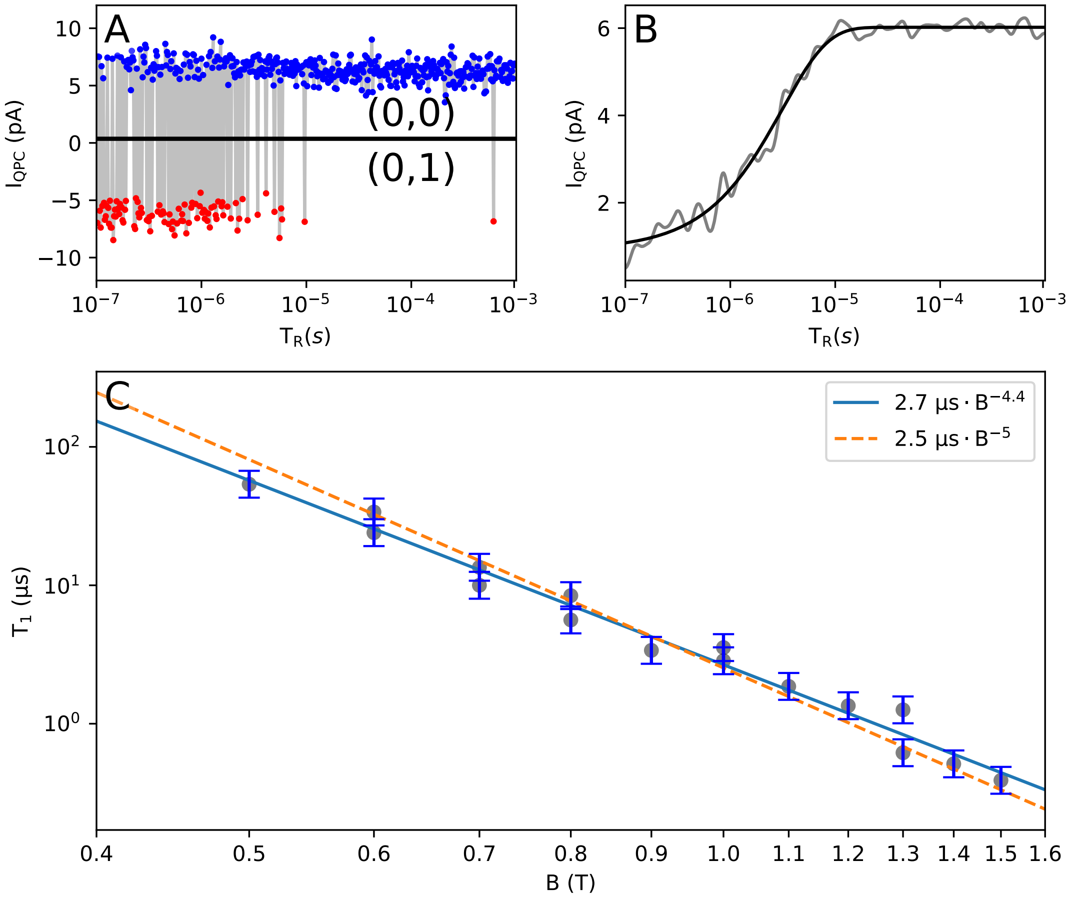

Figure 5.5: ***A****) Single-shot measurements of average QPC current as a function of* T_R *at B* $= 1.0\,\mathrm{T}$ *and* $\epsilon = -E_Z$*. The horizontal line is used as the current threshold for discriminating between (0,0) and (0,1) charge outcomes.* ***B****) Average* I_{QPC} *obtained by Gaussian averaging of 10 traces. The curve is a fit to equation 5.1 giving* $T_1 = 3.1\,\mu\mathrm{s}$*.* ***C****) Gray circles represent measurements of* T_1 *obtained using data similar to the above for different values of B. The lines correspond to fits to power laws of the form* $T_1 = AB^n$*, either with the power n as a free fitting parameter (solid green) or fixed to* $n = -5$ *(dashed red).*

5.2 Conclusions

As with all control fields, the spin-orbit interaction is a path for decoherence and noise to act on the qubit as well. Efforts to mitigate the relaxation of hole spins in GaAs quantum dots system might focus on minimizing coupling to phonons by engineering of the phonon density of states [97] or by optimization of the shape and orientation of the dot, as for example in [98], where circular symmetry was shown to slow spin relaxation.

Two advantages of this protocol can be stated compared to conventional single spin readout techniques that use a reference lead in lieu of a charge latch [84]. This technique separates the spin to charge conversion step from the charge readout step, separating them in time. The spin to charge conversion step is limited in speed only by the tunable inter-dot tunnel coupling, and therefore fast spin projection can be achieved irrespective of the integration time of the charge sensor. Additionally, the separation of fast spin to charge conversion and relatively slow charge readout allows spin projection with greater temporal resolution than may in principle be achieved with a typical charge sensor and a readout protocol that relies on stochastic inelastic tunneling [84].

Chapter 6

LZSM Interferometry of Single Hole Tunneling

The spatial charge configuration of an electron in a quantum dot has been thoroughly investigated [99–102] owing to the relative ease with which the charge degree of freedom of a qubit can be manipulated and read out. The charge degree of freedom's sensitivity to electric fields is both a boon and a challenge due the presence of electrical noise, limiting the coherence times of electrically driven charge qubits to a typical range from 100 ps to 10 ns.

Despite the sensitivity to noise, the charge degree of freedom can be an asset in charged spin qubit systems. Hybridized spin/charge qubits have been investigated [103, 104] and shown to possess longer coherence times than simple charge qubits by one or two orders of magnitude. The readout of spin qubits can be achieved by converting spin information into charge information, and the previous chapter is just one example of such spin to charge conversion techniques. Normally, the magnetic moment of a free electron does not directly couple to the electric field and must be manipulated through a magnetic field as in [105–107]. In semiconductor quantum dots, however, electrical control of spin has has been achieved using inhomogeneous magnetic fields [108–111]. In these techniques the spatial charge distribution may be oscillated with an electric field to create an effective oscillating magnetic field. This technique drives the spin through the charge degree of freedom without entangling them.

Electrical control of spin qubits through the spin-orbit interaction has been demonstrated for electrons in GaAs [112, 113] and InAs [114, 115] devices, though the SOI is weaker for electrons in those systems than for holes in GaAs. Similar methods may be applicable for holes to achieve high speed spin qubit control and work towards that goal is in progress at the time of writing.

In previous chapters, spin to charge conversion has been demonstrated using the unique properties of holes. Moreover, spin flipping charge tunneling transitions have been discussed in the context of transport measurements. In this chapter, the coherent driving of a hole charge qubit and hybrid spin/charge qubit will be demonstrated and analyzed using Landau Zener Stueckelberg Interferometry. This analysis will reveal the coherence of the spin conserving and non-conserving transitions. Finally, simultaneous coherent driving of multiple transitions in the double quantum dot will be demonstrated and discussed.

6.1 Introduction to Two Level LZSM Interferometry

The technique of LZSM interferometry [116], used for example to study the coherence of charge qubits [101, 112, 117–121], involves the application of radio frequency electric fields to modulate the energy separation of (at least) two energy levels, causing them to cross repeatedly. During the transition through zero separation, some of the population of each level will be coherently transfered to the other. Successive transitions may have a cummulative (constructive) or negative (destructive) effect on the state of the system, depending on the phase evolution of the system between transitions, leading to interference patterns in the time-averaged state of the system.

An intuition for LZSM Interference can be obtained by examining the adiabatic impulse model [116], which will be summarized below.

Suppose a two level system, for example a charge qubit in a double quantum dot with levels (1,0) and (0,1), is driven through an anti-crossing by an electromagnetic field. The Hamiltonian of such a system is:

$$H_0 = \begin{bmatrix} \frac{\Delta\epsilon}{2} & t \\ t & -\frac{\Delta\epsilon}{2} \end{bmatrix} \tag{6.1}$$

$$H_{AC}(t) = \begin{bmatrix} \frac{A\sin(\omega t)}{2} & 0 \\ 0 & -\frac{A\sin(\omega t)}{2} \end{bmatrix} \tag{6.2}$$

$$H = H_0 + H_{AC} \tag{6.3}$$

where the tunneling matrix element t parameterizes the gap between the two states at zero detuning.

The eigenstate energies of the time-independent part of the Hamiltonian (H_0) are plotted in figure 6.1, while the time-dependent energies of the instantaneous eigenstates of the full Hamiltonian are plotted in figure 6.2. In the adiabatic impulse model, the evolution of the system is assumed to be adiabatic far from the anticrossing and non-adiabatic at each anti-crossing, where coherent Landau-Zener transitions occur between the two levels.

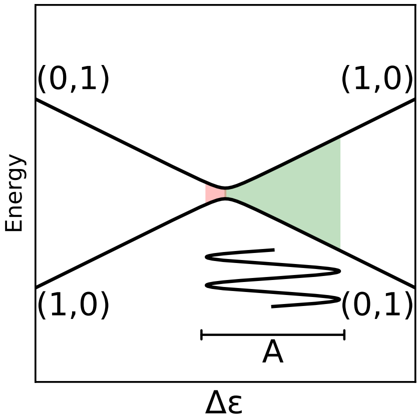

Figure 6.1: Sketch of eigenstate energies of H_0 vs. detuning. In LZSM interference experiments, the two levels of the system are detuned off resonance and driven by a microwave field of amplitude A. In this example, A is sufficiently large to repeatedly drive the system through the avoided crossing, where the energy levels are inverted. Respectively, green and red show where positive and negative phase accumulation occurs.

If $|\Delta\epsilon| < A$ the system will undergo two Landau-Zener transitions per cycle, whereas away from the anti-crossings the system will accumulate alternating positive and negative phases denoted θ_0 and θ_1 in figure 6.2. The four parts of the cycle are as follows:

- Adiabatic evolution of the detuning away from the crossing. A dynamical phase (θ_0) is accumulated.
- Landau Zener crossing of the two levels. The crossing is modeled as an arbitrary unitary operator $\hat{U}$.
- Adiabatic evolution of the detuning away from the crossing. A dynamical phase (θ_1) is accumulated.

- The second Landau Zener crossing. This crossing is modeled by the inverse operation $\hat{U}^{-1}$.

The total phase accumulated by the system in one cycle of the detuning oscillation is $\Delta\theta = \theta_0 - \theta_1$.

Successive coherent Landau-Zener transitions through the anti-crossings can cummulatively cause coherent oscillations between the (0,1) state to the (1,0) state over time. However, alternating Landau-Zener transitions in this case proceed in opposing directions and therefore invert one another, preventing a cummulative effect. This suppression is lifted when the phase of the qubit is changed between transitions (θ_0 and θ_1 are not both multiples of 2π). In the case that the accumulated phases are inverted between transitions, constructive interference occurs instead.

In fact, constructive interference will occur when two conditions are met. First, if $\Delta\theta = 2\pi N$ for any integer N, then the net rotation of the qubit over one cycle preserves phase (or azimuthal angle in the Bloch sphere). A rotation preserving phase necessarily maximizes the amplitude of the oscillation between the eigenstates ((0,1) and (1,0)). $\Delta\theta$ can be obtained by integration of the diagonal elements of the Hamiltonian (neglecting the tunneling element t):

$$\Delta\theta = \frac{1}{\hbar}\int_0^{\frac{2\pi}{\omega}} (A\sin(\omega t) + \Delta\epsilon)dt \tag{6.4}$$

$$= \frac{2\pi\Delta\epsilon}{\hbar\omega} \tag{6.5}$$

This gives:

$$\Delta\epsilon = N\hbar\omega \tag{6.6}$$

The first condition can be satisfied and constructive interference fringes are expected at evenly spaced intervals in $\Delta\epsilon$ with period equal to the photon energy.

However, this first condition only guarantees the phase is inverted an even number of times per cycle. In fact, constructive interference is maximized when each individual transition is accompanied by an odd number of phase flips, or

$$\theta_0 = (2k+1)\pi \tag{6.7}$$

for some integer k, whereas $\theta_0 = 2k\pi$ corresponds to destructive interference because the second transition in every cycle becomes the inverse of the first. Since θ increases with A for any given value of $\Delta\epsilon$, oscillatory behaviour is expected in each interference fringe with increasing A.

Figure 6.3 shows a pattern of LZSM fringes for a simulated two level system with driving field of frequency $\frac{\omega}{2\pi} = 3.0$ GHz amplitude A varied between 0 µV and 100 µV. As predicted, fringes are visible evenly spaced by the photon energy $\hbar\omega$, with a central fringe visible at zero detuning and zero amplitude. Moreover, the amplitudes of the fringes oscillate with increasing A and more fringes are visible at greater detuning as the amplitude increases.

To summarize:

- Constructive LZSM interference is possible near $\Delta\epsilon \approx N\hbar\omega$.
- Constructive LZSM interference occurs when $|\Delta\epsilon| < A$, the amplitude of the modulation.
- Maximal constructive LZSM interference occurs when $\theta_0 = (2k+1)\pi$ and therefore $\theta_1 = (2l+1)\pi$ for some integers k,l.
- Because θ_0 and θ_1 both vary with A, oscillations between constructive and destructive interference are expected with A for each fringe.

Alternate Dressed State Approach Suppose a quantum dot is described by a local Hamiltonian H consisting of a time-independent component H_0 and a sinusoidal time-dependent component.

$$H(\vec{r},t) = H_0(\vec{r},t) + A\cos(\omega t) \tag{6.8}$$

Here the time-dependent term could reflect the oscillating electric potential created by microwaves applied to an electrostatic gate, where the wavelength of the electric field is much larger than the characteristic length scales of the potential itself. Because there is no spatial dependence in the time-dependent perturbation, we can solve the time-dependent Schrodinger equation exactly. Where ψ_0 solves the time-independent H_0, the following ansatz can be shown to satisfy the full Schroginger equation:

$$\psi(\vec{r},t) = \psi_0(\vec{r},t)\exp\left\{-\frac{i}{\hbar\omega}A\sin(\omega t)\right\} \tag{6.9}$$

In detail:

$$i\hbar\frac{\mathrm{d}\psi(\vec{r},t)}{\mathrm{d}t} = H_0\psi(\vec{r},t) + A\cos(\omega t)\psi(\vec{r},t) \tag{6.10}$$

$$\begin{aligned}
&i\hbar\frac{\mathrm{d}\psi_0}{\mathrm{d}t}\exp\left\{-\frac{i}{\hbar\omega}A\sin(\omega t)\right\}\\
&+i\hbar\left(-\frac{i\omega}{\hbar\omega}\right)\psi_0 A\cos(\omega t)\exp\left\{-\frac{i}{\hbar\omega}A\sin(\omega t)\right\}\\
&=H_0\psi_0\\
&+A\cos(\omega t)\psi_0\exp\left\{-\frac{i}{\hbar\omega}A\sin(\omega t)\right\}
\end{aligned} \tag{6.11}$$

Terms 1 and 3 of equation 6.11 are the Schrodinger equation as applied to H_0 and ψ_0, and therefore cancel. Terms 2 and 4 cancel directly. Therefore, $\psi(\vec{r},t) = \psi_0(\vec{r},t)\exp\left\{-\frac{i}{\hbar\omega}A\sin(\omega t)\right\}$ solves the Schrodinger equation.

The time-dependent exponential term can be expressed as a power series in Bessel functions using the identity:

$$\exp\left\{-\frac{i}{\hbar\omega}A\sin(\omega t)\right\} \equiv \sum_{N=-\infty}^{\infty} J_n\left(\frac{A}{\hbar\omega}\right)\exp\{-iN\omega t\} \tag{6.12}$$

$$\psi(\vec{r},t) = \psi_0(\vec{r},t)\sum_{N=-\infty}^{\infty} J_n\left(\frac{A}{\hbar\omega}\right)\exp\{-iN\omega t\} \tag{6.13}$$

Under an oscillating spatially-independent perturbation, the eigenstates H_0 therefore lose the quality of a single scalar energy eigenvalue, instead becoming spread over a discrete spectrum of quasi-energies $E_N = N\hbar\omega$, where ω is the frequency of the driving perturbation [122]. The amplitude of the N-th pseudo-level is the bessel function of the first kind of order N with the ratio of the driving amplitude to the energy $\hbar\omega$ as its argument. This function is oscillatory in its parameter, so we expect oscillations in the amplitude of each pseudo-level with increasing driving amplitude.

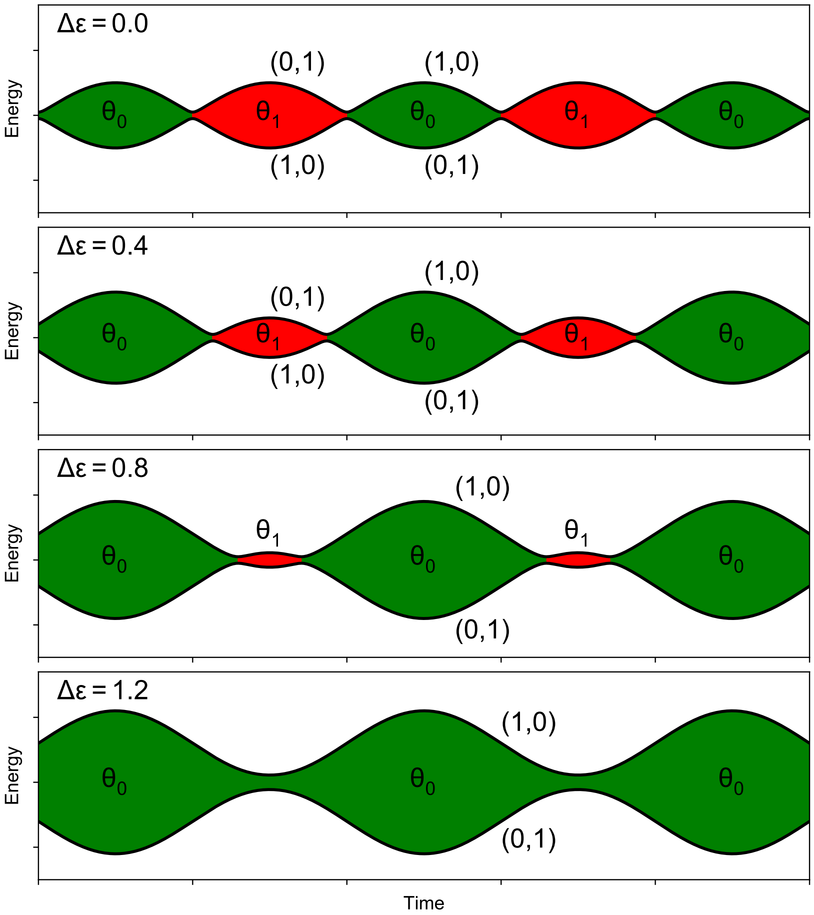

Figure 6.2: Energies (in arbitrary units) of the eigenstates for charge qubit driven by an oscillating detuning for various average separations $\Delta\epsilon$ relative to the detuning modulation amplitude. The qubit accumulates alternating positive (θ_0) and negative (θ_1) phases between crossings of the two energy levels. The phase accumulated depends on both the amplitude of the oscillation and the average detuning.

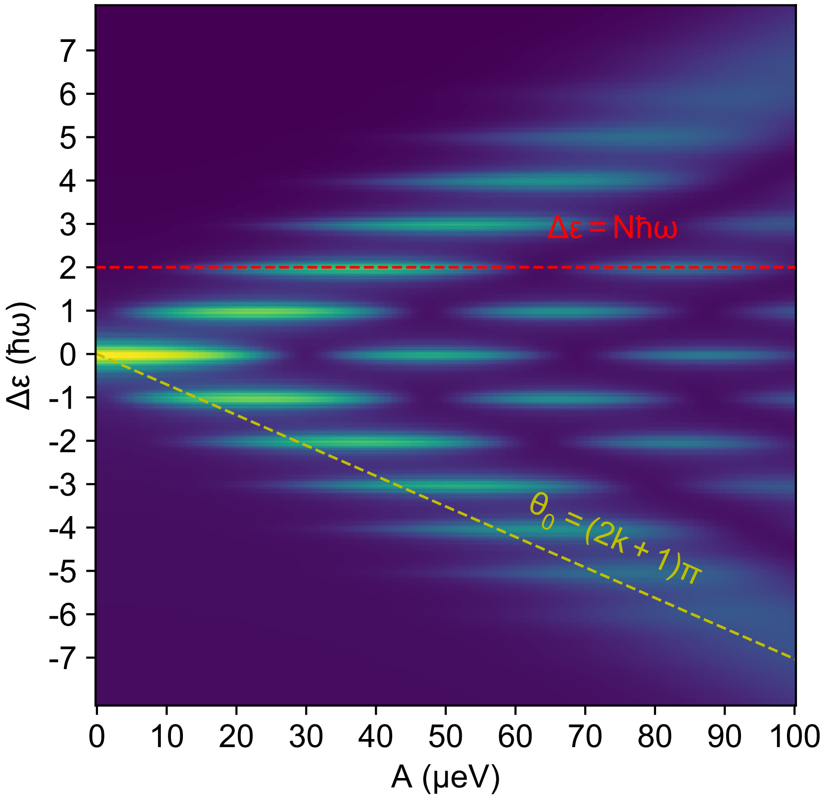

Figure 6.3: Time-averaged occupation of the excited state of a numerically simulated two level system described by equation 6.3 initially in the ground state. Fringes appear for finite A, equally spaced in $\Delta\epsilon$ by multiples of the photon energy $\hbar\omega$, and the amplitude of each fringe oscillates with A. Dashed lines roughly mark example loci where each of the two conditions for constructive LZSM interference are met. Maxima occur where both conditions are met simultaneously. Here $f = 3$ GHz was chosen.

6.2 Coherence in LZSM Interferometry

The discussion so far has involved an ideal decoherence-free model of LZSM interference. The effect of phase decoherence in LZSM is to broaden and eventually extinguish the fringes along the detuning axis. To see why this must be so, recall that the condition for constructive interference in equation 6.1 arises because of the relationship between energy and phase. The phase of the qubit must be preserved over each cycle of the driving field to achieve maximum constructive interference. If the phase accumulation is probabilistic with increasing uncertainty over time, the energy matching condition can be expected to broaden and the maximum degree of constructive interference can be expected to decrease.

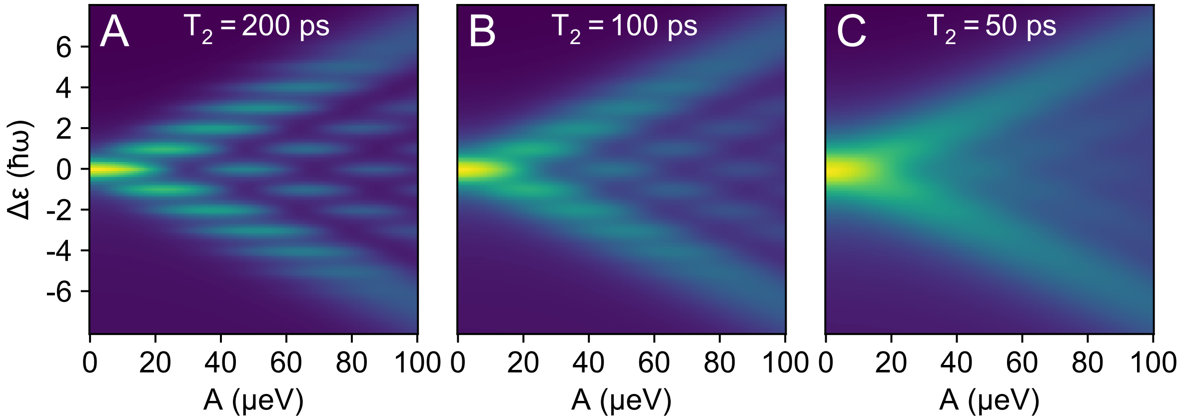

Figure 6.4: Time-averaged occupation of the excited state of a numerically simulated two level system described by equation 6.3 with phase decoherence introduced. The phase coherence lifetime T_2 is varied as indicated. Here $f = 3$ GHz was chosen.

The numerical model that produced figure 6.3 can be extended to include phase decoherence described by a mean phase lifetime T_2. Results are plotted in figure 6.4, where T_2 is varied from 200 to 50 ps. The effect of reduced phase coherence is to broaden the interference fringes, allowing the phase coherence lifetime to be extracted from a fit to the model [65].

The following section will detail an experiment where the technique of LZSM inteferometry was used to experimentally study the coherence of spin preserving and spin flipping transitions of a hole in a double quantum dot using similar numerical simulation techniques.

6.3 LZSM Interferometry of Inter-dot Transitions

The spin flipping charge tunneling transitions have been discussed and analyzed with transport measurements in previous chapters. This section presents an LZSM inteferometry experiment that independently demonstrates the coherence of these transitions and the potential for coherent manipulation of hole charge qubits and spin qubits through the charge degree of freedom.

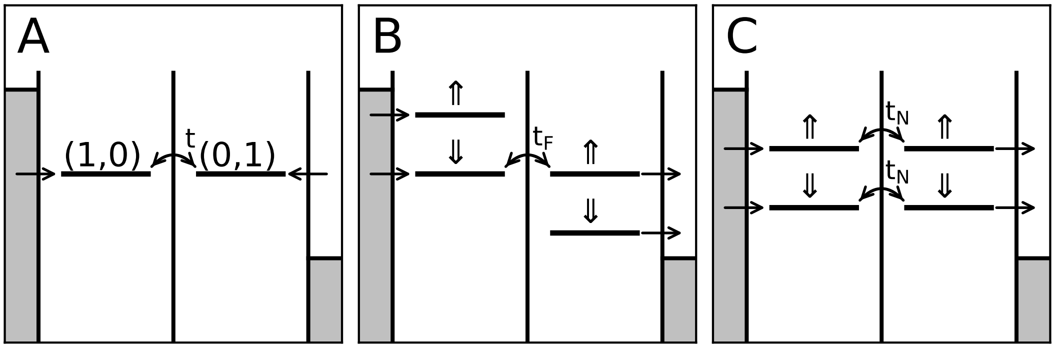

Figure 6.5: Energy level diagram showing experimental settings for LZSM interferometry. The device was tuned such that the four lowest DQD states were within the bias window, but the panels show particular configurations: ***A****)* $\Delta\epsilon = E_Z = 0$*,* ***B****)* $\Delta\epsilon = E_Z > 0$*, and* ***B****)* $E_Z > \Delta\epsilon = 0$*.*

The experiment was performed with the device configured in the single hole regime, near the intersection of the (1,0) and (0,1) charge stability regions of the device. Figure 6.5 illustrates the tuning of the device for this experiment. A positive bias $V_{DC} = 2$ mV was applied and the transport current was recorded as in the magnetospectroscopy experiments of chapter 4. In addition, an oscillating voltage was applied to gate 'L' through the high-frequency transmission line to induce an oscillating detuning:

$$\Delta\epsilon(t) = V_0 sin(2\pi f t) + \Delta\epsilon_0 \tag{6.14}$$

where V_0 is the amplitude of the modulation. f is the frequency of the detuning modulation, typically several GHz, and $\Delta\epsilon_0$ is the static (time-independent) component of detuning typically on the order of several hundred µeV.

The relationship between V_0 and the controllable microwave power output of the microwave generator P depends on fine details of the microwave circuit; including the frequency dependence of the transmission line impedance, the gate capacitance, and the quantum dot shape and orientation. Figure 6.6 demonstrates that this frequency dependence of V_0 exists for fixed generator output power over the frequency range of interest. With no magnetic field applied and for a fixed output power of $P = -20$ dBm, the output frequency of the microwave generator was varied between 4 and 20 GHz while the detuning was swept between -150 and 150 µeV. While the positions of the fringes vary linearly with the applied frequency, as expected according to equation 6.1, their amplitudes vary considerably and unpredictably in the GHz regime.

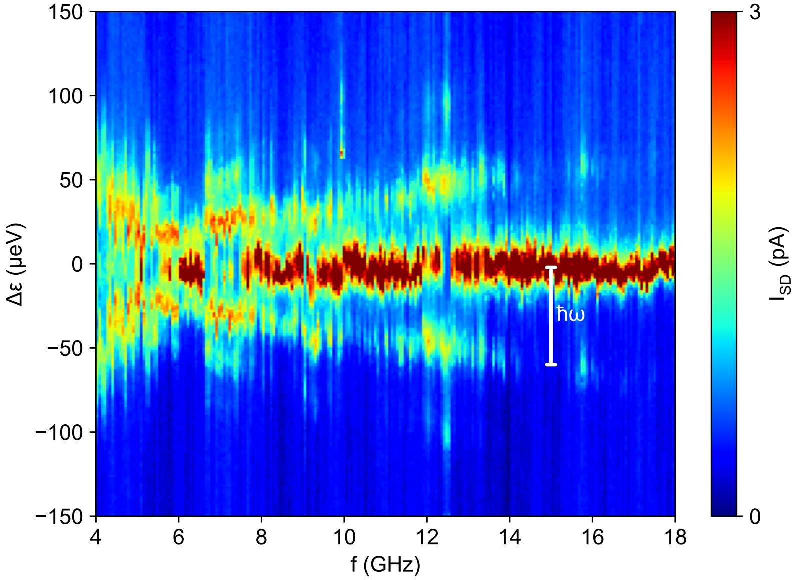

Figure 6.6: LZSM spectra in transport current, obtained by sweeping $\Delta\epsilon$ and varying the driving frequency f.

Owing to the linearity of the microwave transmission circuit, for fixed frequency the power can be varied to reveal an LZSM interference spectrum in the transport current. Again with zero applied magnetic field, spectra were obtained by sweeping detuning and varying the applied power at different discrete frequency values where the circuit exhibited good transmission. The results are plotted in figure 6.7.

When little to no power is applied, a single resonant current line is visibile at $\epsilon = 0$ as observed in section 4.4. With increasing microwave power, the single resonance at zero field developed multiple side-resonances at positive and negative detunings equal to multiples of the photon energy hf. In addition to the appearance of higher order resonances with increasing power, the fringes showed oscillatory behaviour with applied power as expected.

The side-resonances can be explained by LZSM driving of the two level system consisting of the (1,0) and (0,1) charge levels of the double quantum dot. With no microwave field applied, the current is supressed by Coulomb blockade for $\Delta\epsilon < 0$ and limited to inelastic relaxation from the (0,1) charge state to the (1,0) charge state for $\Delta\epsilon < 0$. At $\Delta\epsilon = 0$, however, there is a resonant enhancement to the current because (0,1) and (1,0) are hybridized and neither is a time-independent eigenstate of the system. When a microwave field is applied, (0,1) and (1,0) become hybridized at discrete values of detuning corresponding to the conditions for constructive LZSM interference. The transport current is directly proportional to the amplitude of oscillation between (0,1) and (1,0) or the time-averaged occupation of the (1,0) state when the system is initialized in (0,1).

Notably, the (1,0), (0,1) charge qubit is not a true two level system because the charge states contain doubly degenerate spin sub-levels. Indeed, the degeneracy is broken and a multi-level LZSM spectrum appears in transport when a magnetic field is applied.

Just as in section 4.4, a second resonant enhancement to the current appears at $\epsilon = E_Z$. When microwaves are applied the signature of LZSM interference is revealed at both resonances. Figure 6.8 shows LZSM fringes at B=1.34 T and B=2.1 T. As before, for positive V_{DC}, the $\epsilon = -E_Z$ resonance cannot lift the blockade condition and thus is not expected to be visible in transport.

Both figures 6.7 and 6.8 present numerically simulated transport through the double quantum dot. The simulation models the lowest four energy levels of the DQD near the (0,1)/(1,0) degeneracy, and is discussed in more detail in [64] and in appendix A. The state space of simulation is spanned by four basis states: $(\Uparrow,0)$, $(\Downarrow,0)$, $(0,\Uparrow)$, and $(0,\Downarrow)$; where for example $(0,\Downarrow)$ represents precisely one hole in the right dot in the lower spin state. In the weak tunneling regime, the system can be described by the following Hamiltonian:

$$H = \begin{bmatrix} \frac{\Delta\epsilon}{2} + \frac{E_Z}{2} & 0 & -t_N & -it_F \\ 0 & \frac{\Delta\epsilon}{2} - \frac{E_Z}{2} & -it_F & -t_N \\ -t_N & it_F & -\frac{\Delta\epsilon}{2} + \frac{E_Z}{2} & 0 \\ it_F & -t_N & 0 & -\frac{\Delta\epsilon}{2} - \frac{E_Z}{2} \end{bmatrix} \tag{6.15}$$

where t_N and t_F are the spin non-flipping and spin flipping tunneling matrix elements respectively and $E_Z = g^*\mu_B B$ is the Zeeman energy.

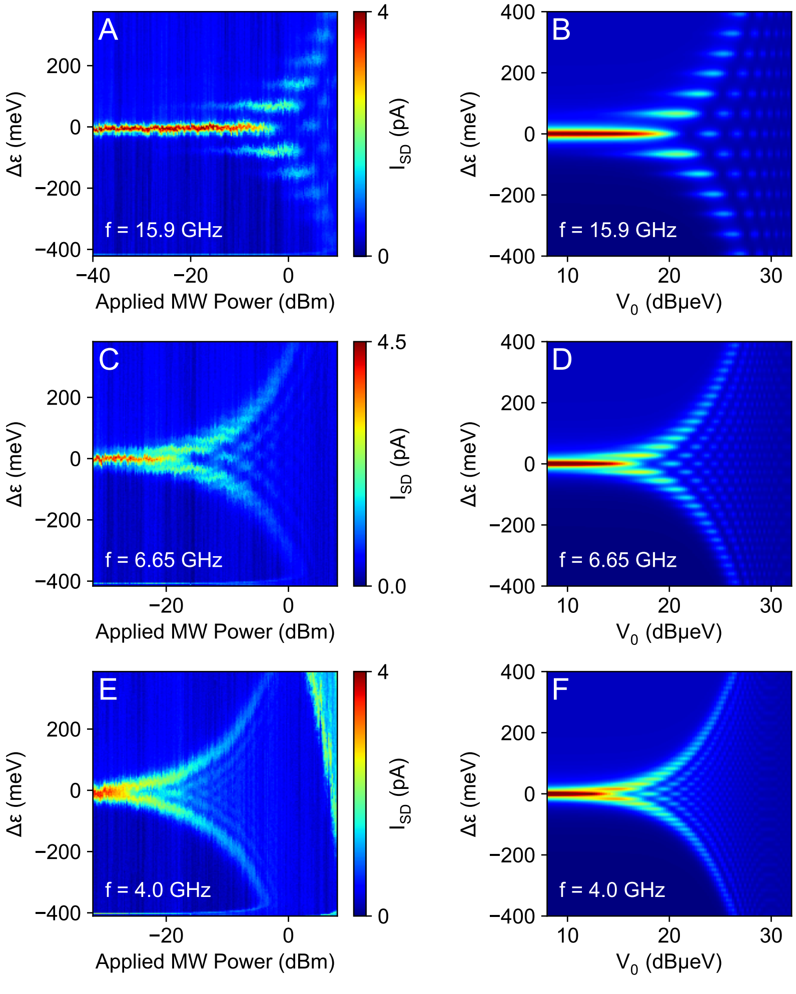

Figure 6.7: ***A***, ***C***, ***E***: *Tunneling current through the quantum dot with microwave excitation applied to gate L at various frequencies. Generated power is varied and photon assisted tunneling fringes appear.* ***B***, ***D***, ***F***: *Simulated tunneling current for the conditions given in 6.1.*

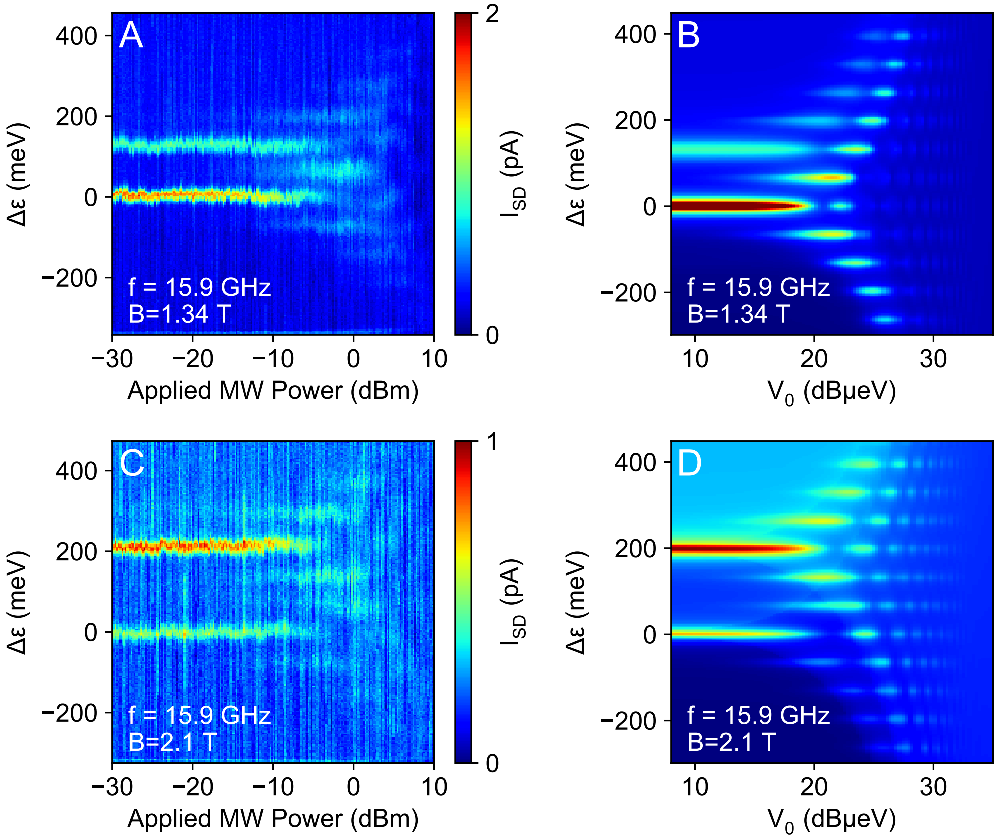

Figure 6.8: ***A***, ***C***: *LZSM interferometry with a magnetic field applied. Tunneling current is measured as detuning and microwave power are varied, at the indicated frequencies and magnetic fields.* ***B***, ***D***: *Numerical simulation for the conditions given in table 6.2.*

Figure 6.9 panel A is a diagram of the energies of the four steady states as a function of detuning at zero field. In this case the spin eigenstates are always degenerate and there is one anticrossing between the doubly-degenerate charge states, (1,0) and (0,1). In the zero B limit the minimum energy splitting t is a combination of the off-diagonal Hamiltonian parameters: $t = \sqrt{t_F^2 + t_N^2}$.

Figure 6.9 panel B is a similar diagram showing the case of finite field where the Zeeman term is larger than t. The spin degeneracy is lifted and there are four anti-crossings: two

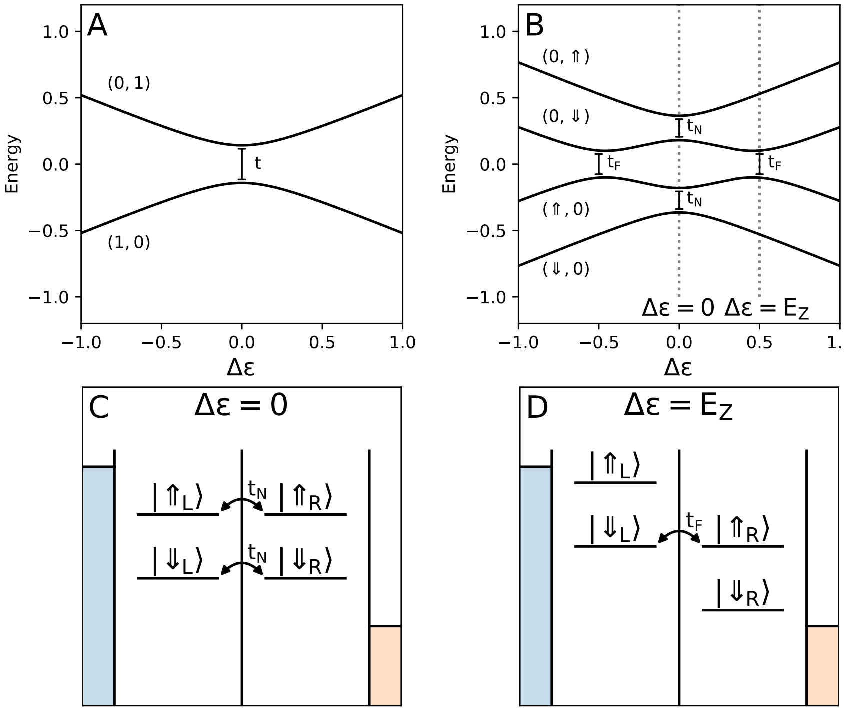

Figure 6.9: ***A**) Diagram of eigenstate energies as a function of detuning at $B = 0$ with $t_F = t_N = 0.1$. Upper and lower branches are spin-degenerate, and at extreme detuning are composed of distinct and localized charge states in each dot. Axes indicate arbitrary units.* ***B**) Similar diagram with $B = 0.5$. At extreme detuning eigenstates correspond to well defined and localized spin states.*

between states of similar spin (at $\epsilon = 0$) and two more for dissimilar spin (at $\epsilon = \pm E_Z$).

The single anti-crossing at zero field is qualitatively analogous to the expected case for electrons in GaAs except that t would be dominated by t_N in the electron case. Unlike the electron case in GaAs, however, additional prominent anti-crossings appear at finite detuning and originate from the spin-orbit interaction [37, 52, 64, 123, 124]. The anti-crossings are individually parameterized by spin flipping and non-flipping tunneling matrix elements, t_F and t_N respectively, as shown in figure 6.9. Panels C and D show the alignment

Panel	f (GHz)	B (T)	t (μeV)	T_1 (μs)	T_2 (ps)
B	15.9	0.0	0.375	0.8	60
D	6.7	0.0	0.375	0.8	75
E	4.0	0.0	0.375	0.8	90

Table 6.1: Parameter values used to reproduce the LZSM interference patterns in figure 6.7.

Panel	f (GHz)	B (T)	t_F (μeV)	t_N (μeV)	T_{1S} (μs)	T_{1N} (μs)	T_{1F} (μs)	T_2 (ps)
B	15.9	1.34	0.28	0.26	1	2.421	2.721	70
D	15.9	2.1	0.125	0.08	1	2.421	2.721	70

Table 6.2: Parameter values used to reproduce the LZSM interference patterns in figure 6.8.

of energy levels at $\epsilon = 0$ and $\epsilon = E_Z$ conditions for $E_Z >> t$. These conditions support resonant enhancements to charge transport, exactly as in section 4.4, whereas the $\epsilon = -E_Z$ case is energetically blockaded for positive V_{DC}.

The LZSM fringes in figures 6.7 and 6.8 were reproduced with a numerical four-level model based on the Hamiltonian in equation 6.3 and several incoherent processes. The master equation for the model was:

$$\frac{\partial}{\partial t}\rho(t) = -\frac{i}{\hbar}\left[H, \rho(t)\right] + \hat{\Gamma}_{in} + \hat{\Gamma}_{out} + \hat{\Gamma}_{T2F} + \hat{\Gamma}_{T2N} + \hat{\Gamma}_{T1N} + \hat{\Gamma}_{T1F} + \hat{\Gamma}_{T1S} \tag{6.16}$$

where the operators $\hat{\Gamma}_{in}$ and $\hat{\Gamma}_{out}$ represent tunneling into the (0,1) and out of the (1,0) states respectively, $\hat{\Gamma}_{T2N}$ and $\hat{\Gamma}_{T2F}$ respresents phase decoherence of the spin conserving and non-conserving transitions, $\hat{\Gamma}_{T1N}$ and $\hat{\Gamma}_{T1F}$ represent spin non-flipping and flipping charge relaxation, and finally $\hat{\Gamma}_{T1S}$ is the relaxation of the spin excited state inside each quantum dot. These relaxation pathways are depicted in figure 6.10. The simulation algorithm and fitting procedure are presented in more detail elsewhere [64]. Table 6.1 presents the values that best reproduced the LZSM spectra at zero field. At zero field the quasi two level system is described by the single tunneling matrix parameter t and just two decoherence parameters: T_1 (relaxation) and T_2 (dephasing). Table 6.2 presents the input values used at finite field where the system is described by two matrix elements t_F and t_N. The dephasing times T_{2F}, T_{2N} were found to be sufficiently similar that the same value (denoted T_2) was used for both.

In chapter 4.4 it was found that above $B = 0.7$ T the spin flipping and non-flipping tunneling matrix elements were similar in magnitude, as was reflected in this experiment as

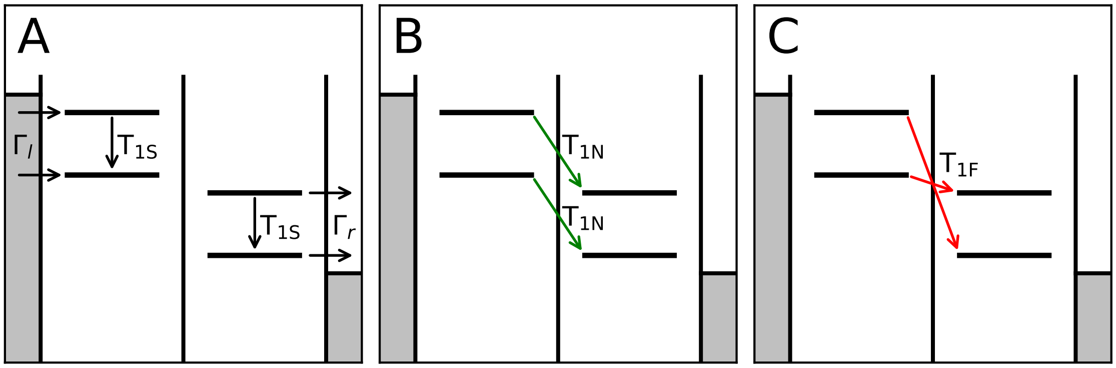

Figure 6.10: Sketch of the incoherent processes and relaxation pathways included in the double quantum dot model, all of which act simultaneously. ***A*** *Tunneling to the left dot from the left lead at a rate* Γ_l *when the double quantum dot is empty, as well as tunneling from the right dot to the right lead at a rate* Γ_r *when the right dot is full. Spin relaxation within each dot is parameterized by a mean lifetime* T_{1S}*.* ***B*** *Inter-dot relaxation preserving spin is parameterized by the mean lifetime* T_{1N}*.* ***C*** *Inter-dot relaxation with a spin flip is parameterized by a single mean lifetime* T_{1F}*.*

well. Moreover, the phase coherence of the LZSM driven tunneling appears to be similarly coherent for both processes, and thus the coherence of the spin/charge hybrid qubit driven in this manner does not appear to be limited by spin decoherence. Both the spin flipping and non-flipping processes are similarly strong and similarly coherent. In electron spin qubits in GaAs, spin non-conserving tunneling has been observed assisted by the hyperfine interaction [94]. However, this process is much slower (by at least an order of magnitude) than non-spin-flip tunneling and is not a coherent process, and therefore cannot be used for coherent spin manipulations. In this system, both the spin preserving and non-preserving transitions can be coherently driven simultaneously, as will be demonstrated in the following section.

6.4 Simultaneous Driving of Inter-Dot Transitions

In the previous section, it was demonstrated that spin flipping and non-flipping transitions could be driven equally coherently with a microwave field applied to a gate. This section will briefly discuss simultaneous driving of multiple transitions.

When driven by a microwave field, the positions of the LZSM fringes attributable to the spin preserving transition are fixed as a function of $\Delta\epsilon$. However, the positions of the fringes attributable to the spin flipping transitions are not fixed with magnetic field, and indeed their positions vary linearly with the applied field.

Figure 6.11 shows the evolution of these fringes with field for high frequency, $f = 19.56$ GHz and microwave power $P = 0$ dBm. Panel A shows measured LZSM spectra in transport, whereas panel B is a simulation. The current is visibly enhanced where the fringes coincide, which occurs under two distinct conditions: first, there are the points where $E_Z = (N + \frac{1}{2})\hbar\omega$ and $\Delta\epsilon = (M + \frac{1}{2})\Delta\epsilon$ for integers N, M. One such point is identified as point 1 in panel B, and this condition corresponds to constructive interference of both spin-flipping transitions as depicted in panel C. While normally only one of these transitions produces fringes because only one lifts the blockade condition for the ground state $(0,\Downarrow)$, the current is still limited by incoherent relaxation from $(0,\Uparrow)$ unless this state is also mixed with one or both states from the (1,0) manifold. At points that satisfy these conditions, both states are hybridized with the (1,0) state of opposite spin and a current enhancement is observed. In this configuration the hole is resonantly driven between the two dots with a spin flip.

The second class of coincidence occurs where $E_Z = N\hbar\omega$ and $\Delta\epsilon = M\hbar\omega$ for some integers M, N. One example is identified as point 2 in panel B, and these coincidences

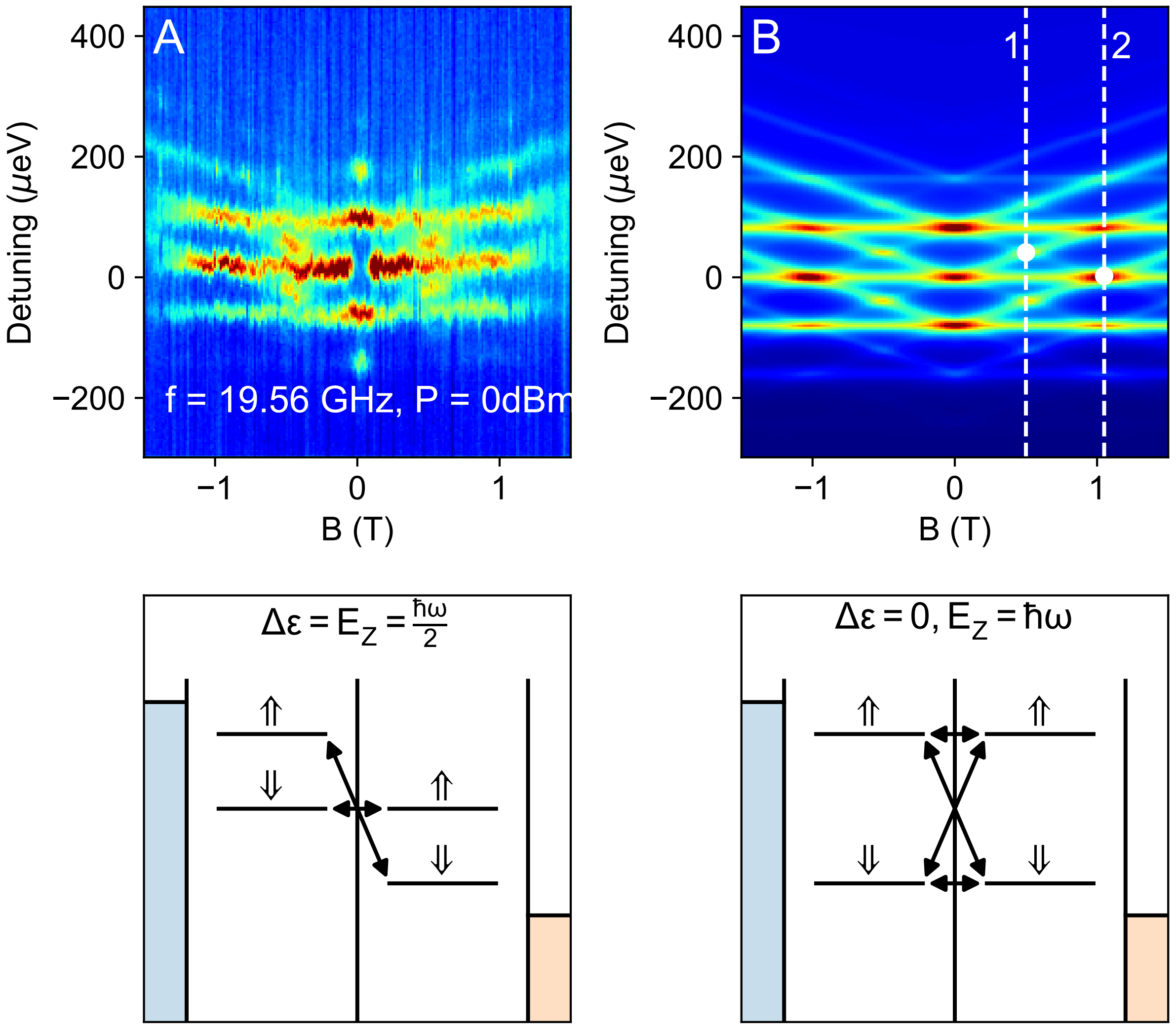

Figure 6.11: ***A****) LZSM interference fringes measured in transport for F=19.56* GHz. ***B****) Simulation of the conditions in panel A. Two concidences of fringes are identified: points 1 and 2.* ***C****) Diagram showing the alignment of energy levels and the two active transitions at point 1.* ***D****) Similar diagram corresponding to point 2 showing the four active transitions.*

correspond to simultaneous driving of both spin-flipping transitions *and* both spin preserving transitions. Again an enhancement in the current is expected and observed at point 2, even though $\hbar\omega = M\Delta\epsilon$ is itself sufficient to lift blockade. Here the enhancement is due to the constructive interference of multiple transitions being driven simultaneously.

6.5 Conclusions

In this chapter, the technique of Landau Zener Stueckelberg Majorana Interferometry was applied to transport through a double quantum dot in the single hole regime. From the experiment, the coherence of the spin orbit induced spin flipping tunneling processes between dots was estimated and found to be similar to that of the spin preserving tunneling process in the same system ($T_2 \sim 70$ ps). In previous chapters, the large spin-flip tunneling of holes in quantum dots was applied to develop a novel spin projection technique, but this technique did not rely on the coherence of the tunneling process. In this chapter coherent driving of singular or multiple transitions in the double quantum dot are possible in this system owing to the spin-orbit enabled spin flip tunneling exibited by holes, potentially enabling new functionalities and spin control.

Chapter 7

Conclusions and Future Work

This work has presented transport and charge detection measurements of holes in double quantum dot. From those measurements, several conclusions can be drawn.

First, resonant transport spectroscopy experiments presented in chapter 4 demonstrated a dramatic anisotropy in the effective g-factor of the holes (with a maximum effective g-factor of $g^* = 1.45$), consistent with heavy holes. The confinement of heavy holes in quantum dots has been suggested as a route to the suppression of an important source of decoherence for spin qubits in GaAs: interactions with the spins of the lattice nuclei [125]. Further study of the phase coherence of single heavy hole spin qubits in this system is in progress.

In addition to the anisotropic g-factor, a form of spin blockade was observed at small fields for these heavy holes; the blockade was lifted by the strong spin orbit interaction for larger z-directed magnetic fields. Other experimental studies have demonstrated pauli spin blockade to be anisotropic in GaAs quantum dots in the many hole regime [44]. Whereas the g-factor should be minimized for an applied field anywhere in the plane of the two-dimensional hole gas, the effective spin-orbit field B_{SO} defines a particular axis of interest and it would be interesting to study single spin decoherence with full three-dimensional control of the magnetic field.

In chapter 5, a novel spin projection technique was demonstrated as part of a study of hole spin relaxation. This technique took advantage of the unique spin flip tunneling of holes that enabled the resonant transport spectroscopy experiments. By projecting the spin of a single hole onto meta-stable charge states of the double quantum dot, the spin measurement result could be preserved at the device level long enough to extract with a charge detector. It is the author's opinion that latching spin to charge conversion techniques like this are both experimentally practical and are likely to play an important role in future spin qubit technology.

The mean hole spin relaxation time T_1 was measured in a z-directed magnetic field (i.e. along the growth axis) and shown to vary by three orders of magnitude from 53.7 µs at 0.5 T to 0.39 µs at 1.5 T. The spin relaxation time was modeled by a power law in B, showing good agreement with a $T_1 \propto B^{-5}$ power law. This power law is indicative of the microscopic origin of the spin relaxation in Dresselhaus spin orbit mediated interaction with lattice vibrations (phonons), whereas if Rashba spin orbit interaction were dominant it should produce a B^{-9} dependence. These T_1 values compare favourably to other results in the literature for hole spins, which can be expected because heavy hole pseudo-spin relaxation is a third order process.

Finally, Landau Zener Stueckelberg Majorana interferometry was used to study the coherence of inter-dot transitions. It was found that when driven by a microwave excitation, the inter-dot charge transitions were coherent, with mean phase lifetimes of approximately 70 ps. These coherence lifetimes are typical for charge qubits, which are succeptible to noise in local environmental electric field. Nonetheless, this result suggests that it is in principle possible to coherently drive transitions between charge and spin states in hole quantum dots. Future work would ideally strive to control the single spin qubit alone, without entangling it with the charge state, which should extend the coherence time and enable measurement of the phase decoherence time of a single spin qubit. One such study is in progress at the time of writing.

Bibliography

[1] A. M. Turing. “On Computable Numbers, with an Application to the Entscheidungsproblem”. In: *Proceedings of the London Mathematical Society* s2-42.1 (Jan. 1937), pp. 230–265. ISSN: 0024-6115. DOI: `10.1112/plms/s2-42.1.230`.

[2] C. E. Shannon. “A mathematical theory of communication”. In: *The Bell System Technical Journal* 27.3 (July 1948), pp. 379–423. ISSN: 0005-8580. DOI: `10.1002/j.1538-7305.1948.tb01338.x`.

[3] *Simulating Physics with Computers*. Vol. 21. International Journal of Theoretical Physics. Kluwer Academic Publishers-Plenum Publishers, 1982.

[4] A. S. Holevo. “Bounds for the Quantity of Information Transmitted by a Quantum Communication Channel”. In: *Probl. Peredachi Inf.* 9.3 (1973), pp. 3–11.

[5] Roman S. Ingarden. “Quantum information theory”. In: *Reports on Mathematical Physics* 10.1 (Aug. 1976), pp. 43–72. ISSN: 0034-4877. DOI: `10.1016/0034-4877(76)90005-7`.

[6] Jae-yoon Choi et al. “Exploring the many-body localization transition in two dimensions”. en. In: *Science* 352.6293 (June 2016), pp. 1547–1552. ISSN: 0036-8075, 1095-9203. DOI: `10.1126/science.aaf8834`.

[7] Anton Mazurenko et al. “A cold-atom Fermi–Hubbard antiferromagnet”. en. In: *Nature* 545.7655 (May 2017), pp. 462–466. ISSN: 1476-4687. DOI: `10.1038/nature22362`.

[8] Florian Neukart et al. “Traffic flow optimization using a quantum annealer”. In: *arXiv:1708.01625 [quant-ph]* (Aug. 2017). arXiv: 1708.01625.

[9] P. Shor. “Polynomial-Time Algorithms for Prime Factorization and Discrete Logarithms on a Quantum Computer”. In: *SIAM Journal on Computing* 26.5 (Oct. 1997), pp. 1484–1509. ISSN: 0097-5397. DOI: `10.1137/S0097539795293172`.

[10] *Quantum cryptography: Public key distribution and coin tossing*. Vol. 28. IBM Tech. Discl. Bull., 1984, pp. 175–179.

[11] Peter W. Shor and John Preskill. “Simple Proof of Security of the BB84 Quantum Key Distribution Protocol”. In: *Phys. Rev. Lett.* 85 (2 July 2000), pp. 441–444. DOI: 10.1103/PhysRevLett.85.441.

[12] E. Knill, R. Laflamme, and G. J. Milburn. “A scheme for efficient quantum computation with linear optics”. In: *Nature* 409 (Jan. 2001), p. 46.

[13] John Clarke and Frank K. Wilhelm. “Superconducting quantum bits”. In: *Nature* 453 (June 2008), p. 1031.

[14] A. Imamoglu et al. “Quantum Information Processing Using Quantum Dot Spins and Cavity QED”. In: *Phys. Rev. Lett.* 83 (20 Nov. 1999), pp. 4204–4207. DOI: 10.1103/PhysRevLett.83.4204.

[15] Kamyar Saeedi et al. “Room-Temperature Quantum Bit Storage Exceeding 39 Minutes Using Ionized Donors in Silicon-28”. en. In: *Science* 342.6160 (Nov. 2013), pp. 830–833. ISSN: 0036-8075, 1095-9203. DOI: 10.1126/science.1239584.

[16] Louis Gaudreau et al. “Entanglement distribution schemes employing coherent photon-to-spin conversion in semiconductor quantum dot circuits”. en. In: *Semiconductor Science and Technology* 32.9 (2017), p. 093001. ISSN: 0268-1242. DOI: 10.1088/1361-6641/aa788d.

[17] M. V. Gurudev Dutt et al. “Quantum Register Based on Individual Electronic and Nuclear Spin Qubits in Diamond”. en. In: *Science* 316.5829 (June 2007), pp. 1312–1316. ISSN: 0036-8075, 1095-9203. DOI: 10.1126/science.1139831.

[18] G. D. Fuchs et al. “A quantum memory intrinsic to single nitrogen–vacancy centres in diamond”. en. In: *Nature Physics* 7.10 (Oct. 2011), pp. 789–793. ISSN: 1745-2481. DOI: 10.1038/nphys2026.

[19] Lucio Robledo et al. “High-fidelity projective read-out of a solid-state spin quantum register”. en. In: *Nature* 477.7366 (Sept. 2011), pp. 574–578. ISSN: 1476-4687. DOI: 10.1038/nature10401.

[20] P. C. Maurer et al. “Room-Temperature Quantum Bit Memory Exceeding One Second”. en. In: *Science* 336.6086 (June 2012), pp. 1283–1286. ISSN: 0036-8075, 1095-9203. DOI: 10.1126/science.1220513.

[21] David J. Christle et al. “Isolated Spin Qubits in SiC with a High-Fidelity Infrared Spin-to-Photon Interface”. In: *Physical Review X* 7.2 (June 2017), p. 021046. DOI: 10.1103/PhysRevX.7.021046.

[22] Rutger Vrijen and Eli Yablonovitch. “A spin-coherent semiconductor photo-detector for quantum communication”. In: *Physica E: Low-dimensional Systems and Nanostructures* 10.4 (June 2001), pp. 569–575. ISSN: 1386-9477. DOI: 10.1016/S1386-9477(00)00296-4.

[23] E. Yablonovitch et al. “Optoelectronic quantum telecommunications based on spins in semiconductors”. In: *Proceedings of the IEEE* 91.5 (May 2003), pp. 761–780. ISSN: 0018-9219. DOI: 10.1109/JPROC.2003.811799.

[24] A. Pioda et al. “Single-Shot Detection of Electrons Generated by Individual Photons in a Tunable Lateral Quantum Dot”. In: *Physical Review Letters* 106.14 (Apr. 2011), p. 146804. DOI: 10.1103/PhysRevLett.106.146804.

[25] T. Fujita et al. “Nondestructive Real-Time Measurement of Charge and Spin Dynamics of Photoelectrons in a Double Quantum Dot”. In: *Physical Review Letters* 110.26 (June 2013), p. 266803. DOI: 10.1103/PhysRevLett.110.266803.

[26] K. Morimoto et al. “Single photoelectron detection after selective excitation of electron heavy-hole and electron light-hole pairs in double quantum dots”. In: *Physical Review B* 90.8 (Aug. 2014), p. 085306. DOI: 10.1103/PhysRevB.90.085306.

[27] G. Allison et al. “Tuning the electrically evaluated electron Landé g-factor in GaAs quantum dots and quantum wells of different well widths”. In: *Physical Review B* 90.23 (Dec. 2014), p. 235310. DOI: 10.1103/PhysRevB.90.235310.

[28] Akira Oiwa et al. “Conversion from Single Photon to Single Electron Spin Using Electrically Controllable Quantum Dots”. In: *Journal of the Physical Society of Japan* 86.1 (Dec. 2016), p. 011008. ISSN: 0031-9015. DOI: 10.7566/JPSJ.86.011008.

[29] Kazuyuki Kuroyama et al. “Single electron-photon pair creation from a single polarization-entangled photon pair”. En. In: *Scientific Reports* 7.1 (Dec. 2017), p. 16968. ISSN: 2045-2322. DOI: 10.1038/s41598-017-16899-w.

[30] R. Hanson et al. “Spins in few-electron quantum dots”. In: *Reviews of Modern Physics* 79.4 (Oct. 2007), pp. 1217–1265. DOI: 10.1103/RevModPhys.79.1217.

[31] W. G. van der Wiel et al. “Electron transport through double quantum dots”. In: *Reviews of Modern Physics* 75.1 (Dec. 2002), pp. 1–22. DOI: 10.1103/RevModPhys.75.1.

[32] L. Gaudreau et al. “Coherent control of three-spin states in a triple quantum dot”. In: *Nature Physics* 8 (Nov. 2011), p. 54.

[33] Maximilian Russ and Guido Burkard. “Three-electron spin qubits”. en. In: *Journal of Physics: Condensed Matter* 29.39 (Aug. 2017), p. 393001. ISSN: 0953-8984. DOI: 10.1088/1361-648X/aa761f.

[34] Alex Bogan et al. “Strategies for tuning a linear quadruple quantum dot array to the few electron regime”. In: *Applied Physics Letters* 109.17 (Oct. 2016), p. 173108. ISSN: 0003-6951. DOI: 10.1063/1.4966618.

[35] Takumi Ito et al. “Detection and control of charge states in a quintuple quantum dot”. en. In: *Scientific Reports* 6 (Dec. 2016), p. 39113. ISSN: 2045-2322. DOI: 10.1038/srep39113.

[36] Lisa A Tracy, John L. Reno, and Terry W. Hargett. *Fabrication and Characterization of a Single Hole Transistor in p-type GaAs/AlGaAs Heterostructures*. en. Tech. rep. SAND2015–8132, 1221866. Sandia National Labs, Sept. 2015. DOI: 10.2172/1221866.

[37] Denis V. Bulaev and Daniel Loss. “Spin Relaxation and Decoherence of Holes in Quantum Dots”. In: *Physical Review Letters* 95.7 (Aug. 2005), p. 076805. DOI: 10.1103/PhysRevLett.95.076805.

[38] Jan Fischer et al. “Spin decoherence of a heavy hole coupled to nuclear spins in a quantum dot”. In: *Phys. Rev. B* 78 (15 Oct. 2008), p. 155329. DOI: 10.1103/PhysRevB.78.155329.

[39] Ji-Yin Wang et al. “Anisotropic Pauli Spin-Blockade Effect and Spin–Orbit Interaction Field in an InAs Nanowire Double Quantum Dot”. In: *Nano Letters* 18.8 (Aug. 2018), pp. 4741–4747. ISSN: 1530-6984. DOI: 10.1021/acs.nanolett.8b01153.

[40] V. S. Pribiag et al. “Electrical control of single hole spins in nanowire quantum dots”. en. In: *Nature Nanotechnology* 8.3 (Mar. 2013), pp. 170–174. ISSN: 1748-3395. DOI: 10.1038/nnano.2013.5.

[41] A. P. Higginbotham et al. “Hole Spin Coherence in a Ge/Si Heterostructure Nanowire”. In: *Nano Letters* 14.6 (June 2014), pp. 3582–3586. ISSN: 1530-6984. DOI: 10.1021/nl501242b.

[42] Ruoyu Li et al. “Pauli Spin Blockade of Heavy Holes in a Silicon Double Quantum Dot”. In: *Nano Letters* 15.11 (Nov. 2015), pp. 7314–7318. ISSN: 1530-6984. DOI: 10.1021/acs.nanolett.5b02561.

[43] H. Bohuslavskyi et al. “Pauli blockade in a few-hole PMOS double quantum dot limited by spin-orbit interaction”. In: *Applied Physics Letters* 109.19 (Nov. 2016), p. 193101. ISSN: 0003-6951. DOI: 10.1063/1.4966946.

[44] Daisy Q. Wang et al. “Anisotropic Pauli Spin Blockade of Holes in a GaAs Double Quantum Dot”. In: *Nano Letters* 16.12 (Dec. 2016), pp. 7685–7689. ISSN: 1530-6984. DOI: `10.1021/acs.nanolett.6b03752`.

[45] A. Zarassi et al. “Magnetic field evolution of spin blockade in Ge/Si nanowire double quantum dots”. en. In: *Physical Review B* 95.15 (Apr. 2017). ISSN: 2469-9950, 2469-9969. DOI: `10.1103/PhysRevB.95.155416`.

[46] L. Huthmacher et al. “Coherence of a dynamically decoupled quantum-dot hole spin”. In: *Phys. Rev. B* 97 (24 June 2018), p. 241413. DOI: `10.1103/PhysRevB.97.241413`.

[47] V. V. Belykh et al. “Large anisotropy of electron and hole g factors in infrared-emitting InAs/InAlGaAs self-assembled quantum dots”. In: *Physical Review B* 93.12 (Mar. 2016), p. 125302. DOI: `10.1103/PhysRevB.93.125302`.

[48] B. Voisin et al. “Electrical Control of g-Factor in a Few-Hole Silicon Nanowire MOSFET”. In: *Nano Letters* 16.1 (Jan. 2016), pp. 88–92. ISSN: 1530-6984. DOI: `10.1021/acs.nanolett.5b02920`.

[49] Hideo Kosaka et al. “Coherent Transfer of Light Polarization to Electron Spins in a Semiconductor”. In: *Phys. Rev. Lett.* 100 (9 Mar. 2008), p. 096602. DOI: `10.1103/PhysRevLett.100.096602`.

[50] Hideo Kosaka et al. “Coherent transfer of time-bin photons to electron spins in a semiconductor”. In: *Phys. Rev. A* 85 (4 Apr. 2012), p. 042304. DOI: `10.1103/PhysRevA.85.042304`.

[51] L. A. Tracy, T. W. Hargett, and J. L. Reno. “Few-hole double quantum dot in an undoped GaAs/AlGaAs heterostructure”. In: *Applied Physics Letters* 104.12 (Mar. 2014), p. 123101. ISSN: 0003-6951. DOI: `10.1063/1.4868971`.

[52] Denis V. Bulaev and Daniel Loss. “Electric Dipole Spin Resonance for Heavy Holes in Quantum Dots”. In: *Physical Review Letters* 98.9 (Feb. 2007), p. 097202. DOI: `10.1103/PhysRevLett.98.097202`.

[53] Klaus von Klitzing. “The quantized Hall effect”. In: *Reviews of Modern Physics* 58.3 (July 1986), pp. 519–531. DOI: `10.1103/RevModPhys.58.519`.

[54] D. R. Yennie. “Integral quantum Hall effect for nonspecialists”. In: *Reviews of Modern Physics* 59.3 (July 1987), pp. 781–824. DOI: `10.1103/RevModPhys.59.781`.

[55] P. D. Ye et al. “Giant microwave photoresistance of two-dimensional electron gas”. In: *Applied Physics Letters* 79.14 (Sept. 2001), pp. 2193–2195. ISSN: 0003-6951. DOI: `10.1063/1.1408910`.

[56] M. A. Zudov et al. “Shubnikov–de Haas-like oscillations in millimeterwave photoconductivity in a high-mobility two-dimensional electron gas”. In: *Physical Review B* 64.20 (Oct. 2001), p. 201311. DOI: 10.1103/PhysRevB.64.201311.

[57] M. A. Zudov et al. “Evidence for a New Dissipationless Effect in 2D Electronic Transport”. In: *Physical Review Letters* 90.4 (Jan. 2003), p. 046807. DOI: 10.1103/PhysRevLett.90.046807.

[58] Ramesh G. Mani et al. “Zero-resistance states induced by electromagnetic-wave excitation in GaAs/AlGaAs heterostructures”. en. In: *Nature* 420.6916 (Dec. 2002), pp. 646–650. ISSN: 1476-4687. DOI: 10.1038/nature01277.

[59] A.C. Gossard. “Modulation Doping of Semiconductor Heterostructures”. In: *Molecular Beam Epitaxy and Heterostructures*. Ed. by Ploog K. Chang L.L. Dordrecht: Springer Netherlands, 1985, pp. 499–531.

[60] M. Field et al. “Measurements of Coulomb blockade with a noninvasive voltage probe”. In: *Phys. Rev. Lett.* 70 (9 Mar. 1993), pp. 1311–1314. DOI: 10.1103/PhysRevLett.70.1311. URL: https://link.aps.org/doi/10.1103/PhysRevLett.70.1311.

[61] A. B. Zorin. “The thermocoax cable as the microwave frequency filter for single electron circuits”. In: *Review of Scientific Instruments* 66.8 (Aug. 1995), pp. 4296–4300. ISSN: 0034-6748. DOI: 10.1063/1.1145385.

[62] W. G. van der Wiel et al. “Electron transport through double quantum dots”. In: *Rev. Mod. Phys.* 75 (1 Dec. 2002), pp. 1–22. DOI: 10.1103/RevModPhys.75.1.

[63] J. Weis et al. “Transport spectroscopy on a single quantum dot”. en. In: *Semiconductor Science and Technology* 9.11S (Nov. 1994), pp. 1890–1896. ISSN: 0268-1242. DOI: 10.1088/0268-1242/9/11S/006.

[64] Alex Bogan et al. **See supplementary material for** [**65**]. 2018.

[65] Alex Bogan et al. “Landau-Zener-Stuckelberg-Majorana Interferometry of a Single Hole”. In: *Physical Review Letters* 120.20 (May 2018), p. 207701. DOI: 10.1103/PhysRevLett.120.207701.

[66] J. M. Luttinger. “Quantum Theory of Cyclotron Resonance in Semiconductors: General Theory”. In: *Phys. Rev.* 102 (4 May 1956), pp. 1030–1041. DOI: 10.1103/PhysRev.102.1030. URL: https://link.aps.org/doi/10.1103/PhysRev.102.1030.

[67] Leon C. Camenzind et al. “Hyperfine-phonon spin relaxation in a single-electron GaAs quantum dot”. En. In: *Nature Communications* 9.1 (Aug. 2018), p. 3454. ISSN: 2041-1723. DOI: 10.1038/s41467-018-05879-x.

[68] M. Vidal et al. “Hyperfine coupling of hole and nuclear spins in symmetric (111)-grown GaAs quantum dots”. In: *Phys. Rev. B* 94 (12 Sept. 2016), p. 121302. DOI: 10.1103/PhysRevB.94.121302. URL: https://link.aps.org/doi/10.1103/PhysRevB.94.121302.

[69] Alex Bogan et al. “Consequences of Spin-Orbit Coupling at the Single Hole Level: Spin-Flip Tunneling and the Anisotropic g Factor”. In: *Physical Review Letters* 118.16 (Apr. 2017), p. 167701. DOI: 10.1103/PhysRevLett.118.167701.

[70] S. Studenikin et al. “Spin-Orbit Blockade in Two-Hole Double Quantum Dot at Zero Magnetic Field”. in preparation.

[71] Guido Burkard. “Quantum information: Positively spin coherent”. en. In: *Nature Materials* 7.2 (Feb. 2008), pp. 100–101. ISSN: 1476-4660. DOI: 10.1038/nmat2107.

[72] Alexander Tartakovskii. “Quantum information: Holes avoid decoherence”. en. In: *Nature Photonics* 5.11 (Nov. 2011), pp. 647–649. ISSN: 1749-4893. DOI: 10.1038/nphoton.2011.262.

[73] W. A. Coish et al. “Measurement, control, and decay of quantum-dot spins”. en. In: *physica status solidi (b)* 243.14 (Nov. 2006), pp. 3658–3672. ISSN: 1521-3951. DOI: 10.1002/pssb.200642348.

[74] C. Testelin et al. “Hole–spin dephasing time associated with hyperfine interaction in quantum dots”. In: *Physical Review B* 79.19 (May 2009), p. 195440. DOI: 10.1103/PhysRevB.79.195440.

[75] Xiaoya Judy Wang, Stefano Chesi, and W. A. Coish. “Spin-Echo Dynamics of a Heavy Hole in a Quantum Dot”. In: *Physical Review Letters* 109.23 (Dec. 2012), p. 237601. DOI: 10.1103/PhysRevLett.109.237601.

[76] Jan Fischer et al. “Spin decoherence of a heavy hole coupled to nuclear spins in a quantum dot”. In: *Physical Review B* 78.15 (Oct. 2008), p. 155329. DOI: 10.1103/PhysRevB.78.155329.

[77] P. Fallahi, S. T. Yılmaz, and A. Imamoğlu. “Measurement of a Heavy-Hole Hyperfine Interaction in InGaAs Quantum Dots Using Resonance Fluorescence”. In: *Physical Review Letters* 105.25 (Dec. 2010), p. 257402. DOI: 10.1103/PhysRevLett.105.257402.

[78] E. A. Chekhovich et al. “Direct Measurement of the Hole-Nuclear Spin Interaction in Single InP/GaInP Quantum Dots Using Photoluminescence Spectroscopy”. In: *Physical Review Letters* 106.2 (Jan. 2011), p. 027402. DOI: 10.1103/PhysRevLett.106.027402.

[79] S. G. Carter et al. "Strong hyperfine-induced modulation of an optically driven hole spin in an InAs quantum dot". In: *Physical Review B* 89.7 (Feb. 2014), p. 075316. DOI: 10.1103/PhysRevB.89.075316.

[80] Alexander V. Khaetskii and Yuli V. Nazarov. "Spin-flip transitions between Zeeman sublevels in semiconductor quantum dots". In: *Physical Review B* 64.12 (Sept. 2001), p. 125316. DOI: 10.1103/PhysRevB.64.125316.

[81] Vitaly N. Golovach, Alexander Khaetskii, and Daniel Loss. "Phonon-Induced Decay of the Electron Spin in Quantum Dots". In: *Physical Review Letters* 93.1 (June 2004), p. 016601. DOI: 10.1103/PhysRevLett.93.016601.

[82] Toshimasa Fujisawa et al. "Allowed and forbidden transitions in artificial hydrogen and helium atoms". en. In: *Nature* 419.6904 (Sept. 2002), pp. 278–281. ISSN: 1476-4687. DOI: 10.1038/nature00976.

[83] Miro Kroutvar et al. "Optically programmable electron spin memory using semiconductor quantum dots". en. In: *Nature* 432.7013 (Nov. 2004), pp. 81–84. ISSN: 1476-4687. DOI: 10.1038/nature03008.

[84] J. M. Elzerman et al. "Single-shot read-out of an individual electron spin in a quantum dot". en. In: *Nature* 430.6998 (July 2004), pp. 431–435. ISSN: 1476-4687. DOI: 10.1038/nature02693.

[85] R. Hanson et al. "Single-Shot Readout of Electron Spin States in a Quantum Dot Using Spin-Dependent Tunnel Rates". In: *Physical Review Letters* 94.19 (May 2005), p. 196802. DOI: 10.1103/PhysRevLett.94.196802.

[86] T. Meunier et al. "Experimental Signature of Phonon-Mediated Spin Relaxation in a Two-Electron Quantum Dot". In: *Physical Review Letters* 98.12 (Mar. 2007), p. 126601. DOI: 10.1103/PhysRevLett.98.126601.

[87] I. Siddiqi et al. "Dispersive measurements of superconducting qubit coherence with a fast latching readout". In: *Physical Review B* 73.5 (Feb. 2006), p. 054510. DOI: 10.1103/PhysRevB.73.054510.

[88] S. A. Studenikin et al. "Enhanced charge detection of spin qubit readout via an intermediate state". In: *Applied Physics Letters* 101.23 (Dec. 2012), p. 233101. ISSN: 0003-6951. DOI: 10.1063/1.4749281.

[89] M. A. Fogarty et al. "Integrated silicon qubit platform with single-spin addressability, exchange control and single-shot singlet-triplet readout". En. In: *Nature Communications* 9.1 (Oct. 2018), p. 4370. ISSN: 2041-1723. DOI: 10.1038/s41467-018-06039-x.

[90] Patrick Harvey-Collard et al. "High-Fidelity Single-Shot Readout for a Spin Qubit via an Enhanced Latching Mechanism". In: *Physical Review X* 8.2 (May 2018), p. 021046. DOI: `10.1103/PhysRevX.8.021046`.

[91] C. B. Simmons et al. "Tunable Spin Loading and T_1 of a Silicon Spin Qubit Measured by Single-Shot Readout". In: *Physical Review Letters* 106.15 (Apr. 2011), p. 156804. DOI: `10.1103/PhysRevLett.106.156804`.

[92] S. Nadj-Perge et al. "Disentangling the effects of spin-orbit and hyperfine interactions on spin blockade". In: *Physical Review B* 81.20 (May 2010), p. 201305. DOI: `10.1103/PhysRevB.81.201305`.

[93] John M. Nichol et al. "Quenching of dynamic nuclear polarization by spin–orbit coupling in GaAs quantum dots". en. In: *Nature Communications* 6 (July 2015), p. 7682. ISSN: 2041-1723. DOI: `10.1038/ncomms8682`.

[94] T. Fujita et al. "Signatures of Hyperfine, Spin-Orbit, and Decoherence Effects in a Pauli Spin Blockade". In: *Physical Review Letters* 117.20 (Nov. 2016), p. 206802. DOI: `10.1103/PhysRevLett.117.206802`.

[95] V. F. Maisi et al. "Spin-Orbit Coupling at the Level of a Single Electron". In: *Physical Review Letters* 116.13 (Mar. 2016), p. 136803. DOI: `10.1103/PhysRevLett.116.136803`.

[96] Yongjie Hu et al. "Hole spin relaxation in Ge–Si core–shell nanowire qubits". en. In: *Nature Nanotechnology* 7.1 (Jan. 2012), pp. 47–50. ISSN: 1748-3395. DOI: `10.1038/nnano.2011.234`.

[97] M. Wang, Y. Yin, and M. W. Wu. "Electric manipulation of electron spin relaxation induced by confined phonons in nanowire-based double quantum dots". In: *Journal of Applied Physics* 109.10 (May 2011), p. 103713. ISSN: 0021-8979. DOI: `10.1063/1.3592340`.

[98] S. Amasha et al. "Electrical Control of Spin Relaxation in a Quantum Dot". In: *Physical Review Letters* 100.4 (Jan. 2008), p. 046803. DOI: `10.1103/PhysRevLett.100.046803`.

[99] T. Hayashi et al. "Coherent Manipulation of Electronic States in a Double Quantum Dot". In: *Physical Review Letters* 91.22 (Nov. 2003), p. 226804. DOI: `10.1103/PhysRevLett.91.226804`.

[100] Alexander Croy and Ulf Saalmann. "Coherent manipulation of charge qubits in double quantum dots". en. In: *New Journal of Physics* 13.4 (2011), p. 043015. ISSN: 1367-2630. DOI: `10.1088/1367-2630/13/4/043015`.

[101] J. Stehlik et al. “Landau-Zener-Stuckelberg interferometry of a single electron charge qubit”. In: *Physical Review B* 86.12 (Sept. 2012), p. 121303. DOI: 10.1103/PhysRevB.86.121303.

[102] Dohun Kim et al. “Microwave-driven coherent operation of a semiconductor quantum dot charge qubit”. en. In: *Nature Nanotechnology* 10.3 (Mar. 2015), pp. 243–247. ISSN: 1748-3395. DOI: 10.1038/nnano.2014.336.

[103] Gang Cao et al. “Tunable Hybrid Qubit in a GaAs Double Quantum Dot”. In: *Physical Review Letters* 116.8 (Feb. 2016), p. 086801. DOI: 10.1103/PhysRevLett.116.086801.

[104] Bao-Chuan Wang et al. “Tunable Hybrid Qubit in a Triple Quantum Dot”. In: *Physical Review Applied* 8.6 (Dec. 2017), p. 064035. DOI: 10.1103/PhysRevApplied.8.064035.

[105] F. H. L. Koppens et al. “Driven coherent oscillations of a single electron spin in a quantum dot”. eng. In: *Nature* 442.7104 (Aug. 2006), pp. 766–771. ISSN: 1476-4687. DOI: 10.1038/nature05065.

[106] F. H. L. Koppens, K. C. Nowack, and L. M. K. Vandersypen. “Spin Echo of a Single Electron Spin in a Quantum Dot”. In: *Physical Review Letters* 100.23 (June 2008), p. 236802. DOI: 10.1103/PhysRevLett.100.236802.

[107] M. Veldhorst et al. “An addressable quantum dot qubit with fault-tolerant control-fidelity”. en. In: *Nature Nanotechnology* 9.12 (Dec. 2014), pp. 981–985. ISSN: 1748-3395. DOI: 10.1038/nnano.2014.216.

[108] E. A. Laird et al. “A new mechanism of electric dipole spin resonance: hyperfine coupling in quantum dots”. en. In: *Semiconductor Science and Technology* 24.6 (2009), p. 064004. ISSN: 0268-1242. DOI: 10.1088/0268-1242/24/6/064004.

[109] Stefano Chesi et al. “Single-spin manipulation in a double quantum dot in the field of a micromagnet”. In: *Physical Review B* 90.23 (Dec. 2014), p. 235311. DOI: 10.1103/PhysRevB.90.235311.

[110] Jun Yoneda et al. “Robust micromagnet design for fast electrical manipulations of single spins in quantum dots”. en. In: *Applied Physics Express* 8.8 (July 2015), p. 084401. ISSN: 1882-0786. DOI: 10.7567/APEX.8.084401.

[111] F. Forster et al. “Electric-dipole-induced spin resonance in a lateral double quantum dot incorporating two single-domain nanomagnets”. In: *Physical Review B* 91.19 (May 2015), p. 195417. DOI: 10.1103/PhysRevB.91.195417.

[112] L. R. Schreiber et al. “Coupling artificial molecular spin states by photon-assisted tunnelling”. en. In: *Nature Communications* 2 (Nov. 2011), p. 556. ISSN: 2041-1723. DOI: 10.1038/ncomms1561.

[113] K. C. Nowack et al. “Coherent Control of a Single Electron Spin with Electric Fields”. en. In: *Science* 318.5855 (Nov. 2007), pp. 1430–1433. ISSN: 0036-8075, 1095-9203. DOI: 10.1126/science.1148092.

[114] A. Pfund et al. “Spin-state mixing in InAs double quantum dots”. In: *Physical Review B* 76.16 (Oct. 2007), p. 161308. DOI: 10.1103/PhysRevB.76.161308.

[115] S. Nadj-Perge et al. “Spin–orbit qubit in a semiconductor nanowire”. en. In: *Nature* 468.7327 (Dec. 2010), pp. 1084–1087. ISSN: 1476-4687. DOI: 10.1038/nature09682.

[116] S. N. Shevchenko, S. Ashhab, and Franco Nori. “Landau–Zener–Stückelberg interferometry”. In: *Physics Reports* 492.1 (July 2010), pp. 1–30. ISSN: 0370-1573. DOI: 10.1016/j.physrep.2010.03.002.

[117] T. H. Oosterkamp et al. “Microwave spectroscopy of a quantum-dot molecule”. en. In: *Nature* 395.6705 (Oct. 1998), pp. 873–876. ISSN: 1476-4687. DOI: 10.1038/27617.

[118] J. R. Petta et al. “Manipulation of a Single Charge in a Double Quantum Dot”. In: *Physical Review Letters* 93.18 (Oct. 2004), p. 186802. DOI: 10.1103/PhysRevLett.93.186802.

[119] F. R. Braakman et al. “Dynamics of spin-flip photon-assisted tunneling”. In: *Physical Review B* 89.7 (Feb. 2014), p. 075417. DOI: 10.1103/PhysRevB.89.075417.

[120] F. Forster et al. “Characterization of Qubit Dephasing by Landau-Zener-Stuckelberg-Majorana Interferometry”. In: *Physical Review Letters* 112.11 (Mar. 2014), p. 116803. DOI: 10.1103/PhysRevLett.112.116803.

[121] M. Fernando Gonzalez-Zalba et al. “Gate-Sensing Coherent Charge Oscillations in a Silicon Field-Effect Transistor”. In: *Nano Letters* 16.3 (Mar. 2016), pp. 1614–1619. ISSN: 1530-6984. DOI: 10.1021/acs.nanolett.5b04356.

[122] P. K. Tien and J. P. Gordon. “Multiphoton Process Observed in the Interaction of Microwave Fields with the Tunneling between Superconductor Films”. In: *Phys. Rev.* 129 (2 Jan. 1963), pp. 647–651. DOI: 10.1103/PhysRev.129.647. URL: https://link.aps.org/doi/10.1103/PhysRev.129.647.

[123] P. Szumniak et al. “Spin-Orbit-Mediated Manipulation of Heavy-Hole Spin Qubits in Gated Semiconductor Nanodevices”. In: *Physical Review Letters* 109.10 (Sept. 2012), p. 107201. DOI: 10.1103/PhysRevLett.109.107201.

[124] P. Szumniak et al. “All-electrical control of quantum gates for single heavy-hole spin qubits”. In: *Physical Review B* 87.19 (May 2013), p. 195307. DOI: `10.1103/PhysRevB.87.195307`.

[125] Jan Fischer and Daniel Loss. “Hybridization and Spin Decoherence in Heavy-Hole Quantum Dots”. In: *Phys. Rev. Lett.* 105 (26 Dec. 2010), p. 266603. DOI: `10.1103/PhysRevLett.105.266603`.

Appendix A

Single Hole Transport Model

The single hole transport phenomena in chapters 4 and 6 were modeled numerically using a four-point Runge Kutta approach to integrate the following master equation:

$$\frac{\partial}{\partial t}\rho(t) = -\frac{i}{\hbar}\left[H, \rho(t)\right] + (\hat{\Gamma}_{in} + \hat{\Gamma}_{out} + \hat{\Gamma}_{T2F} + \hat{\Gamma}_{T2N} + \hat{\Gamma}_{T1N} + \hat{\Gamma}_{T1F} + \hat{\Gamma}_{T1S})\rho(t) \tag{A.1}$$

where the operators $\hat{\Gamma}_{in}$ and $\hat{\Gamma}_{out}$ represent tunneling of a single hole into the dot from the source or out of the dot to the drain. $\hat{\Gamma}_{T2N}$ and $\hat{\Gamma}_{T2F}$ model phase decoherence of the spin conserving and non-conserving tunneling, and $\hat{\Gamma}_{T1N}$ and $\hat{\Gamma}_{T1F}$ represent inelastic inter-dot charge tunneling via spin non-flipping and flipping pathways respectively. Finally, $\hat{\Gamma}_{T1S}$ is the relaxation of the spin excited state inside each quantum dot. These relaxation pathways are depicted in figure A.2.

Single hole transport was modeled in the basis: $(0,\Downarrow)$, $(0,\Uparrow)$, $(\Downarrow, 0)$, $(\Uparrow, 0)$, where for example $(\Downarrow,0)$ represents a single hole in the left dot in the lower spin state. This basis spans the lowest four states of the double quantum dot near the (1,0)/(0,1) charge transfer line. Note that $\rho(t)$ is not a true density matrix, as the state (0,0) is omitted and the trace of $\rho(t)$ is not preserved in general. The probability of occupation of the (0,0) state is $P_{00}(t) = 1 - \operatorname{tr}\rho(t)$.

The Hamiltonian of the system expressed in this basis is:

$$H = \begin{bmatrix} \frac{\Delta\epsilon}{2} + \frac{E_Z}{2} & 0 & -t_N & -it_F \\ 0 & \frac{\Delta\epsilon}{2} - \frac{E_Z}{2} & -it_F & -t_N \\ -t_N & it_F & -\frac{\Delta\epsilon}{2} + \frac{E_Z}{2} & 0 \\ it_F & -t_N & 0 & -\frac{\Delta\epsilon}{2} - \frac{E_Z}{2} \end{bmatrix} \tag{A.2}$$

where t_N and t_F are the spin non-flipping and spin flipping tunneling matrix elements respectively and $E_Z = g^*\mu_B B$ is the Zeeman energy.

The Γ operators representing the incoherent transitions are as follows:

$$\hat{\Gamma}_{in} = \begin{bmatrix} -\Gamma_o\rho_{11} & 0 & -\frac{1}{2}\Gamma_o\rho_{13} & -\frac{1}{2}\Gamma_o\rho_{14} \\ 0 & -\Gamma_o\rho_{22} & -\frac{1}{2}\Gamma_o\rho_{23} & -\frac{1}{2}\Gamma_o\rho_{24} \\ -\frac{1}{2}\Gamma_o\rho_{31} & -\frac{1}{2}\Gamma_o\rho_{32} & 0 & 0 \\ -\frac{1}{2}\Gamma_o\rho_{41} & -\frac{1}{2}\Gamma_o\rho_{42} & 0 & 0 \end{bmatrix} \tag{A.3}$$

$$\hat{\Gamma}_{out} = \begin{bmatrix} 0 & 0 & 0 & 0 \\ 0 & 0 & 0 & 0 \\ 0 & 0 & \Gamma_i(1 - \operatorname{tr}\rho) & 0 \\ 0 & 0 & 0 & \Gamma_i(1 - \operatorname{tr}\rho) \end{bmatrix} \tag{A.4}$$

with scalar fitting parameters Γ_o and Γ_i representing tunneling rates to the drain and from the source respectively.

$$\hat{\Gamma}_{T2F} + \hat{\Gamma}_{T2N} = \begin{bmatrix} 0 & 0 & -\frac{1}{T_{2N}}\rho_{13} & -\frac{1}{T_{2F}}\rho_{14} \\ 0 & 0 & -\frac{1}{T_{2F}}\rho_{23} & -\frac{1}{T_{2N}}\rho_{24} \\ -\frac{1}{T_{2N}}\rho_{31} & -\frac{1}{T_{2F}}\rho_{32} & 0 & 0 \\ -\frac{1}{T_{2F}}\rho_{41} & -\frac{1}{T_{2N}}\rho_{42} & 0 & 0 \end{bmatrix} \tag{A.5}$$

with scalar fitting parameters T_{2F} and T_{2N} representing mean dephasing lifetimes for the spin flipping and non-flipping transitions.

$$\hat{\Gamma}_{T1S} = \begin{bmatrix} -\frac{1}{T_{1S}}\rho_{11} & -\frac{1}{2T_{1S}}\rho_{12} & 0 & 0 \\ -\frac{1}{2T_{1S}}\rho_{21} & +\frac{1}{T_{1S}}\rho_{22} & 0 & 0 \\ 0 & 0 & -\frac{1}{T_{1S}}\rho_{33} & -\frac{1}{2T_{1S}}\rho_{34} \\ 0 & 0 & -\frac{1}{2T_{1S}}\rho_{43} & +\frac{1}{T_{1S}}\rho_{44} \end{bmatrix} \tag{A.6}$$

with scalar fitting parameter T_{1s} representing the mean spin relaxation lifetime within either quantum dot.

Finally, the inter-dot inelastic tunneling is more complex depending on which pathways are energetically allowed. For $|\Delta\epsilon| > |E_Z|$ (the alignment depicted in figure A.1 A-C) all transitions occur in the same direction and:

$$\hat{\Gamma}_{T1N}+\hat{\Gamma}_{T1F} = \begin{bmatrix} \frac{1}{T_{1F}}\rho_{33}+\frac{1}{T_{1N}}\rho_{44} & 0 & -(\frac{1}{2T_{1F}}+\frac{1}{2T_{1N}})\rho_{13} & -(\frac{1}{2T_{1F}}+\frac{1}{2T_{1N}})\rho_{14} \\ 0 & \frac{1}{T_{1F}}\rho_{33}+\frac{1}{T_{1N}}\rho_{44} & -(\frac{1}{2T_{1F}}+\frac{1}{2T_{1N}})\rho_{23} & -(\frac{1}{2T_{1F}}+\frac{1}{2T_{1N}})\rho_{24} \\ -(\frac{1}{2T_{1F}}+\frac{1}{2T_{1N}})\rho_{31} & -(\frac{1}{2T_{1F}}+\frac{1}{2T_{1N}})\rho_{32} & -(\frac{1}{T_{1F}}+\frac{1}{T_{1N}})\rho_{33} & -(\frac{1}{T_{1F}}+\frac{1}{T_{1N}})\rho_{34} \\ -(\frac{1}{2T_{1F}}+\frac{1}{2T_{1N}})\rho_{41} & -(\frac{1}{2T_{1F}}+\frac{1}{2T_{1N}})\rho_{42} & -(\frac{1}{T_{1F}}+\frac{1}{T_{1N}})\rho_{43} & -(\frac{1}{T_{1F}}+\frac{1}{T_{1N}})\rho_{44} \end{bmatrix} \tag{A.7}$$

for $|\Delta\epsilon| < |E_Z|$ the transition between the higher spin state of the lower charge distribution and the lower spin state of the higher charge distribution runs counter to the other transitions, and instead:

$$\hat{\Gamma}_{T1N}+\hat{\Gamma}_{T1F} = \begin{bmatrix} \frac{1}{T_{1F}}\rho_{33}-\frac{1}{T_{1N}}\rho_{11} & -\frac{1}{T_{1F}}\rho_{12} & -(\frac{1}{T_{1F}}+\frac{1}{2T_{1N}})\rho_{13} & -(\frac{1}{2T_{1F}}+\frac{1}{2T_{1N}})\rho_{14} \\ -\frac{1}{T_{1F}}\rho_{21} & \frac{1}{T_{1F}}\rho_{33}+\frac{1}{T_{1N}}\rho_{44} & -(\frac{1}{2T_{1F}}+\frac{1}{2T_{1N}})\rho_{23} & -\frac{1}{2T_{1N}}\rho_{24} \\ -(\frac{1}{T_{1F}}+\frac{1}{2T_{1N}})\rho_{31} & -(\frac{1}{2T_{1F}}+\frac{1}{2T_{1N}})\rho_{32} & -(\frac{1}{T_{1F}}+\frac{1}{T_{1N}})\rho_{33} & -(\frac{1}{2T_{1F}}+\frac{1}{T_{1N}})\rho_{34} \\ -(\frac{1}{2T_{1F}}+\frac{1}{2T_{1N}})\rho_{41} & -\frac{1}{2T_{1N}}\rho_{42} & -(\frac{1}{2T_{1F}}+\frac{1}{T_{1N}})\rho_{43} & \frac{1}{T_{1F}}\rho_{11}-\frac{1}{T_{1N}}\rho_{44} \end{bmatrix} \tag{A.8}$$

The measured current through the dot is then given by the trace of the matrix $\hat{\Gamma_o}\rho_0$, where ρ_0 is the steady solution to the master equation:

$$< I_{SD} >= - < q \,\mathrm{tr}\, \hat{\Gamma_o}\rho_0 > \tag{A.9}$$

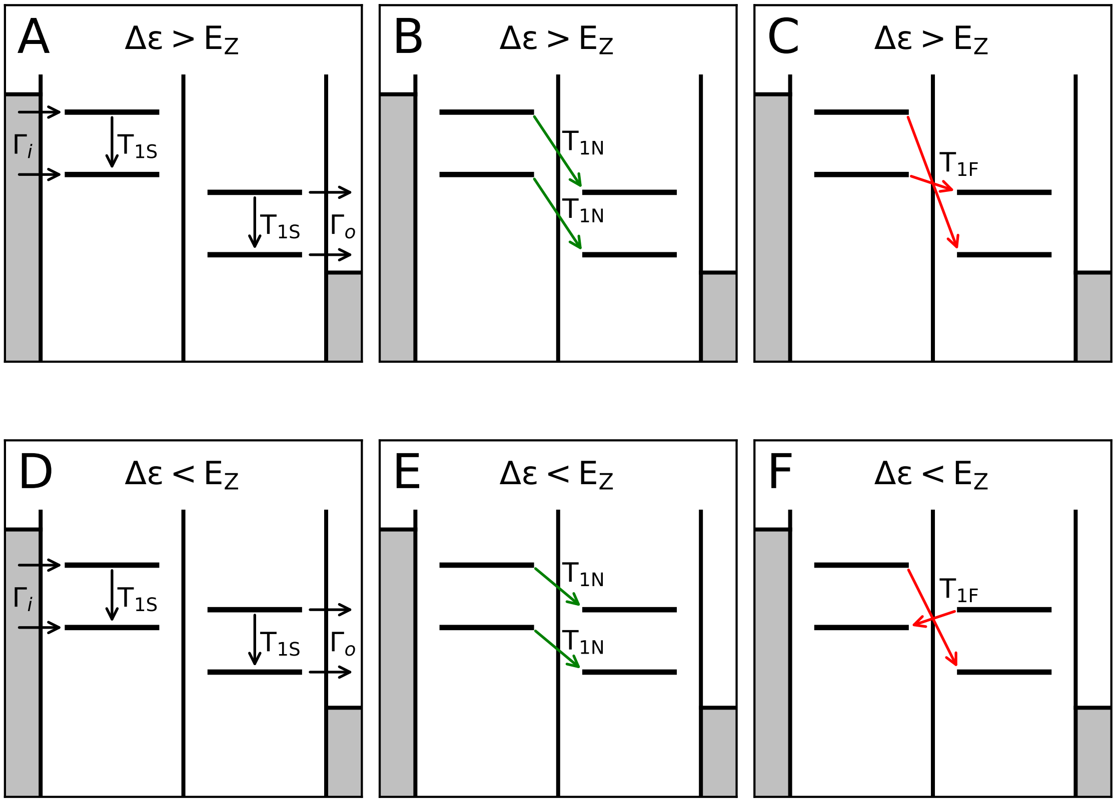

Figure A.1: Energy level diagrams showing different (simultaneously active) relaxation and tunneling pathways included in the model, with the arrows indicating the source and destination states for each operator for positive detuning. In ***A-C*** $\Delta\epsilon > E_Z$ *and in* ***D-F*** $\Delta\epsilon > E_Z$*. Note that one arrow is inverted between panels* ***C*** *and* ***F****.*

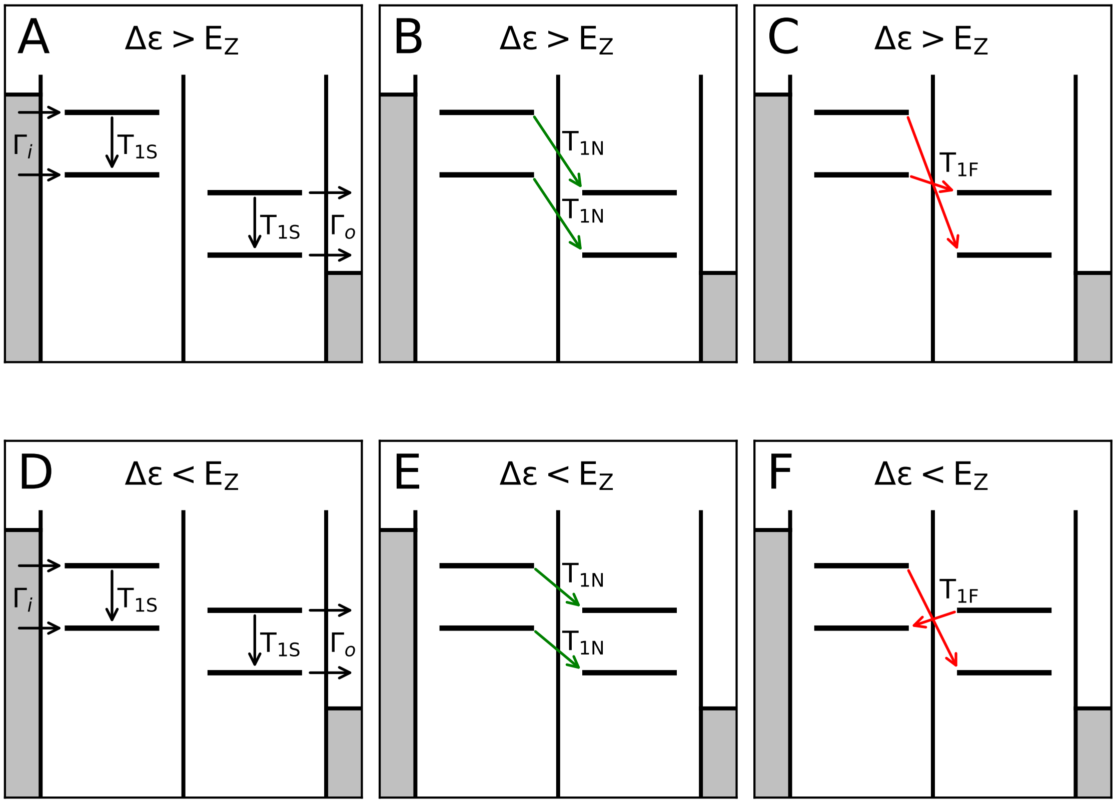

Figure A.2: Sketch of the incoherent processes and relaxation pathways included in the double quantum dot model, all of which act simultaneously. ***A*** *Tunneling to the left dot from the left lead at a rate Γ_l when the double quantum dot is empty, as well as tunneling from the right dot to the right lead at a rate Γ_r when the right dot is full. Spin relaxation within each dot is parameterized by a mean lifetime T_{1S}.* ***B*** *Inter-dot relaxation preserving spin is parameterized by the mean lifetime T_{1N}.* ***C*** *Inter-dot relaxation with a spin flip is parameterized by a single mean lifetime T_{1F}.*

Appendix B

Fidelity and Visibility of Single Hole Spin Projection and Readout

An assessment of the fidelity of the spin to charge conversion scheme used in chapter 5 requires knowledge of the input spin state. Where $P_{\Uparrow}$ and $P_{\Downarrow}$ are the respective probabilities of injecting up and down holes, the injected hole initially occupies the incoherent superposition:

$$|\Psi\rangle = P_{\Uparrow} |\Uparrow\rangle\langle\Uparrow| + P_{\Downarrow} |\Downarrow\rangle\langle\Downarrow| \tag{B.1}$$

However, it has been shown that $P_{\Uparrow}$ is a function of relaxation time, following equation 5.1. If the initial $P_{\Uparrow}(t = 0)$ can be estimated, then process tomography can be used to estimate the probability of a correct outcome of spin to charge conversion for a particular input spin.

To find the parameter $P_{\Uparrow}(t = 0)$, an experiment was conducted using off-resonant charge tunneling instead of the resonant scheme demonstrated in chapter 5. A random spin was injected using a minimal injection time $T_R = 100\,\mathrm{ns}$ into the left dot of the DQD, as in the main experiment, at $B = 1$ T. However, spin to charge conversion was executed at $\epsilon = -\frac{E_Z}{2}$ instead of $\epsilon = -E_Z$. This produced the arrangement of levels depicted in panel B of figure B.1.

Only three levels are relevant in this configuration: the initially populated states $|L \Uparrow\rangle$ and $|L \Downarrow\rangle$, as well as $|R \Downarrow\rangle$ in the right dot. Because no populated state ever crosses the state $|R \Uparrow\rangle$, it is assumed not to be populated.

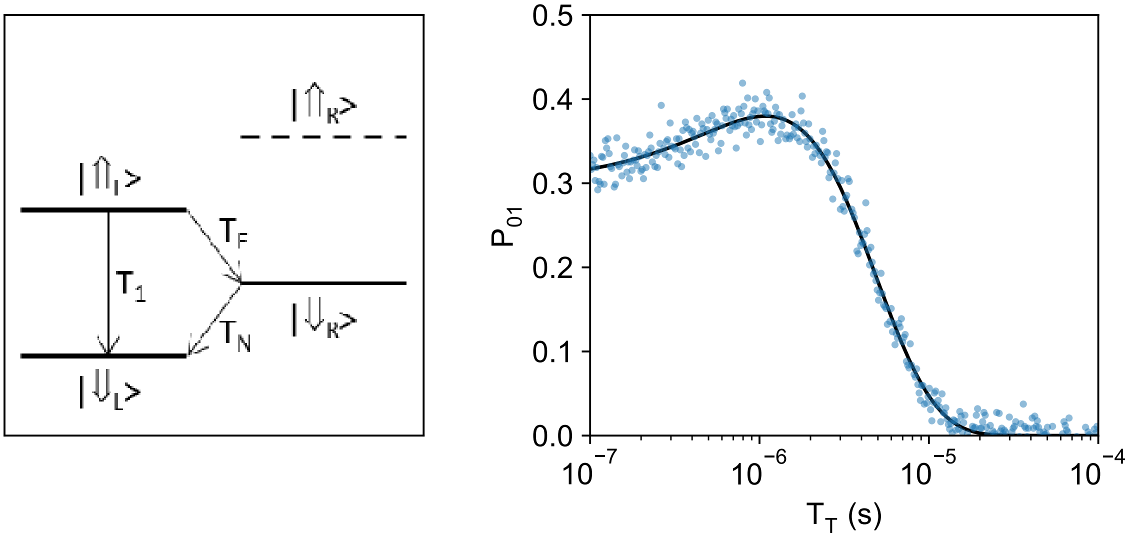

Figure B.1: ***A****) Sketch of the three-level decay model used to model the inelastic tunneling during inelastic spin to charge conversion.* ***B****) The probability of outcome (0,1) from 1000 inelastic spin to charge conversion attempts as a function of the inelastic transfer time,* T_T*. A fit to the lambda decay model to the right gives* $T_N = 3.58$ µs, $T_F = 1.86$ µs, *and* $P_{\Uparrow} = 0.766$*.* $T_1 = 3.3$ µs *was used as obtained in from chapter 5 for* $B = 1$ T.

The transfer time T_T, the duration of step 4 in figure 5.3, was varied. For each value of T_T, 1000 measurements were performed and a probability of outcome (0,1) was extracted: P_{01}. Panel A of figure B.1 shows the result. With increasing T_T, an initial increase in P_{01} is visible due to the finite inelastic charge tunneling time between $|L \Uparrow\rangle$ and $|R \Downarrow\rangle$. Moreover, an initial population of state $|R \Downarrow\rangle$ is observed. An opportunity for Zener tunneling occurs as $|L \Leftarrow\rangle$ crosses $|R \Downarrow\rangle$ between the injection and transfer steps. Indeed, for $T_R = 0$, this opportunity and this initial population both vanish.

P_{01} begins to decrease after 1 µs, due to inelastic tunneling from $|R \Downarrow\rangle$ into the left dot state $|L \Downarrow\rangle$, which is the ground state. P_{01} was fitted to a simple model with three decay rates: T_1 (single spin relaxation), T_F (spin flipping tunneling) and T_N (non spin-flipping tunneling). The fit yielded $T_F = 1.86$ µs, $T_N = 3.58$ µs, and $P_{\Uparrow} = 0.766$.

Given this information it is possible to calculate $P_{\Uparrow}$ and $P_{\Uparrow}$ for any given relaxation time T_R using equation 5.1.

Let the probability of receiving charge outcome x from the spin to charge conversion process given spin input y be $P(x|y)$. For example, $P(0,1|\Uparrow)$ denotes the probability of receiving charge outcome (0,1) with input spin $\Uparrow$.

Given the measured probability of each outcome shown in figure 5.4 panel A, and considering the (now) known input spins to the spin to charge conversion step for $T_R = 100$ ns and $T_R = 100$ µs, the conditional probabilities can be calculated from the measured charge state outcomes ($P_{01}(T_R)$) and predicted spin probability distribution ($P_{\Uparrow}(T_R)$):

Solving:

$$P_{01} = P(0,1|\Uparrow)P_{\Uparrow}(T_R) + P(0,1|\Downarrow)P_{\Downarrow}(T_R) \tag{B.2}$$
$$P_{00} = P(0,0|\Uparrow)P_{\Uparrow}(T_R) + P(0,0|\Downarrow)P_{\Downarrow}(T_R) \tag{B.3}$$
$$\tag{B.4}$$

for both $T_R = 100$ ns and $T_R = 100$ µs gives:

$$P(0,1|\Uparrow) = 0.52 \tag{B.5}$$
$$P(0,1|\Downarrow) = 0.01 \tag{B.6}$$
$$P(0,0|\Uparrow) = 0.48 \tag{B.7}$$
$$P(0,0|\Downarrow) = 0.99 \tag{B.8}$$

The fidelity of the measurement for an input spin $\Uparrow$ is the probability of (correctly) obtaining outcome (0,1). Similarly, the fidelity for a $\Downarrow$ input is the probability of correctly obtaining outcome (0,0).

Therefore:

$$F_{\Uparrow} = P(0,1|\Uparrow) \qquad = 0.52 \tag{B.9}$$

$$F_{\Downarrow} = P(0,1|\Downarrow) \qquad = 0.99 \tag{B.10}$$

The fidelities for each spin species were: $F_{\Uparrow} = P(1|\Uparrow) = 0.52$ and $F_{\Downarrow} = P(0|\Downarrow) = 0.99$, yielding a maximum visibility of $V = F_{\Uparrow} + F_{\Downarrow} - 1 = 0.51$ at B=1 T.

The dominant source of infidelity, and thus the limiting factor in the visibility, is likely the pulse shape. By simply resting on the resonance at $\epsilon = -E_Z$ for 100 ns, the left and right dot states hybridize and the probability of occupuying each of them equalize with time; hence, the probability of a net transfer from left to right is approximately 50%. An adiabatic charge transfer from left to right would raise the visibility closer to ideal.